

**ALTERNATIVE METHODS TO FINDING
PATTERNS IN HIRES STEREO DATA**

by

Rasha Usama Abbasi

A dissertation submitted to the faculty of
The University of Utah
in partial fulfillment of the requirements for the degree of

Doctor of Philosophy

Department of Physics

The University of Utah

August 2007

Copyright © Rasha Usama Abbasi 2007

All Rights Reserved

THE UNIVERSITY OF UTAH GRADUATE SCHOOL

SUPERVISORY COMMITTEE APPROVAL

of a dissertation submitted by

Rasha Usama Abbasi

This dissertation has been read by each member of the following supervisory committee and by majority vote has been found to be satisfactory.

Chair: Charles C. H. Jui

Mikhail Raikh

Wayne Springer

Jordan Gerton

Alex Balk

THE UNIVERSITY OF UTAH GRADUATE SCHOOL

FINAL READING APPROVAL

To the Graduate Council of the University of Utah:

I have read the dissertation of Rasha Usama Abbasi in its final form and have found that (1) its format, citations, and bibliographic style are consistent and acceptable; (2) its illustrative materials including figures, tables, and charts are in place; and (3) the final manuscript is satisfactory to the Supervisory Committee and is ready for submission to The Graduate School.

Date

Charles C. H. Jui
Chair, Supervisory Committee

Approved for the Major Department

Pierre Sokolsky
Chair/Dean

Approved for the Graduate Council

David S. Chapman
Dean of The Graduate School

ABSTRACT

The arrival direction study of Ultra High Energy Cosmic Rays potentially gives us an insight into their origin. The High Resolution Fly's Eye (HiRes) is a stereo air fluorescence experiment that detects cosmic rays with energies greater than $\sim 10^{18}$ eV. Here we present alternative methods to finding patterns in HiRes stereo data. In addition, we present the correlation of the observed cosmic rays patterns in the HiRes stereo data with some astronomical sources, in particular with BL Lac sources, which are a subclass of active galaxies.

To my parents Usama and Nawal.

CONTENTS

ABSTRACT	iv
LIST OF FIGURES	ix
ACKNOWLEDGMENTS	xii
CHAPTERS	
1. INTRODUCTION	1
1.1 Introduction	1
1.2 The Spectrum	3
1.3 Acceleration Sources Above 10^{14} eV	5
1.4 Acceleration of Cosmic Rays	5
1.4.1 Bottom-Up	7
1.4.2 Direct Acceleration Mechanism	7
1.4.3 Statistical Acceleration	8
1.4.4 Top-Down	8
1.5 Current Status of Cosmic Ray Science	9
2. PROPAGATION OF UHECRS IN THE UNIVERSE	11
2.1 The Origin of UHECRs	11
2.2 Galactic Magnetic Field (GMF)	13
2.3 Interaction With the IGMF	16
2.4 Interaction With the CMB	19
2.4.1 Photons	19
2.4.2 Protons	21
2.5 Conclusion	22
3. EXTENSIVE AIR SHOWER	23
3.1 Cosmic Ray Detection	23
3.2 Shower Development	23
3.2.1 The Hadronic Component	23
3.2.2 The Electromagnetic Component	25
3.2.3 The Muonic Component	25
3.3 Shower Parameters	26
3.3.1 Longitudinal Shower Distribution	26
3.3.2 Lateral Distribution	29
3.4 Čerenkov Light	29

4.	THE HIRES DETECTOR	32
4.1	Introduction	32
4.2	HiRes-1 and HiRes-2	33
4.3	Calibration	35
4.4	Atmospheric	39
4.4.1	Cloud Monitor	39
4.4.2	Xenon Flashers	40
4.4.3	Steerable Lasers	40
5.	EVENT RECONSTRUCTION AND SELECTION	44
5.1	Reconstruction	44
5.1.1	Noise Event Filtering	44
5.1.2	Shower Trajectory Reconstruction	45
5.1.3	Shower Profile Reconstruction	46
5.1.4	Analyzed Data Set	49
6.	SEARCH FOR EXTENDED CORRELATIONS	52
6.1	Introduction to Hough Transformation	52
6.2	Applying The Hough Transform	55
6.3	Background Estimation	55
6.4	Search for Significant Excess	59
6.5	Global Significance of Data Excess	63
6.6	Conclusion	63
7.	CROSS CORRELATION WITH BL LACERTAE OBJECTS	65
7.1	BL Lacertae Objects	65
7.1.1	Cross Correlation Study With BL-Lacertae	66
7.1.2	The Arc Average Point Correlation With BL-Lacertae	70
7.1.3	Conclusion	73
7.2	Bin-to-bin Correlation	74
8.	THREE POINT CORRELATION	79
8.1	Girard's Theorem	79
8.2	Spherical Trigonometry	83
8.3	Search for Significant Excess	86
8.3.1	Cross Correlation Between the Centroid of the Triplets With Small Solid Angles and BL-Lacertae	90
8.3.2	Three Point Correlation With the BL-Lacertae	91
8.4	Conclusion	95
9.	FOUR POINT CORRELATION	97
9.1	Four Point Configurations	97
9.1.1	Configuration 1: Spherical Triangle With Interior Point	97
9.1.2	Configuration 2: Spherical Quadrilateral	99
9.2	Classification of Quadruples	101

9.3 Four Point Auto Correlation	101
9.4 Conclusion	106
10. CONCLUSION	107
REFERENCES	109

LIST OF FIGURES

1.1 Flux vs. energy for the CR particles	4
1.2 The estimated magnetic field strength vs. size	6
1.3 This spectrum of ultra high energy cosmic rays above 10^{17} eV	10
2.1 The averaged sky distribution of the RMs.	15
2.2 The A0 dynamo pattern.	15
2.3 The spiral model of the GMF in the galactic plane.	16
2.4 Three models of the GMF using different choices of parameters.	17
2.5 The predicted distribution of deflection angles.	18
2.6 A full sky map of predicted deflection angle.	20
2.7 Cumulative fraction of the sky	21
2.8 Energy of a proton as a function of the propagation distance	22
3.1 A simple diagram of the EAS components.	24
3.2 Nitrogen fluorescence spectrum.	27
3.3 The shower mean elongation rate.	28
3.4 The simulated light signal vs. atmospheric depth	31
4.1 A picture of a detector building at the HiRes-2 observatory.	34
4.2 This figure shows a PMT cluster.	34
4.3 HiRes-1 event display.	36
4.4 HiRes-2 event display.	37
4.5 The pedestal subtracted QDE count vs. the mean number of photo- electrons.	38
4.6 A vertical flashers map	41
4.7 Steerable laser shots from HiRes-2 as seen from HiRes-1	42
4.8 A nearly horizontal laser shot as seen by HiRes-1.	43
5.1 Schematic of the Rayleigh scattering.	46
5.2 The SD plane.	47
5.3 Stereo trajectory reconstruction.	48
5.4 The upper figure shows the shower profile.	50

5.5	The 271 event stereo data set.	51
6.1	Simulated polarization plot by Gustavo Medina-Tanco	53
6.2	Illustration of the Hough transform	54
6.3	An illustration of the latitudinal binning.	55
6.4	The pointing direction, right ascension vs. declination	56
6.5	HiRes 271 event stereo data.	57
6.6	The bin occupancy values.	58
6.7	Right ascension and declination histograms.	60
6.8	Significance values for each bin.	61
6.9	The arcs found in the stereo data set	62
6.10	For the 2×10^4 isotropic MC sets.	64
7.1	Histogram of the cosine of the angle.	67
7.2	Histogram of the cosine of the angle.	68
7.3	This figure shows the distribution of the occupancy level.	69
7.4	Histogram of the cosine of the angle	70
7.5	Histogram of the cosine of the angle	71
7.6	This figure shows the histogram in	72
7.7	Histogram of the cosine of the angle	73
7.8	The correlation factor between the bin.	75
7.9	The CF between the bins of the $\cos\theta$ histogram.	76
7.10	The CF between the bins of the $\cos\theta$ histogram.	77
7.11	This figure shows the distribution of the occupancy level.	78
8.1	A sphere divided into two hemispheres.	80
8.2	This figure shows the angles of the spherical triangle.	81
8.3	This figure shows the lune bounded by two half.	82
8.4	This figure shows a generic spherical triangle.	84
8.5	A histogram of the area of the spherical triangles.	88
8.6	A histogram of the area of the spherical triangles.	89
8.7	A diagram of three points.	91
8.8	A histogram of $\cos(\theta)$	92
8.9	The distribution of the number of spherical triangles	93
8.10	The histogram distribution of the $\cos(\theta)$	94

8.11 A histogram of the area of the spherical triangles. 95
9.1 The configurations of four points on a sphere. 98
9.2 The area of the second configuration. 99
9.3 Two different divisions of a spherical quadrilateral. 100
9.4 First condition. 102
9.5 Second condition 103
9.6 Third condition. 104
9.7 The histogram of the solid angle. 105

ACKNOWLEDGMENTS

I would like to thank my advisor Charlie for his great help. He taught me many things through the years about doing research and understanding many physical concepts. He has been a great teacher and mentor to me. He also supported me through many stages in my graduate school. I don't think I can thank him enough for everything that he did for me.

I would also like to thank Stan Thomas. He always made me feel comfortable to ask for his help any time I needed it. I would also like to thank John Matthews for being really helpful whenever I needed anything non-physics related.

I would really like to thank many people in the HiRes group for many discussions about the detector and the detector events reconstruction and data analysis.

I would like to thank my parents. They supported me living abroad for many years to finish my graduate school and fulfill my dreams. They always made feel that I am loved beyond any limits. I really feel so lucky to have them in my life. I would also like to thank my brother Bassam for believing in me and always making sure that I believe that I can do anything if I put my heart in it. I would also like to thank my brother Hussam for always making sure that nothing would stop him from doing anything for me.

I would also like to thank my friends here and back in Jordan for always supporting me and caring for me. They all have enriched my life on many levels.

I love you all.

CHAPTER 1

INTRODUCTION

1.1 Introduction

The history of cosmic rays research is filled with fascinating adventures. Scientists have ridden hot air balloons, climbed mountains and traveled great distances to remote places in attempting to unlock the mystery of cosmic rays.

At the beginning of the 20th century, physicists noticed background radiation. This radiation was detected everywhere even in the absence of radioactive matter. The radiation was believed to be due to the natural radiation of the Earth. To further investigate this radiation, the Austrian physicist Victor F. Hess made a series of balloon ascents, through his careful measurements, to heights many kilometers above sea level. Hess discovered that the radiation intensity increases with height. He concluded that the source of this radiation is from the outer space and he called it “cosmic radiation” [1].

In 1925 Millikan and Cameron argued that cosmic rays were a result of a complex formation of nuclei. These nuclei are the result of the binding between an electron and a proton (the only elementary particles known at the time). Such a process would release binding energy in the form of gamma rays (cosmic radiation). Thus they introduced the term “cosmic rays” (CRs) [2].

Millikan’s theory was proven wrong by Compton who measured the intensity of the CRs at 69 stations distributed over the Earth. Through his measurements he found that CRs are affected by the Earth’s magnetic field indicating that CRs are in fact charged particles and definitely not neutral rays [3].

Along the way, observing CRs gave birth to many important discoveries. In 1933 while Carl Anderson was watching the tracks left by cosmic rays passing through his cloud chamber, he discovered antimatter when he noticed the existence

of a subatomic particle identical to an electron but possessing a positive charge (positron) [4]. In 1936 Seth Neddermeyer and Carl Anderson discovered another subatomic particle 207 times heavier than an electron, the muon [5]. These breakthroughs were the beginning of many discoveries, which led to a whole new field of study: elementary particle physics.

In 1938 Pierre Auger placed detectors on the Alps. He observed coincidental events in two detectors separated by 20 meters. He concluded that these were secondary particles from a single source [6]. With his array, Auger observed CRs with energies up to 10^{15} eV. This discovery was at a time when the most energetic particles detected from radioactivity or accelerators had an energy of a few MeV. He concluded that the source of such energetic particles must be of great extension:

One of the consequences of the extension of the energy spectrum of cosmic rays up to 10^{15} eV is that is actually impossible to imagine a single process able to give to a particle such an energy. It seems much more likely that the charged particles which constitute the primary cosmic radiation acquire their energy along electric fields of a very great extension. [7].

In 1949 Enrico Fermi proposed the shock acceleration model, where protons accelerate by bouncing off a moving magnetic cloud. However, this model could not explain the higher energetic particles that were detected by succeeding experiments. A satisfactory model that would explain these energetic particles has yet to be found [8].

In 1962 John Linsley using his detector in the desert of New Mexico observed a CR with an energy of 10^{20} eV. Several other experiments also observed such energetic particles. In 1991, the Fly's Eye cosmic research group detected a CR with an energy of 3×10^{20} eV. In 1994 the Japanese group Akino Giant Air Shower Array (AGASA) detected another CR event with an energy of 2×10^{20} eV. Such observations puzzled the CR community for two reasons. First, in 1966 Greisen-Zatespin-Kuzmin (GZK) suggested that since CRs interact with Cosmic Microwave Background (CMB), high Energy Cosmic Rays ($E \geq 6 \times 10^{19}$ eV) will have enough energy that when colliding with 2.7 K photons of the CMB they will

produce a δ resonance. This will produce a pion and a proton of lower energy. The mean free path in the uniform CMB is ≈ 50 Mpc for a cosmic ray proton of $10^{20}eV$. Hence such interaction with the CMB would reduce their energy. Therefore CRs traveling a long intergalactic distance could not be detected with energies greater than $6 \times 10^{19}eV$ (the GZK cutoff) ([9], [10]). The second reason for this puzzlement is the fact that at lower energies the cosmic ray trajectories bend in the Galactic magnetic field. At these high energies they should be traveling a straight line and should point back to their origin for they suffer very little bending due to the magnetic field. None of the observed events points back to an astrophysical source(s) that could produce such energetic events.

Until today, after one century of observing CRs, we still do not know the answer to fundamental questions about their nature: What are they? Where are they from? What could cause these particles to travel through space with such high energies?

1.2 The Spectrum

Cosmic rays are energetic particles, mostly protons. The spectrum is shown in Figure 1.1 ([11], [12]). It shows the change in the observed flux with energy. Note how the spectrum follows a power law

$$\frac{dN}{dE} \propto E^{-\alpha} \quad (1.1)$$

where N is the number of observed particles, E is the particle energy and α is the spectral index. The spectral index is different for different energy ranges. Its value is ~ 2.7 up to $10^{15}eV$ energy range. Below $10^{15}eV$ the slope is 2.7, however, the spectrum steepens at the “the knee” to a slope of ~ 3.0 above this. Around $3 \times 10^{18}eV$, the spectrum flattens a bit. This region is called “the ankle.” The fact that the spectrum follows a power law is important. It restricts possible acceleration mechanisms and it also indicates that different sources are responsible for different spectral indices [13].

The leading candidate for the source of CRs with energies below $10^{14}eV$ are supernova explosions. Although the acceleration of CR particles inside an expanding Supernova Remnant (SNR) shocks, theoretically, is well understood, it has been

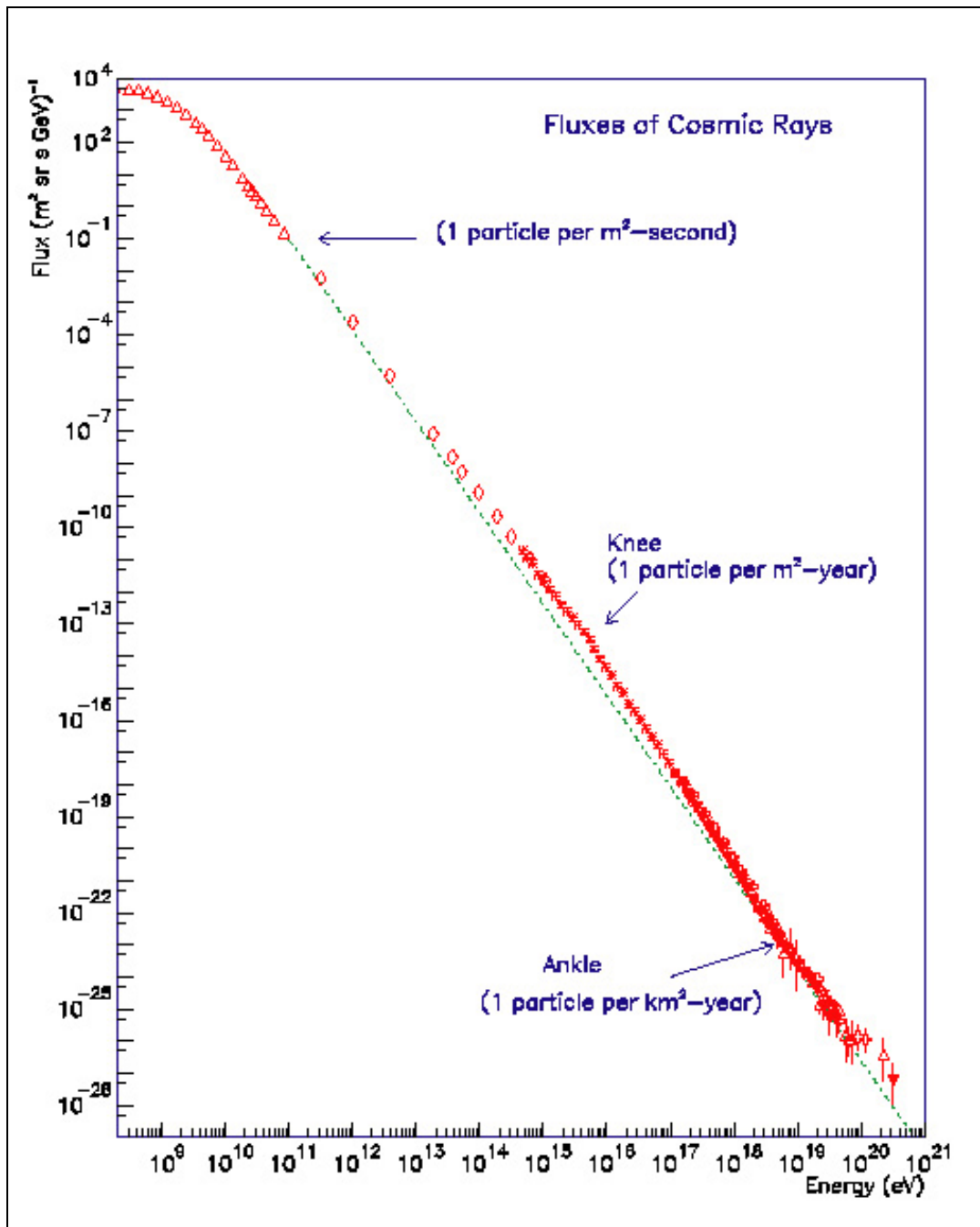


Figure 1.1. Flux vs. energy for the CR particles. The flux is in $(m^2 \text{ srs GeV})^{-1}$ and energy is in eV. This figure was originally made by S.Swordy [11] and modified by X. Bertou [12]). Note that the spectrum is virtually featureless. There is only a slight kink (knee) around 10^{16} eV.

very challenging to detect. The most recent evidence is a TeV γ -ray image of the SNR RX J1713.7-3946 which was presented by the High Energy Stereoscopic System (HESS). With this image, HESS was able to demonstrate that highly energetic particles accelerate in the SNR [14].

1.3 Acceleration Sources Above 10^{14} eV

The acceleration mechanisms for cosmic rays with energies greater than 10^{14} eV remain unknown. The problem, as interpreted by M. Hillas, is as follows: The path of a charged cosmic ray particle passing through a magnetic field will get deflected. The deflection is described by the Larmor radius, $R_L = 1.08 \frac{E}{10^{15} \text{eV}} \frac{\mu\text{G}}{B} \frac{1}{Z}$ pc, where E is the energy in PeV, Z is the particle charge and B is the magnetic field in micro-gauss. In a mode of gradual acceleration the particle passes through both regular and irregular fields. Hence, the size of the region, in which the particle accelerates, must be at least of the order of $\sim 2 \frac{E}{ZB\beta}$ where βc is the velocity of the scattering centers and c is the speed of light. Hence, the maximum energy of a particle accelerated from a source with size L and magnetic field B is:

$$E_{max} \sim ZBL\beta. \quad (1.2)$$

Figure 1.2 shows a plot of the estimated magnetic field length vs. the size of various different sources where cosmic rays could be accelerated. Essentially, the source needs to either have a very huge magnetic field or very extended space, and in either case the shock front speed needs to be very fast. The sites below the line of $\beta = 1/300$ do not meet the condition to accelerate protons to 10^{20} eV. Even for the extreme assumption where $\beta = 1$, very few objects remain as potential sources of such energetic particles. In addition, we have yet to account for energy loss processes that the particles would undergo. Such energy losses include synchrotron radiation and photo-production interaction. Taking this into account, the detection of cosmic rays with energies greater than 10^{20} eV is as great a mystery as ever [15].

1.4 Acceleration of Cosmic Rays

Two potential types models of cosmic ray acceleration are:

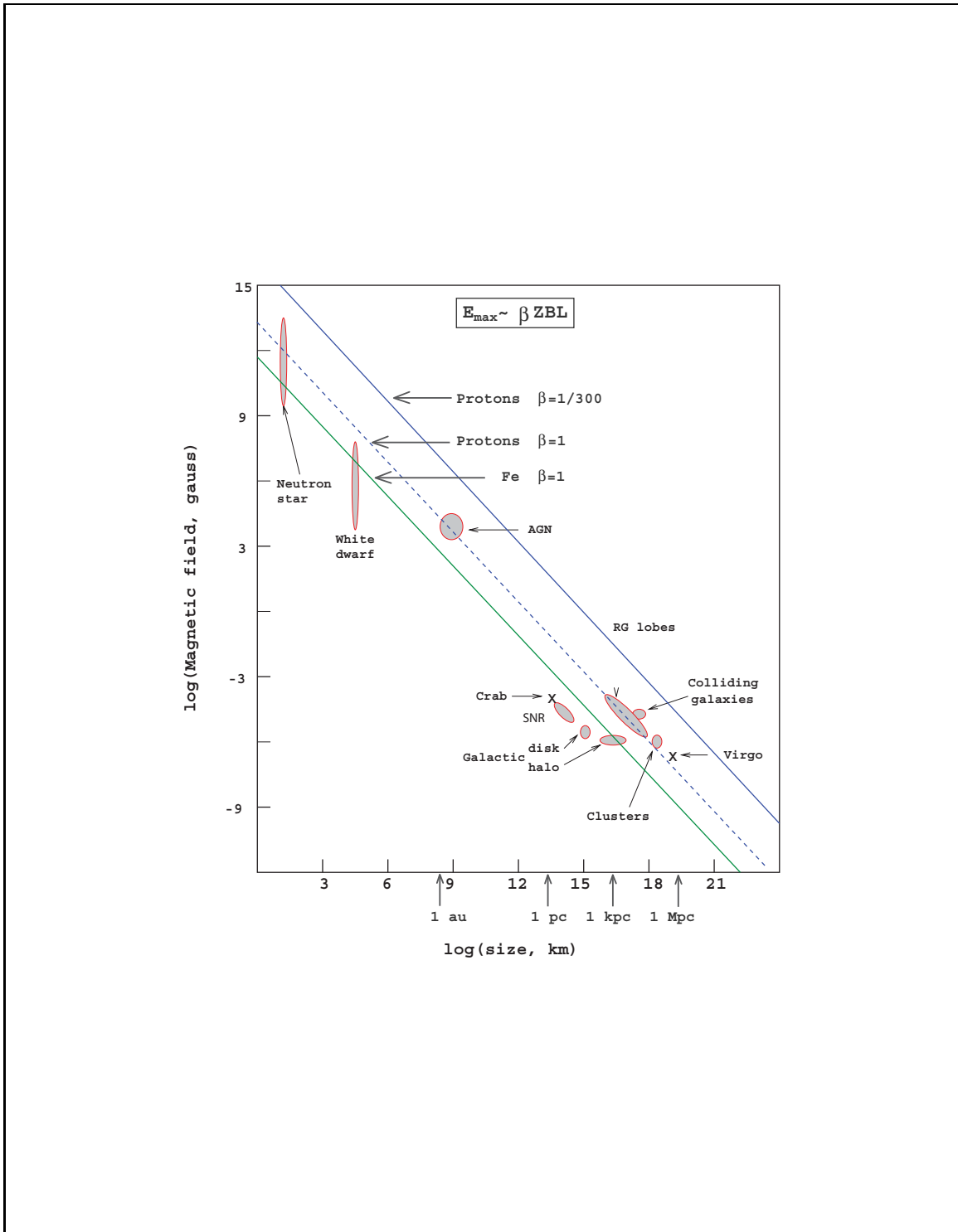


Figure 1.2. The estimated magnetic field strength vs. size for potential cosmic ray acceleration sites. Objects below the line of $\beta = 1/300$ cannot accelerate particles to 10^{20} eV. Even for the extreme assumption, where $\beta = 1$, very few sites remain as possible sources. This plot was made by M. Hillas [15] and modified by Bhattacharjee and Sigel [17].

1. Bottom-up, in these models cosmic rays are accelerated in shocks and other collisions and then travel through space to us.
2. Top-down, in these models ultra high energy cosmic rays are the result of a decay of exotic remnant particles from the early universe.

1.4.1 Bottom-Up

There are two suggested bottom-up models: In one the particles are accelerated directly and in the other they are accelerated statistically. In the direct acceleration mechanism, particles are accelerated by electric fields such as those found in a rotating neutron star or an accretion disk. Such mechanisms have the advantage of occurring so quickly that they can overcome energy loss processes. The disadvantage of this method is that it requires extremely complex analysis which does not clearly lead to a power-law spectrum.

In the statistical acceleration mechanism, particles are accelerated by repeatedly interacting with moving magnetic fields, gradually gaining energy. This naturally leads to an energy that is spread over many decades of energy and an energy spectrum that fits a power law of $\sim E^{-2}$. A major disadvantage of this method is that it is slow and competing energy losses are quite difficult to overcome [15], [16].

1.4.2 Direct Acceleration Mechanism

Neutron stars are strong candidates for sources of direct acceleration mechanism. They contain strong magnetic fields, of order 10^{12} Gauss, are several kilometers in diameter and rotate quickly, ~ 30 rounds per second. Such sites would produce an Electromotive Motive Force (EMF) of order $\sim 10^{18}$ eV. With this EMF, particles could accelerate to the ultra high energy regime. Such a possibility depends upon the rate at which the EMF drops with distance from the neutron star. If the EMF only drops off far from the neutron star, then the particle can travel longer distances without much loss in its energy. Examples of such sources are a neutron star with a corotating magnetosphere and a rotating accretion disk around a blackhole. In such cases the EMF is likely to fall far from the source. Conversely, if the EMF drops close to the neutron star the particle's energy loss would be great, and the

star would not be a candidate for source of ultra high energy particles. One needs to keep in mind that this model remains problematic on the ground that it is not clear how such sources would produce the spectrum power loss. [13]

1.4.3 Statistical Acceleration

In general terms, for any statistical acceleration model, if we assume t_a is the average acceleration time and t_b is the average escape time, then the power-law spectrum $dE/dx = E^{-\alpha}$ where $\alpha = 1 + t_a/t_b$. The fact that the detected spectrum has $\alpha = 2$ implies that t_a equals t_b . However, this is problematic since the greater the energy of the accelerated particle, the less the escape time from the source would be. One possibility could be that energy losses increase fast enough so as to cancel the energy gains. In such a case, t_a needs to be $< t_{loss}$, the energy loss time, for the spectrum index to meet the observed criteria.

Note that if we assume a low magnetic field, the main energy loss mechanism is the interaction of CR particles with CMB. This leads to an energy loss time, t_{loss} of $\sim 10^8 - 10^9$ years to obtain energies between 10 and 100 EeV. Following such condition the only acceptable model for this picture is the radio galactic hot spots. Note that, to date, no significant anisotropy has been observed in ultra high energy cosmic rays let alone any indication that radio galactic “hot spots” might be their sources [13].

1.4.4 Top-Down

In the top-down model, highly energetic particles are the result of the decay of super-massive “X particles” with a mass $m_X \gg 10^{20}$ eV. The decay or annihilation of these supermassive particles could produce secondary particles with energies up to m_X . It has been proposed that these exotic particles could be topological defects from the early universe (such as monopoles or cosmic strings, etc), such topological defects could be associated with the spontaneous symmetry-breaking phase transition investigated by the Grand Unification Theories (GUTs). Alternatively, the X particles could also be supermassive particles that were created in the early universe. In this scenario, such particles would be located in the galactic halo,

potentially explaining an absence of a GZK cutoff. This model would result with anisotropy in the cosmic-ray arrival directions to the galactic halo. Such anisotropy has not been observed [17].

1.5 Current Status of Cosmic Ray Science

The source of the UHECRs can be solved through the detection of the existence or the nonexistence of the GZK cutoff. The two experiments with the largest published data sets are the Akeno Giant Air Shower Array (AGASA) and the High Resolutions Fly's Eye (HiRes). Figure 1.3 shows the CR spectrum above 10^{17} eV as observed by the two experiments. As shown in Figure 1.3 there is an observed cosmic ray spectrum beyond 10^{20} eV. Nonetheless, The AGASA experiment spectrum shows no suppression beyond the GZK cutoff, while the HiRes experiment does observe a GZK cutoff at $\sim 5\sigma$ level. This is a key piece of information. It has been suggested that there are problems with AGASA's energy measurement and in particular with the μ distribution and with late arrival particles since their detectors use a "time-over-threshold" measurement. However, we still require measurements on anisotropy to determine sources whatever they are. A future experiment such as the Telescope Array TA is still under development in the Utah desert. TA is among experiments that will collect greater statistics and hopefully solve these issues.

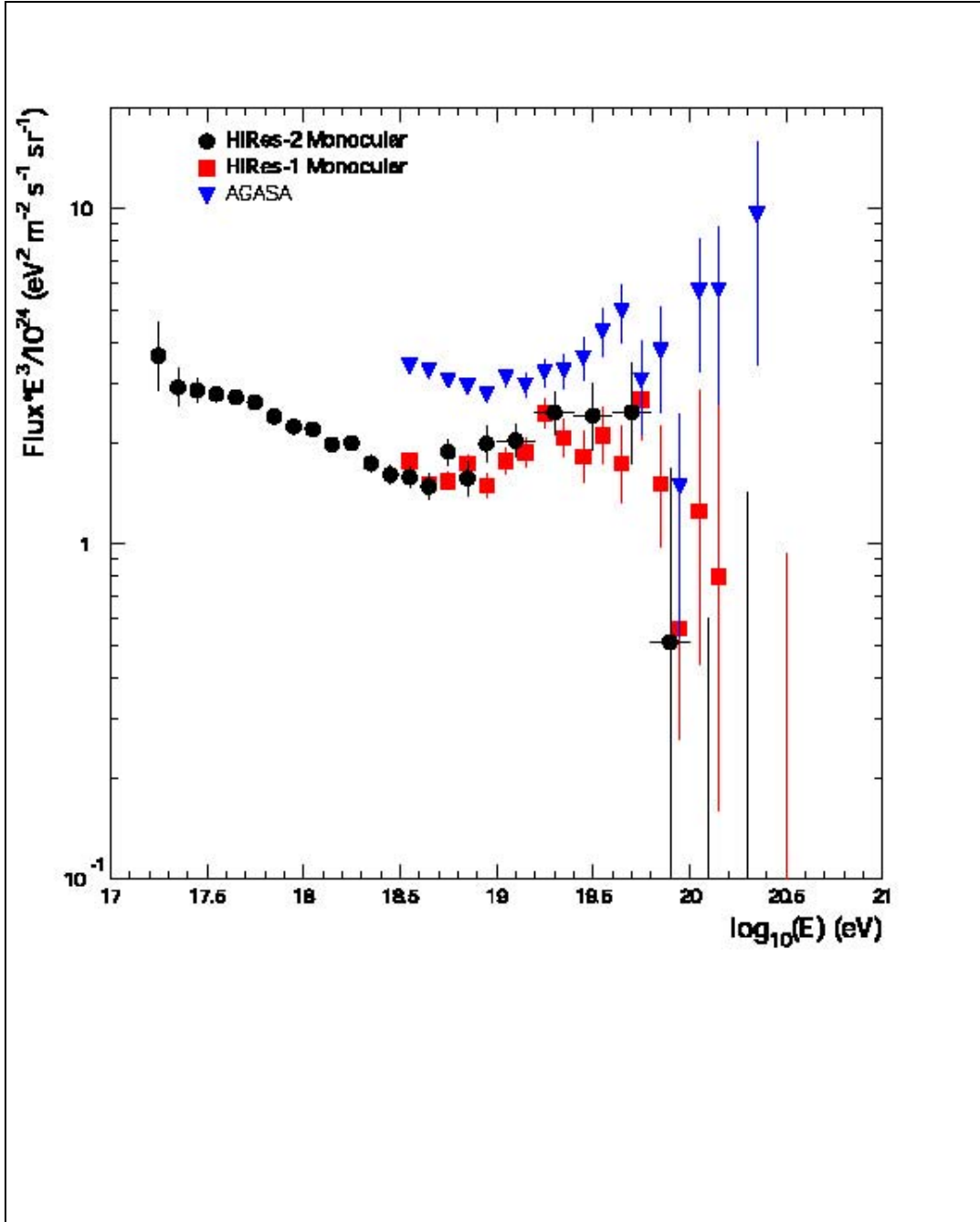


Figure 1.3. This spectrum of ultra high energy cosmic rays above 10^{17} eV as observed by HiRes-1,2 monocular [20] and AGASA [21]. There are two significant differences between the HiRes and AGASA spectra. First there is an obvious energy shift with AGASA being almost 30% higher in energy than HiRes. A newer “reanalysis” of AGASA data using Corsica is having the effect of lowering that spectrum by 10-15% with some energy dependence. A second difference is that the AGASA spectrum continues unabated beyond 6×10^{19} eV, the expected threshold of GZK suppression. The HiRes spectrum, on the other hand, shows strong suppression and is inconsistent with a continuing spectrum at nearly the 5σ level.

CHAPTER 2

PROPAGATION OF UHECRS IN THE UNIVERSE

2.1 The Origin of UHECRs

One of the biggest open questions in CR research is finding the origin of the Ultra High Energy Cosmic Rays (UHECRs). This problem is a great challenge due to the rapidly diminishing flux of particles as energy increases. In addition, when CR particles travel through the universe they do not pass unhindered. They must pass through the Magnetic Field (MF) and the Cosmic Microwave Background (CMB). Such interaction results in a deflection of the particles and limits the maximum distances over which we can accurately point back to the sources.

The key to doing CR astronomy is understanding the magnetic fields. The magnetic fields are classified as: the regular MF and random MF. The regular MF will deflect the charged CR particle with a motion characterized by Larmor radius, R_{Larmor} :

$$\frac{R_{Larmor}}{kpc} \approx \frac{1}{Z} \frac{E}{10^{18}eV} \frac{1\mu G}{B} \quad (2.1)$$

where E is the energy of the particles, Z is the charge of the particle and B is the strength of the magnetic field the particle is traversing. Accordingly, such a particle would get deflected by an angular deflection, δ :

$$\delta = \frac{S}{R_{Larmor}} \quad (2.2)$$

where δ is in degrees and S is the distance that the charged nuclei travels through

the field. Consequently, δ can also be expressed as

$$\delta = 0.5^0 Z \frac{S}{kpc} \frac{B}{\mu G} \frac{10^{20} eV}{E}. \quad (2.3)$$

Thus, we need to know the strength of the MF in the intervening space. This, of course, depends on the location of the CR source. If the source is galactic then the particle would get deflected by the Galactic MF (GMF) ($B \sim \mu G$). However, if the source is Extra Galactic (EG), the particle would first get deflected by the Extra Galactic Magnetic Field (EGMF) then by the Inter Galactic MF (IGMF) (the MF between galaxies) then by the GMF. In this case, we need to know the MF strength at each stage of the CR particle path.

Note that if the CR particle is a proton from a galactic source and has an energy below the ankle ($\sim 10^{16} eV$), it is expected to go through quite large deflections thus CR astronomy is impossible. Only protons with energies of greater than a few $10^{19} eV$ would experience deflections small enough to trace them back to their source within the galaxy. Also note that in the case of iron nuclei no anisotropy is expected toward the galactic plane, unless their energies exceed $\sim 10^{21} eV$. In other words, for particles with low charge and high enough energy, we might expect the deviation to be small enough that we could potentially correlate the tracks with sources.

A CR particle passing through a regular MF would result in the greatest deflection, yet if the particle passes through an irregular MF the mean deflection of a charged CR particle vanishes and the important quantity is the root mean square of the value of the deflection described by δ_{rms} where:

$$\delta_{rms} = \frac{1}{\sqrt{2}} \frac{Ze}{E} B_{rms} \sqrt{L} \sqrt{L_c} \quad (2.4)$$

or,

$$\delta_{rms} \simeq 1.5^0 \frac{1}{Z} \frac{40 \times 10^{18} E eV}{E} \frac{B_{rms}}{5 \mu G} \frac{\sqrt{L}}{2 kpc} \frac{\sqrt{L_c}}{50 pc} \quad (2.5)$$

where L is the distance traversed by the CR charge through the random MF,

Z is the charge of the CR particle and E is the energy of the CR particle. L_c is the coherence length, and the B_{rms} is the root mean square value of the turbulent magnetic field. Note that the deflection through a random MF is effectively a random walk deflection where $N = S/L$ and the net deviation is \sqrt{N} [22].

2.2 Galactic Magnetic Field (GMF)

Understanding the magnetic field that the charged CR traverses is a crucial element when collecting the puzzle pieces to understand the origin of the CR particles. One way of probing the GMF is through Faraday rotation. When light waves pass through a medium in a magnetic field, the waves undergo a rotation in their polarization which is proportional to the magnetic field strength. The relation between the angle of rotation of the polarization and the magnetic field is

$$\beta = \nu B d \quad (2.6)$$

where β is the angle rotation (in radians), B is the magnetic flux density in the direction propagation (in Tesla), d is the interaction path length (in meters), and ν is the Verdet constant for the material, which varies for wavelength and material. A positive Verdet constant corresponds to counter-clockwise rotation when the propagation is parallel to the magnetic field.

By measuring the rotation, we can estimate the magnetic field strength. Due to the Earth's position in the galaxy we are well positioned to measure the magnetic field both through the main body of the galaxy (edge-on) and of the galactic halo.

With Faraday rotation we are able to measure the magnetic component parallel to our line of sight. This can be achieved by measuring the Rotation Measures (RM) and the Dispersion Measures (DM) of the polarized light from hundreds of pulsars and many extragalactic radio sources. The RM is the integration of the product of the electron density and with the magnetic field along the line of sight from the source to the observer.

$$RM = a \int_{source}^{observer} n_e B_{\parallel} dl, \quad (2.7)$$

where a is a constant, n_e is the electron density, B_{\parallel} is the magnetic field and dl is the unit length along the line of sight. The DM on the other hand is the integration of the electron density along the line of sight.

$$DM = a \int_{source}^{observer} n_e dl \quad (2.8)$$

This would lead to a measurement of the magnetic field where $B_{\parallel} = 1.232RM/DM$. The average magnetic field in our galaxy was found to be equal to few $\sim \mu G$ [23].

Through the measurements of the averaged sky distribution of the RMs (as shown in Figure 2.1), we are able to probe the magnetic field in the Galactic halo. In this figure, filled symbols represent positive RMs, and open symbols represent negative RMs [24]. Note how the antisymmetric pattern is consistent with the A0 dynamo (see Figure 2.2). The dynamo has toroidal fields with reversed direction above and below the galactic plane, possibly all the way through the molecular zone [25], Note that there is no observational confirmation of high intensity of the magnetic field in the center of our galaxy[[26], [27]].

While the structure of the magnetic field in the galactic disk is not known on a small scale level, there are two models for the large scale structure of the MF. The Axi-symmetric (ASS) spiral model, and the Bi-symmetric (BSS) spiral models, are shown in Figure 2.3. To date, there are too few observations of extra-galactic radio sources to reach solid conclusions concerning these models [28].

Such limited knowledge of the MF limits our ability to make more than an order of magnitude estimation of the CR deflections. Figure 2.4 shows three models of the GMF made by three different groups (Tinyakov and Tkachev (TT), Harari, Mollerach and Roulet (HMR) and Prouza and Simda (PS) [29], [30], [31]) using different choices of parameters. The figure shows the deflection (as seen from the Earth) of protons with energy of $4 \times 10^{19}eV$ propagated backwards 50 kpc away from the galactic center. The deflection maps are shown in the Hammer-Aitoff projection of galactic coordinates. Note the high level of disagreement between the

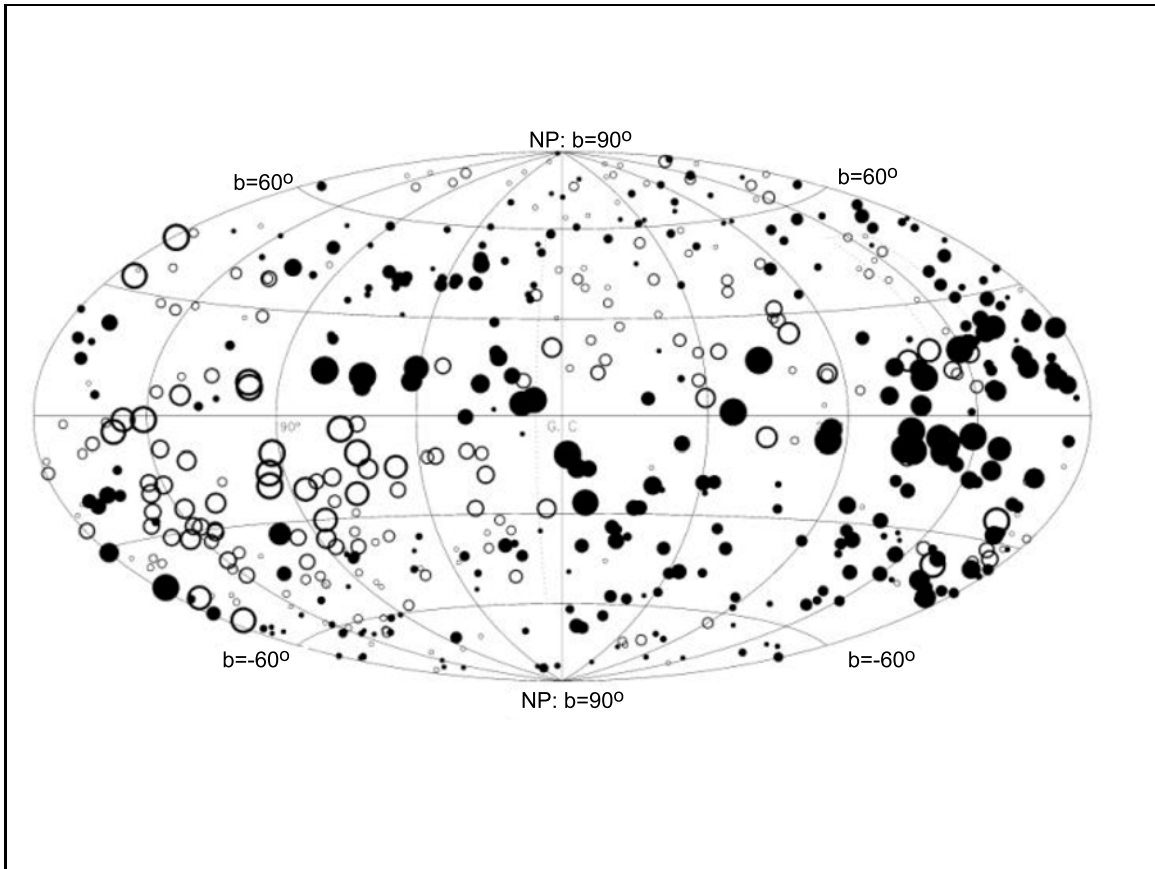


Figure 2.1. The averaged sky distribution of the RMs. Here filled symbols represent positive RMs, and open symbols represent negative RMs [24]

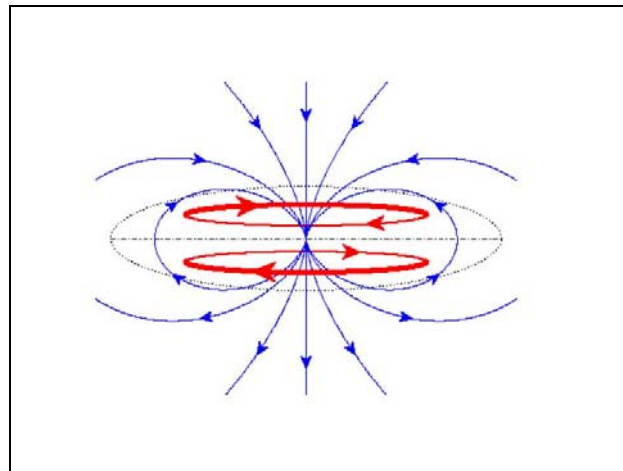


Figure 2.2. The A0 dynamo pattern [24]

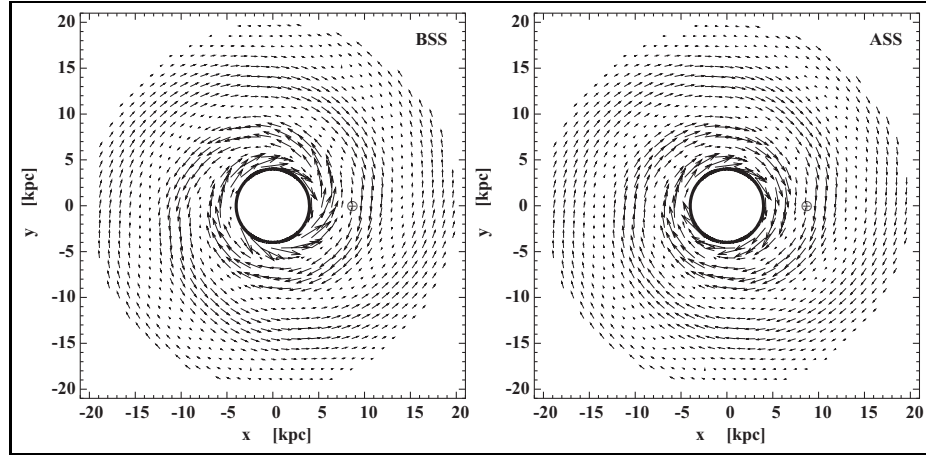


Figure 2.3. The spiral model of the GMF in the galactic plane. The left plot shows Bi-symmetric (BSS) spiral model while the right plot shows the axi-symmetric (ASS) spiral model. The location of the solar system is indicated by a small circle. [28]

maps. Furthermore, the GMF could be different from all these models. In order to locate CR sources, we need much better knowledge of our GMF [32]

2.3 Interaction With the IGMF

Even with all the uncertainties in the GMF, a particle with an energy of 10^{20} eV will exhibit sufficiently small bending that it can be traced back to a source if that source is within our galaxy. Therefore, our ability for doing ultra high energy cosmic ray astronomy depends upon our knowledge of the Inter Galactic Magnetic Field IGMF. The observations of the MF indicate that the IGMF is of order $\sim 1\mu G$ extending up to 1 Mpc from the galactic center [33]. Such observation are made through Faraday Rotation from polarized radio sources and/or synchrotron radiation from relativistic electron in the intra cluster MF. Galactic clusters only fill a small portion of the universe. However, they would cause a large deflection for charged particles that pass through the galaxies [34], [35]. In the rest of space, we only have the upper limit of the IGMF to be of order of 1-10 nG with coherence extending 50-100 Mpc, respectively [36]. Regardless, these bounds do not hold for clustered regions; such regions are filaments connecting clusters where the MF

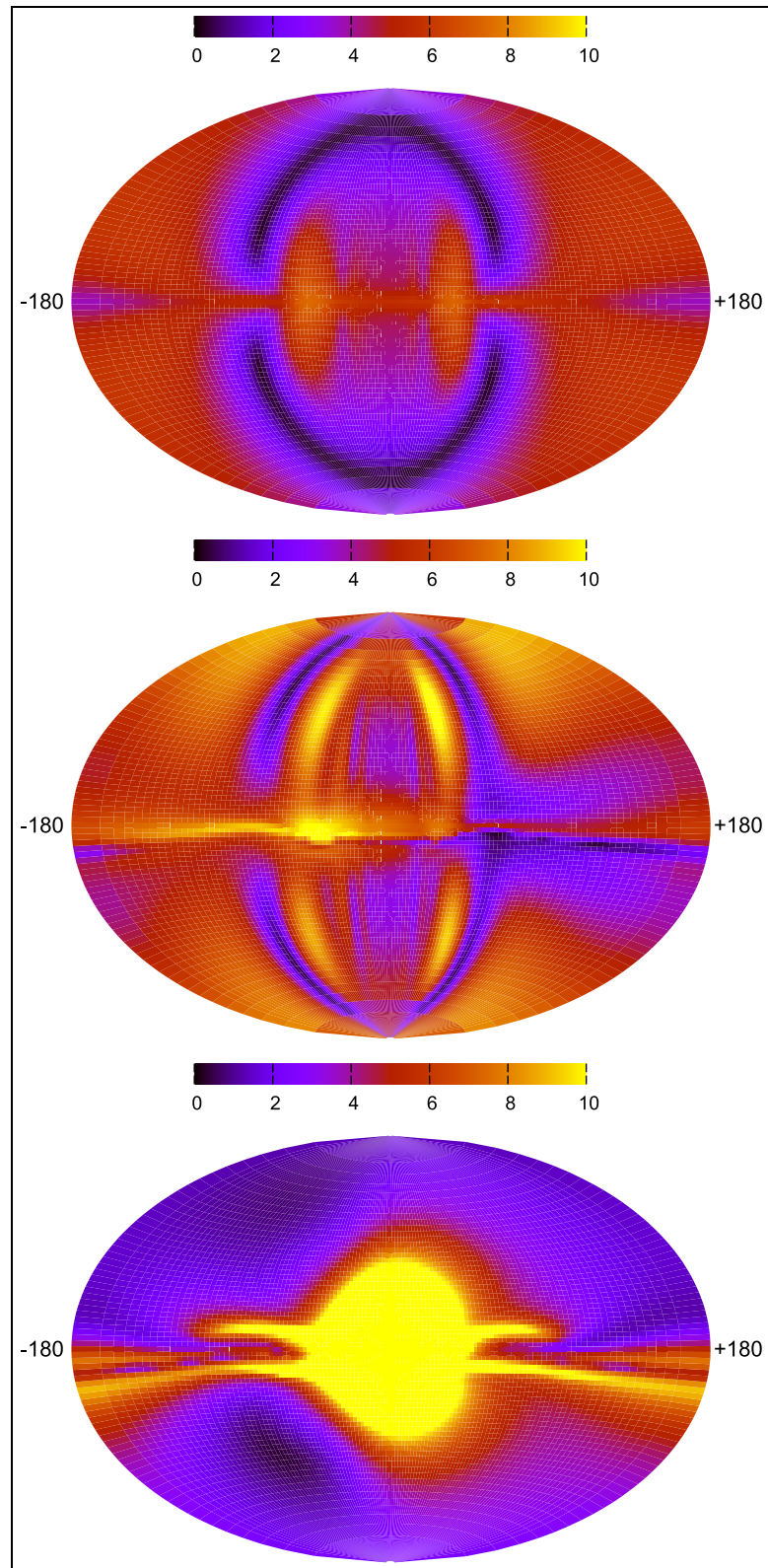


Figure 2.4. Three models of the GMF using different choices of parameters. The figure shows the deflection (as seen from the Earth) of protons with energy of 4×10^{19} eV propagated backwards 50 kpc away from the galactic center. The deflection maps are shown in the Hammer-Aitoff projection of galactic coordinates. The color index shows the size of deflection from 0 to 10 degrees [32].

might be as large as $10^{-7}G$. Therefore, to be able to do astronomy with protons we also need to have much improved knowledge of the large scale magnetic field of the universe.

Our knowledge of the MF structure in the IG space is limited, in part, due to the low density of the MF that makes it difficult to use indirect methods to make measurements. Theoretical predictions of the strength of the IGMF vary widely. For example, in Armengaud [37], the authors simulated MF from the shocks during large scale structure formation. Figure 2.5 shows the predicted deflection angles (left panel) and the time delay vs. straight-line propagation time (right panel) for protons injected with a spectral index of $\alpha = 2.4$. Note that protons with energy of 100 EeV have typical deflection on order of $10 - 40^\circ$. This large deflection is due to the expected large MF around the sources. Also note that typical time delays are also large, 1Gy at 10 EeV. Such time delays are too large to be directly measurable.

On the other hand, in a more optimistic study by Dolag [38], simulation reproduces the IGMFs using Magneto Hydrodynamics MHD to form the structures and the positions of known galactic clusters in the local universe.

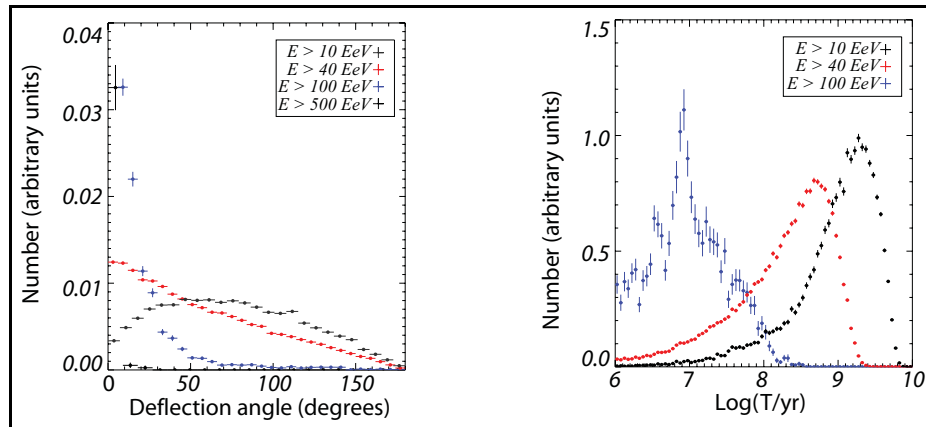


Figure 2.5. The predicted distribution of deflection angles (left panel) and time delay vs. straight-line propagation time (right panel) for proton injection particles with a spectral index of $\alpha = 2.4$. [37] Reprinted figure with permission from [E. Armengaud, G. Sigl, and F. Miniati, Ultrahigh Energy Nuclei Propagation in a Structured, Magnetized Universe, Phys. Rev. D72,043009, 2005] Copyright(2005) by the American Physical Society.

Figure 2.6 shows a full sky map of the predicted deflection angle for CRs with energy of 4×10^{19} eV for Dolag model. These particles are traced to a distance of 107 Mpc from the observer. In the figure, the deflection is represented by a color index where 0 degree deflection is presented by a dark color and 5 degree deflection is presented by light color. Note that large deflections of > 4 degrees are indicative of protons that pass through galactic clusters, e.g., Centaurus, Hydra, Perseus and Virgo. Such large deflections cover a small fraction of the sky. Outside the clusters, a deflection of $1^\circ - 2^\circ$ along network of filament. The main portion of the sky has a deflections $< 1^\circ$ that is due to MF $10^{-11}G$. Figure 2.7 shows a cumulative fraction of the sky with deflection larger than δ_{th} for several values of propagating distance. Note that deflection $> 1^\circ$ are predicted to be less than 20% of the sky for distances of 107 Mpc.

2.4 Interaction With the CMB

If the source of the CR particle is EG, the CR particle would have traveled very long distances. Along the way the CR would have high probability to interact with the CMB which, consequently, would result in degrading in the CRs energy and a deflection. This would limit the maximum distance over which ultra high energy CR astronomy would be possible.

2.4.1 Photons

The main energy loss mechanism for photons is Pair Production (PP). In PP, the CR photon combines with a CMB photon, to produce an electron positron pair:

$$\gamma + \gamma \rightarrow e^- + e^+ \quad (2.9)$$

the fate of the electron and positron depends upon the strength of the magnetic field. In a MF with strength $\sim 1nG$ the electron will lose its energy fast due to synchrotron radiation. However for a MF of 0.01 nG inverse Compton scattering is then possible. This would increase the attenuation length of the cosmic ray photons and make their detection possible.

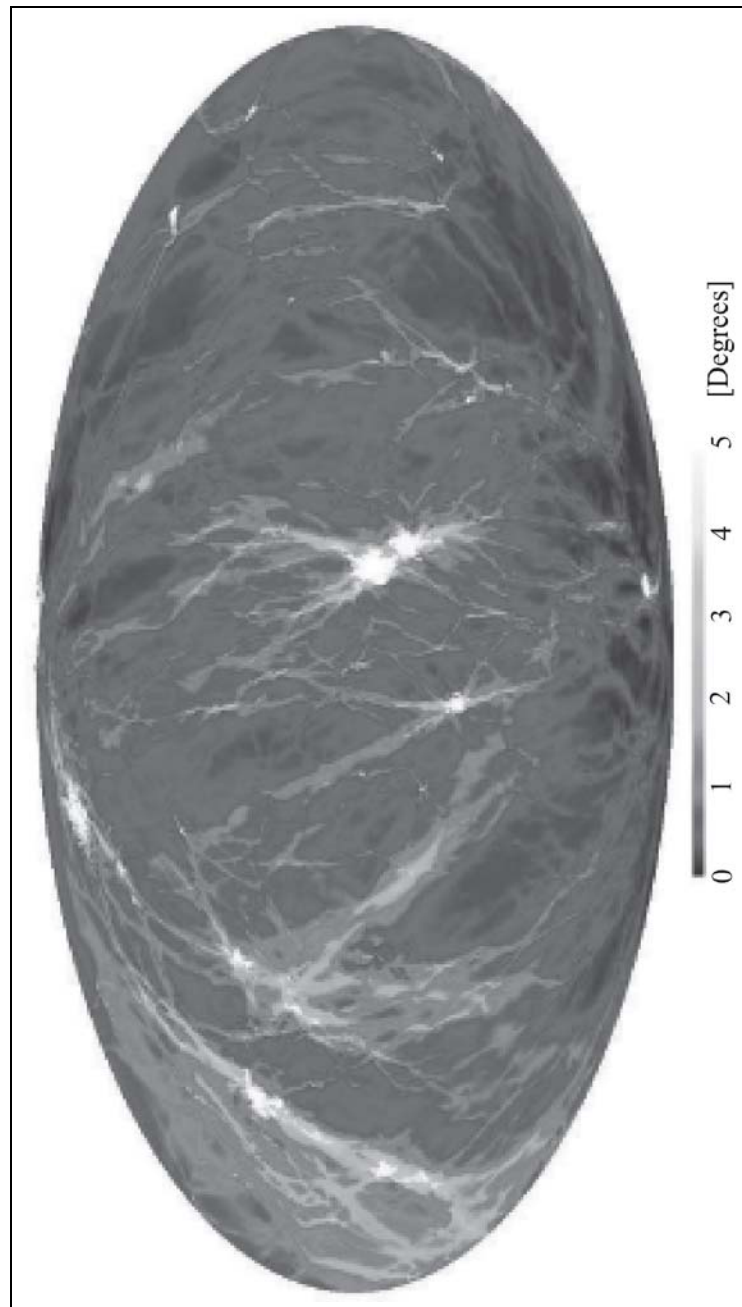


Figure 2.6. A full sky map of the predicted deflection angle for CRs with energy of 4×10^{19} eV. These particles are traced to a distance of 107 Mpc to the observer. Note that the deflection is represented by a color index where 0 degree deflection is presented by dark color and 5 degree deflection is presented by light color. [38] With kind permission of Springer Science and Business Media.

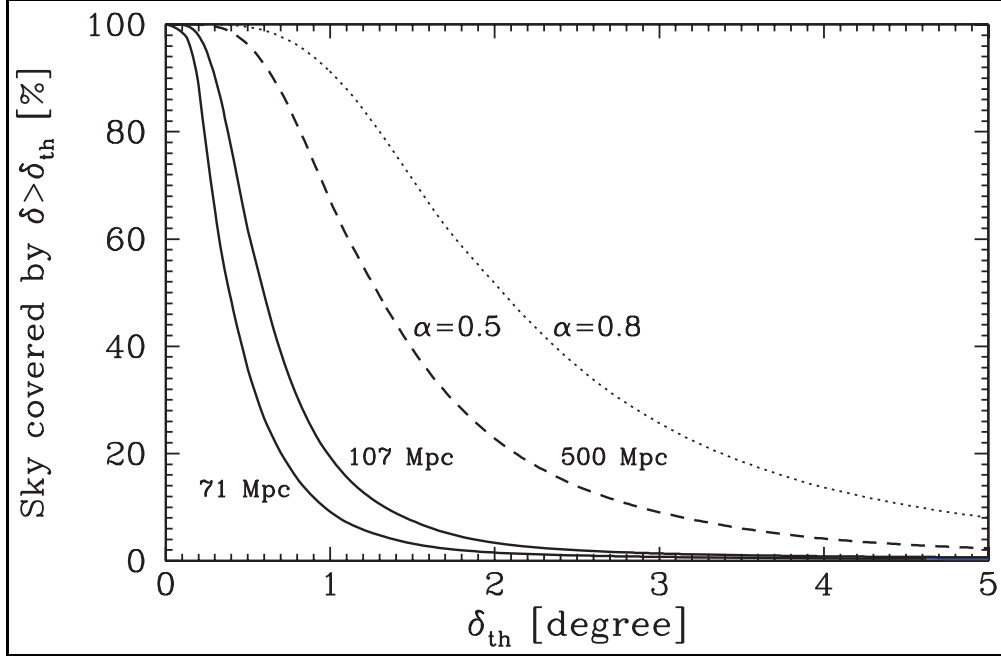


Figure 2.7. Cumulative fraction of the sky with deflection greater than δ_{th} for several values of propagating distance. [38] With kind permission of Springer Science and Business Media.

2.4.2 Protons

The dominant process in the proton interaction with the CMB is the formation of the Δ resonance which then decays to a lower energy, $\Delta(1236)$. This process produces a neutron and a positive pion or a proton and a neutral pion:

$$p + \gamma \rightarrow \Delta(1236) \rightarrow n + \pi^+ \quad (2.10)$$

$$p + \gamma \rightarrow \Delta(1236) \rightarrow p + \pi^0. \quad (2.11)$$

The creation of the pion rest mass along with its kinetic energy will necessarily act to reduce the energy of the proton or neutron. The neutrons will decay to protons with a decay length of ~ 1 Mpc at $10^{20} eV$:

$$L_{neutron\ decay} \approx 1 Mpc \frac{E}{10^{20}} eV, \quad (2.12)$$

thus resulting a proton. Figure 2.8 shows the energy of a proton as a function of its propagating distance. The figure shows that protons with energies 10^{20} will most likely not come further than 100 Mpc due to these interactions with the CMB.

2.5 Conclusion

In principle CR astronomy is possible for galactic sources if the particle is a proton and has an energy $> 10^{19}$ eV. On the other hand, if the CR particle is an iron nucleus, CR astronomy for galactic sources is only possible for energies $> 10^{20}$ eV. Neutral particles are the best probes CR sources, However, they make up a small fraction of the UHECRs. If we can collect a large number of events with energies 10^{19} eV a correlation with potential sources could be possible. As we move to EG sources more knowledge is needed with respect to the IGMF to determine our ability to do CR astronomy over such distance.

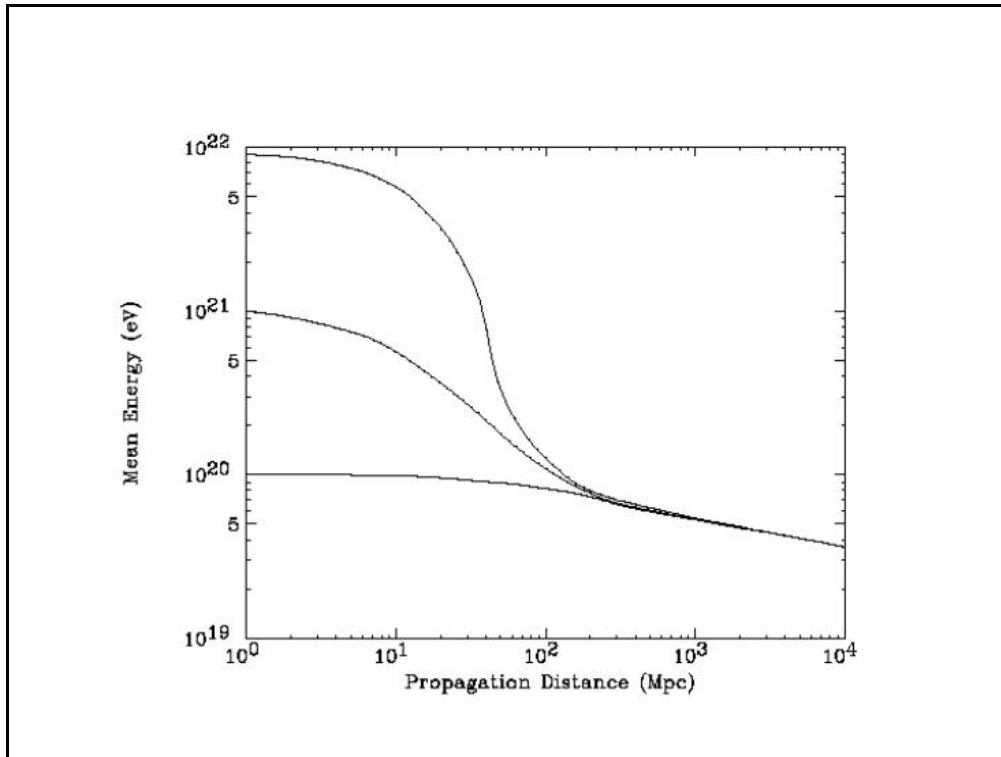


Figure 2.8. Energy of a proton as a function of the propagation distance [39]

CHAPTER 3

EXTENSIVE AIR SHOWER

3.1 Cosmic Ray Detection

The flux of CR at energies $> 10^{14}$ eV is approximately $1 \text{ particle}/m^2/\text{year}$. Such low flux makes direct measurements impossible. Therefore, in order to observe CR at such energies one need to use an indirect method to detecting CRs. The traditional method for doing this uses the shower of the particles produced when the CR particle collides with an atmospheric nucleus (nitrogen or oxygen). This shower is called an Extensive Air Shower (EAS) and it contains a large number of particles extending over hundreds of meters to several kilometers, hence the name EAS. By studying the cascade properties, we are able to infer information about the CR particle type, energy and arrival direction in the UHE region.

3.2 Shower Development

The shower primaries can be photons or nucleons (i.e., proton or iron). If the incident primary particle is photonic then an electromagnetic cascade will be generated. However, if the primary particle is nucleonic then the shower will have three components to its structure: hadronic, electromagnetic and muonic. A simple diagram of the EAS components is shown in Figure 3.1.

3.2.1 The Hadronic Component

The dominant hadronic production process is:

$$CR + N \text{ or } O \rightarrow \pi^{\pm,0} + K^{\pm} + \text{Hadrons}. \quad (3.1)$$

In a typical shower 2/3 of the particles are pions, 10% are kaons and the rest are hadrons such as protons and neutrons. Note that the hadronic component of the

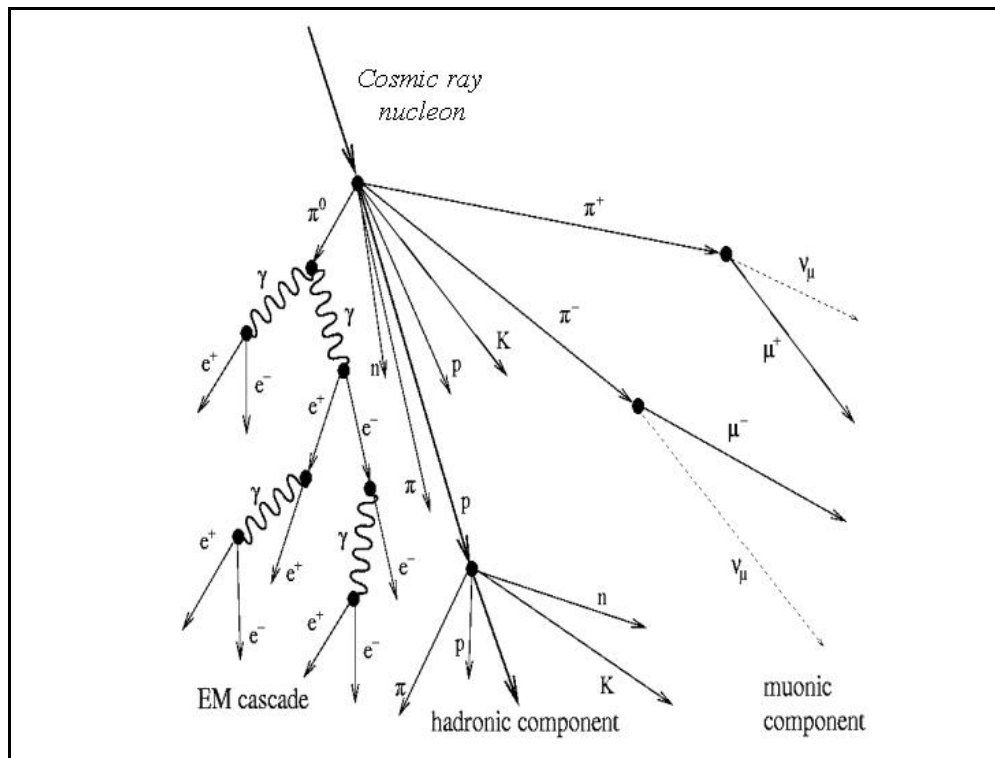


Figure 3.1. A simple diagram of the EAS components resulting when a CR nucleon interacts with the atmosphere. Here the shower cascade is divided into three components: electromagnetic, hadronic and muonic. Note how the hadronic component feeds the electromagnetic component via neutral pions which decay into a pair of photons. Likewise the hadronic part of the shower feeds the muonic component via the charged pions.

shower feeds both the electromagnetic and muonic components of the shower via the decay of neutral and charged pions, respectively.

3.2.2 The Electromagnetic Component

The electromagnetic component of the shower starts either when the incident primary CR particle is a photon or when a neutral pion from the hadronic component decays instantaneously to a pair of photons. Each photon cascades electromagnetically. A photon of energy E_o , produces an e^+e^- pair, each with an equal energy of $E_o/2$. On average each electron will produce an additional photon, via bremsstrahlung, having the average energy $E_o/4$. This process will continue until the average energy per particle is equal to E_c , the critical energy.

The critical energy is the energy at which the dominant energy loss mechanism is via ionization rather than bremsstrahlung; ~ 82 MeV. Beyond this point the shower no longer grows. The shower has reached what is referred to as shower max, the number of particles in the shower has reached a maximum, N_{max} . Beyond this point, the shower begins to attenuate.

Most of the energy found in the shower (a measure of the energy of the incident primary particle) is found in the electromagnetic component. The energy of the electrons and positrons in the EAS is dissipated through ionization losses with the atmosphere. The electromagnetic energy E_{em} is then calculated by integrating the number of charged particles $N(X)$ along the length of the shower track (X):

$$E_{em} = \alpha \times \int N(X) dX \quad (3.2)$$

where α is the energy loss per unit path-length in the atmosphere.

3.2.3 The Muonic Component

The muonic component of the shower is directly coupled with the hadronic component of the EAS since it is mainly produced with the decay of charged pions ($\pi^\pm \rightarrow \mu^\pm + \nu$). Another source is the decay of charged kaons to pions which in turn would decay to muons.

The number of muons in a shower depends upon the incident CR particle's mass and energy. For instance, photon showers contain only 5% as many muons

as found in a nucleon generated shower. Likewise, iron showers contain 80% more muons than proton generated showers with the same energy. This fact is applied in estimating the composition of the shower primary via measurements from ground array detectors.

3.3 Shower Parameters

The High Resolution Fly's Eye (HiRes) is a fluorescence detector, it utilizes the atmosphere as a calorimeter. A fluorescence detector observes the EAS using the fluorescence light produced by the charged particles in the shower. The charged particles excite the nitrogen molecules in the atmosphere, then when the nitrogen molecule relaxes in decaying back to the ground state it emits a broad spectrum of light. The majority of this light is emitted in the near Ultra Violet UV-light (300-400 nm). The nitrogen emission spectrum is shown in Figure 3.2 [42].

Reconstructing the shower's development, we determine the number of photons vs. the slant depth of the shower, X . We estimate the number of electrons in the shower, N_e . Then using equation 3.2, we calculate the electromagnetic energy $E_{em} = \alpha \times \int N_e(X) dX$, where $\alpha = 2.2 \text{ MeV}/(g \text{ cm}^{-2})$. Unfortunately, we cannot integrate along the entire shower length since the detector only views a portion of it. Therefore, to reconstruct the shower energy and composition we perform a fit to the shower parameters for the longitudinal profile and lateral distribution of the shower.

3.3.1 Longitudinal Shower Distribution

The number of electrons at each point of shower development, N_e , can be represented as a function of the slant depth, by a Gaisser-Hillas function [40]:

$$N_e(X) = N_{max} \left(\frac{X - X_o}{X_{max} + X_o} \right)^{(X_{max} - X_o)/\lambda} \exp \left(\frac{X_{max} - X}{\lambda} \right), \quad (3.3)$$

where N_{max} is the number of particles at the shower maximum, X_o is the depth of the first interaction, X_{max} is the point of maximum shower development (in gm/cm^2), and λ is a constant equal to $70 \text{ gm}/\text{cm}^2$.

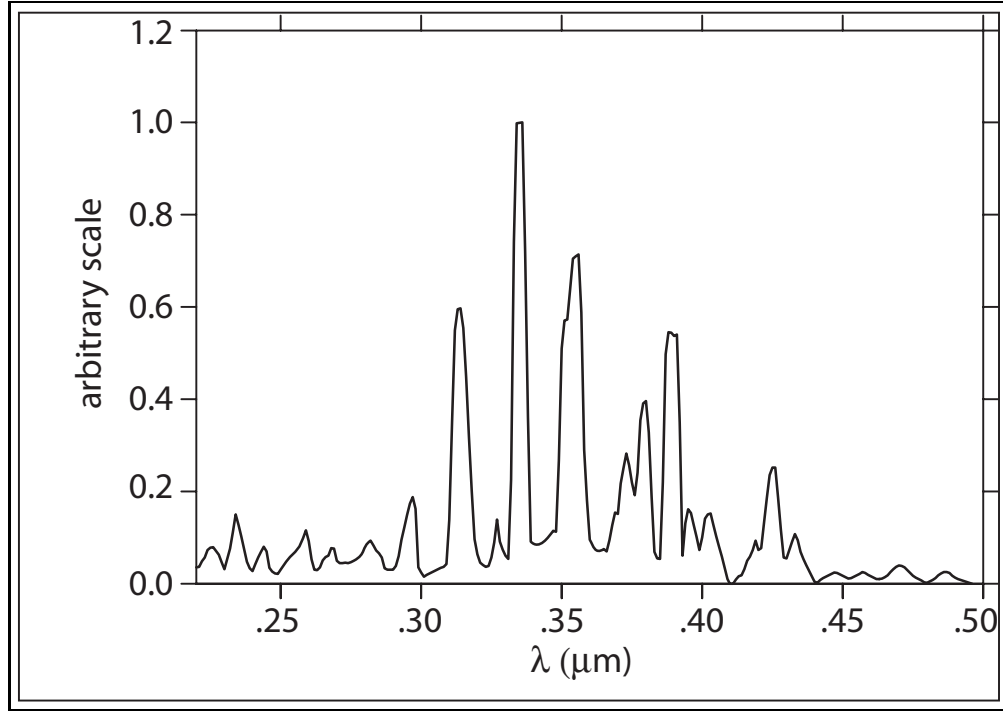


Figure 3.2. Nitrogen fluorescence spectrum as compiled by Bunner [42].

Note that the point of the first interaction depends upon the particle's cross section which in turn is dependent upon the particle's composition and energy. Likewise, X_{max} depends upon the particle's initial interaction position X_o , energy and composition. The depth of the shower maximum, X_{max} , evolves linearly with the logarithm of the energy of the primary. This dependence is referred to as the elongation rate for primaries between 10^{17} eV and $10^{19.5}$ eV. Figure 3.3 shows the predicted and the measured elongation rate. It shows the shower Mean elongation rate X_{max} (gm/cm²) vs. $\log(E(\text{EeV}))$ for HiRes stereo data is shown in triangles. The predicted elongation rate using the SYBIL and QGSJet models shown in open circles and square consequently. The prediction is shown of protons and iron. The stars shows the HiRes prototype result. As one can see, the composition is measured to be primarily heavy (iron-like) around 10^{17} eV. However, it becomes increasingly lighter with energy [43].

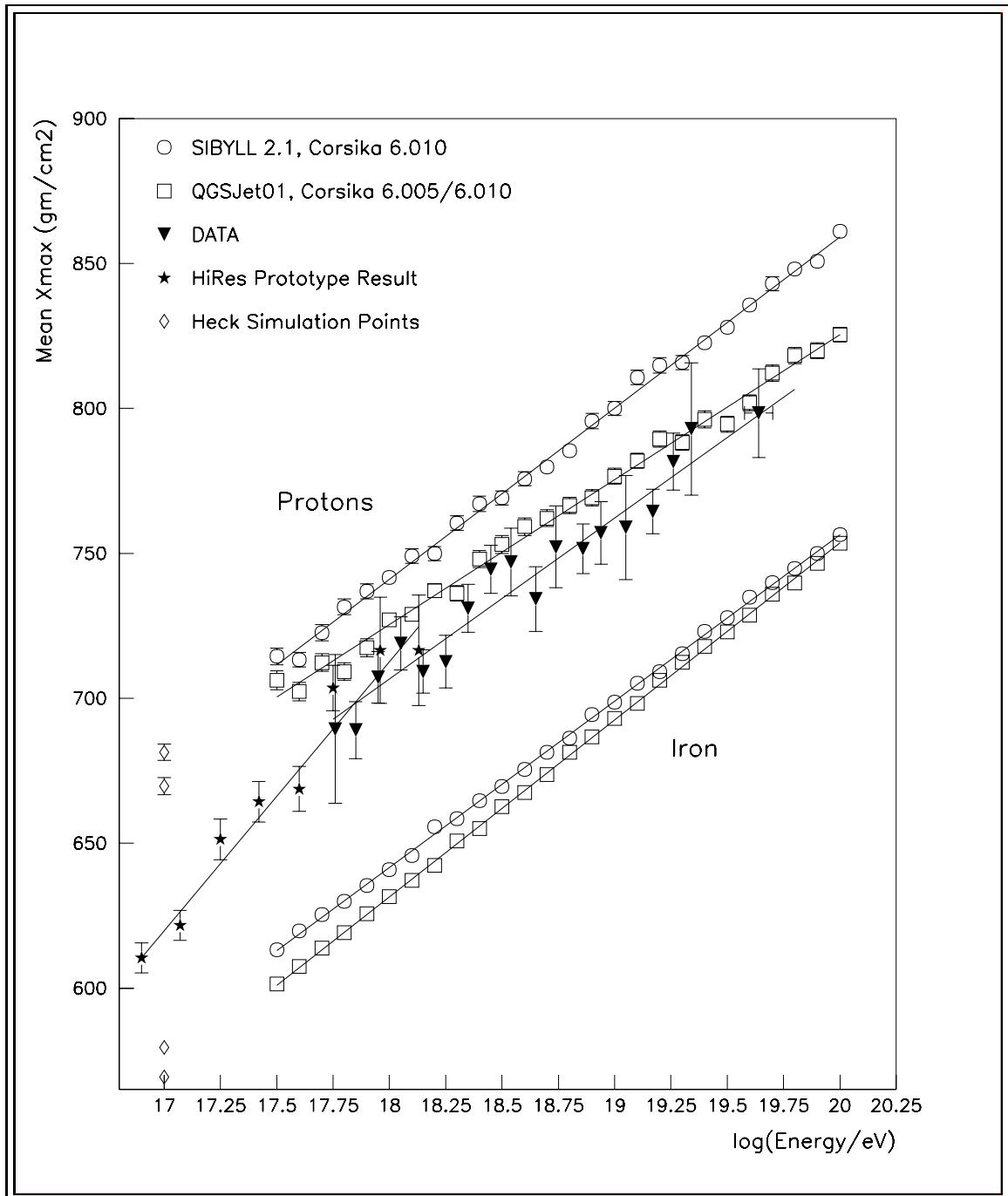


Figure 3.3. The shower mean elongation rate X_{max} (gm/cm^2) vs. $\log(E(\text{EeV}))$ for HiRes stereo data is shown in triangles. The predicted elongation rate using the SYBIL and QGSJet models shown in open circles and square consequently. The prediction is shown of protons and iron. The stars shows the HiRes prototype result. As one can see, the composition is measured to be primarily heavy (iron-like) around 10^{17}eV . However, it becomes increasingly lighter with energy. [43]

3.3.2 Lateral Distribution

The shower electron lateral distribution (density) is parameterized by [41]:

$$\rho(r) = \frac{N}{r^2} f\left(s, \frac{r}{r_m}\right) \quad (3.4)$$

where N is the total number of electrons, and s is the shower age given by $s = 3/(1 + 2X_{max}/X)$. Here X and X_{max} are shower depths measured from the point of the first interaction, r_m is Moliere radius for multiple scattering, and f is the Nishimura-Kamata-Greisen (NKG) function. The NKG function is:

$$f\left(s, \frac{r}{r_m}\right) = \left(\frac{r}{r_m}\right)^{(s-2)} \left(1 + \frac{r}{r_m}\right)^{(s-4.5)} \left(\frac{\Gamma(4.5-s)}{2\pi\Gamma(s)\Gamma(4.5-2s)}\right) \quad (3.5)$$

where Γ is the standard gamma function.

3.4 Čerenkov Light

In most showers the light received by the detector is the superposition of the fluorescence light and the Čerenkov light. Čerenkov light is produced when a charged particle travels through a medium with a velocity that is faster than the speed of light in that medium. The angle of emission for Čerenkov light is given by:

$$\cos\theta = \frac{1}{\beta n}, \quad (3.6)$$

where n is the index of refraction and $\beta = \frac{v}{c}$ where v is the particle velocity and c is the speed of light. This is typically a very small angle. This behavior means that the amount of Čerenkov light received at the detector increases direction of the shower points more toward the detector. It is therefore necessary to estimate the Čerenkov light effect and subtract it from the light signal.

Both the Čerenkov light and the fluorescent light are affected by scattering via the atmosphere. In order to understand the light signal received from the shower we need to estimate the scattering of the light. We need to consider two cases: first, the scattering of the Čerenkov light along the shower direction and second, the scattering of fluorescent and Čerenkov light as they travel from the shower to the detector. In both cases there are two scattering mechanisms, Rayleigh scattering and Mie scattering.

Rayleigh scattering (molecular scattering) at any wavelength depends upon the atmospheric density. In general the atmospheric density is well known and changes little over time. For Mie scattering (aerosol scattering) it is dependent on the density and size of the matter distribution in the atmosphere. Such distributions are variable with time and location. Therefore, a good understanding of the atmosphere is necessary to understand the detected light signal from the shower.

Figure 3.4 illustrates the above ideas. It shows light signal vs. atmospheric depth for a simulated shower with an energy of 10^{19} eV. The simulation included a cut on the wavelength 300-400 nm. The figure shows the total light as well as the contributions from fluorescent light, scattered Čerenkov light and direct Čerenkov light [45].

All of these processes need to be measured and their effects calculated in order to reliably reconstruct the energy and composition of the primary. Despite these challenges the fluorescence technique has the great advantage of viewing the shower track development over many kilometers in the atmosphere. This enables one to make a much more accurate measurement of the arrival direction. This is much amplified if the observation of the shower is made by stereo detectors. In addition, this is a true calorimetric measurement of the energy deposited (albeit with certain assumptions and corrections such as critical and missing energy). While the analysis that follows will not make detailed use of the energy measurement, it greatly benefits from the accurate measurement of the pointing direction.

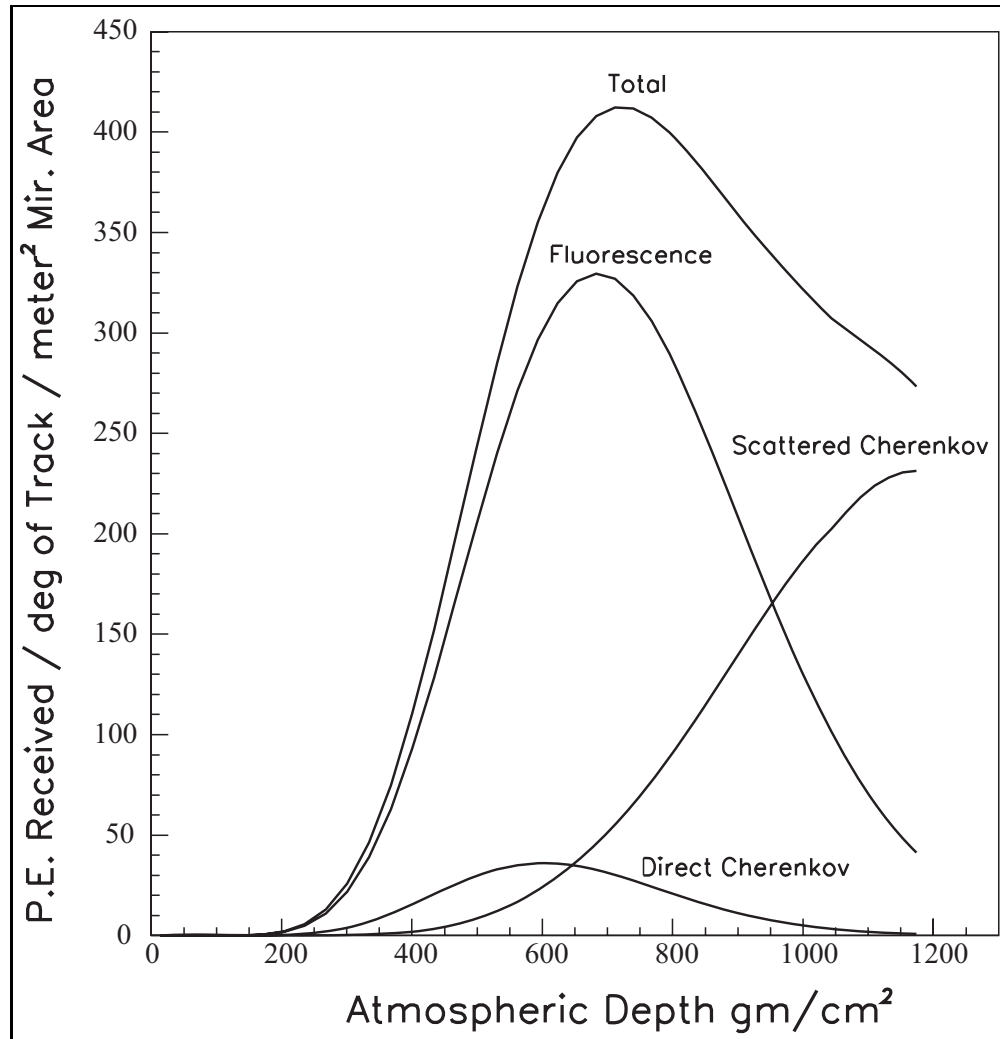


Figure 3.4. The simulated light signal vs. atmospheric depth for a shower of 10^{19} eV. The simulation included a cut on the wavelength 300-400 nm light. The figure shows that the total light is a contribution of fluorescent light, scattered Čerenkov light and direct Čerenkov light [46]

CHAPTER 4

THE HIRES DETECTOR

4.1 Introduction

The High Resolution Fly's Eye Experiment is located in the U.S. Army Dugway Proving Ground (DPG) in Utah. It consists of two observatory sites: HiRes-1 which sits atop Little-Granite mountain, and HiRes-2 which is located on Camel's Back Ridge. The two sites are separated by 12.6 km. The western Utah desert location at DPG was chosen for its clean atmosphere, clean, dry weather, and low light pollution. The HiRes-1 detector began operation in 1997 in monocular mode. Observation at HiRes-2 followed in 1999 with the stereo operation starting in November, 1999. The HiRes experiment collected data separately at each of the two sites. The two data acquisition systems were different and the data were stored separately.

At analysis time, the data could be processed in three possible streams. First, the data could be processed in monocular mode using the information from either one of the individual observatory sites. Additionally, the information from both sites could be used simultaneously to make a stereo reconstruction of the events. The monocular data sets contain for greater statistics, but also greater geometrical reconstruction uncertainty. In the analysis described in this dissertation, we will use the stereo reconstruction which has much more precise geometrical reconstruction. In this chapter we will describe the HiRes detector, atmospheric monitoring, and calibration.

4.2 HiRes-1 and HiRes-2

HiRes-1 is comprised of 22 telescopes in a single ring geometry. They have full azimuthal coverage for the angles between 3° and 17° above horizon. Likewise, HiRes-2 consists of 42 cameras in a two-ring geometry (one ring over the other). It also has full azimuthal coverage, but covers from 3° to 31° above horizon.

Each telescope contains a mirror, Photo Multiplier Tubes (PMTs) and Data-Acquisition (DAQ) electronics (see Figure 4.1). Each mirror is assembled from four spherical segments with a total mirror area of $5.02m^2$. After taking the shadowing of the cluster into account, the mirror's effective area is $3.72 m^2$ [42]. The PMT camera is built from 256 hexagonal PMTs (16×16) in hexagonal close pack (honey comb) geometry, as shown in Figure 4.2. Each PMT is $40 mm$ flat to flat and view a 1° cone of the sky. A camera then views a 16° azimuth by 14° elevation piece of the sky. A UV band pass filter is placed in front of the PMTs to enhance signal to noise ration [47]. This blocks most visible light, but has high transmission for 300-400 nm .

The data acquisition system for HiRes-1 uses Sample-and-Hold (S&H) electronics, and it records the integrated charge and triggering time if the integrated charge passes through a threshold level and meets a $5.6\mu s$ time gate [48]. Afterwards the trigger logic board we then decides whether to pass the the tube's trigger to a mirror trigger by comparing the trigger to preset patterns [[49], [50]]. When a mirror trigger is issued the charge and timing information is gathered, digitized and sent to the DAQ computer.

HiRes-2 detector on the other hand uses the Flash Analog to Digital Converter FADC module to digitize the triggered signal every $100 ns$ with a delay buffer of $820 \mu s$. Note that for the signal to be digitized it needs to be greater than or equal to a trigger threshold. After that the data go through tighter triggering criteria. Once the FADC data pass these cuts they are sent to the DAQ computer. With this system HiRes-2 has many advantages over HiRes-1 such as wide delay buffer, minimal analog processing, and dead-timeless readout of all channels from before the event until after the event [51].



Figure 4.1. A picture of a detector building at the HiRes-2 observatory. Each building is approximately the size of a two-car garage. The mirrors are each made of four segments giving them a “clover leaf” appearance. The spherical mirrors are each approximately $2m$ in size and focus the light onto the PMT camera approximately 92 inches in from the center of the mirror. An electronic rack may be seen at the far right in the building.

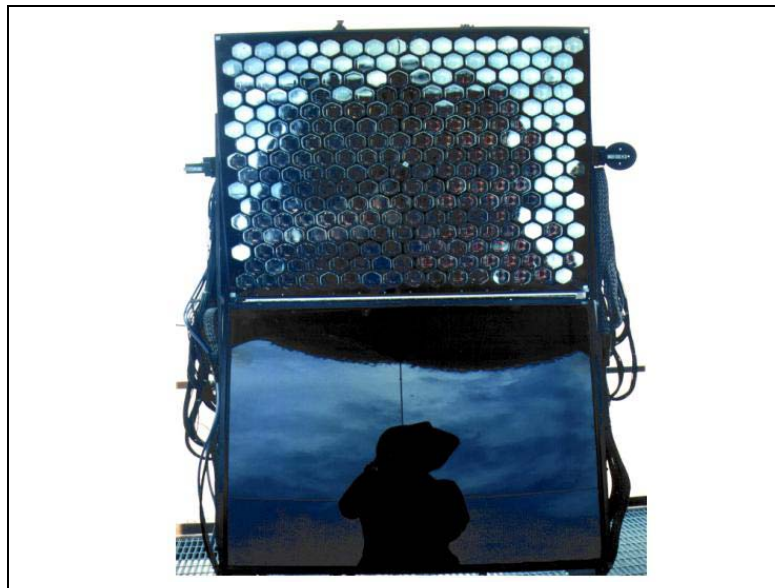


Figure 4.2. This figure shows a PMT cluster. It contains 256 (16×16) hexagonal-faced PMTs. Below the PMT camera we see a reflection of the photographer in the UV band pass filter which has been lowered to show off the PMTs.

Figure 4.3 and 4.4 show HiRes-1 and HiRes-2 events display. An observed event is shown in the display as seen by the two detectors. Mirror numbers are indicated next to each mirror. The up direction represents the north, the center of the display represents the zenith while the outer edge represents the horizon.

4.3 Calibration

Routine calibration of the HiRes PMTs and monitoring of the electronics are essential to maintain a correct understanding of the collected data. The primary way of calibrating the PMTs is using the Roving Xenon Flasher (RXF). The RXF has its many advantages: (1) It is easily transportable, (2) the pulse-to-pulse variation is very small $\approx 0.3\%$, (3) it remains within 2% stability over night, (4) it has a wide emission spectrum that permits calibration over a broad spectrum of wavelengths [52].

The PMTs are calibrated using the RXF. It is a long project that is performed on poor weather nights once a month. The calibration process starts with calibrating standard PMTs against NIST calibrated diode ([53], [54]). Later on, the RXF is placed in the center of the mirror uniformly illuminating the whole cluster of PMTs. The response of the PMTs is then compared to that of the standard PMTs. Such comparison would give us the absolute responsiveness of the PMTs.

The PMTs responsiveness is calculated using different density filters between the RXF and the PMTs. The RXF fires several hundred times for every filter. The mean number of photoelectrons μ_{pe} is then calculated using Poisson statistics where:

$$\mu_{pe} = \alpha \frac{\mu_{QDC}^2}{\sigma_{QDC}^2} \quad (4.1)$$

where $\alpha^{1/2}$ is the PMT excess noise factor, μ_{QDC} is the mean of the charge to digital converter QDC value, and σ_{QDC} is the standard deviation of the QDC value. Figure 4.5 shows a calibration plot for a single PMT. It shows the pedestal-subtracted QDC count vs. the mean number of photoelectrons (subtracted from equation 4.1) for different density filters [55]. A linear fit is then applied, and the tube QDC photoelectrons conversion is then found from the inverse of the slope of

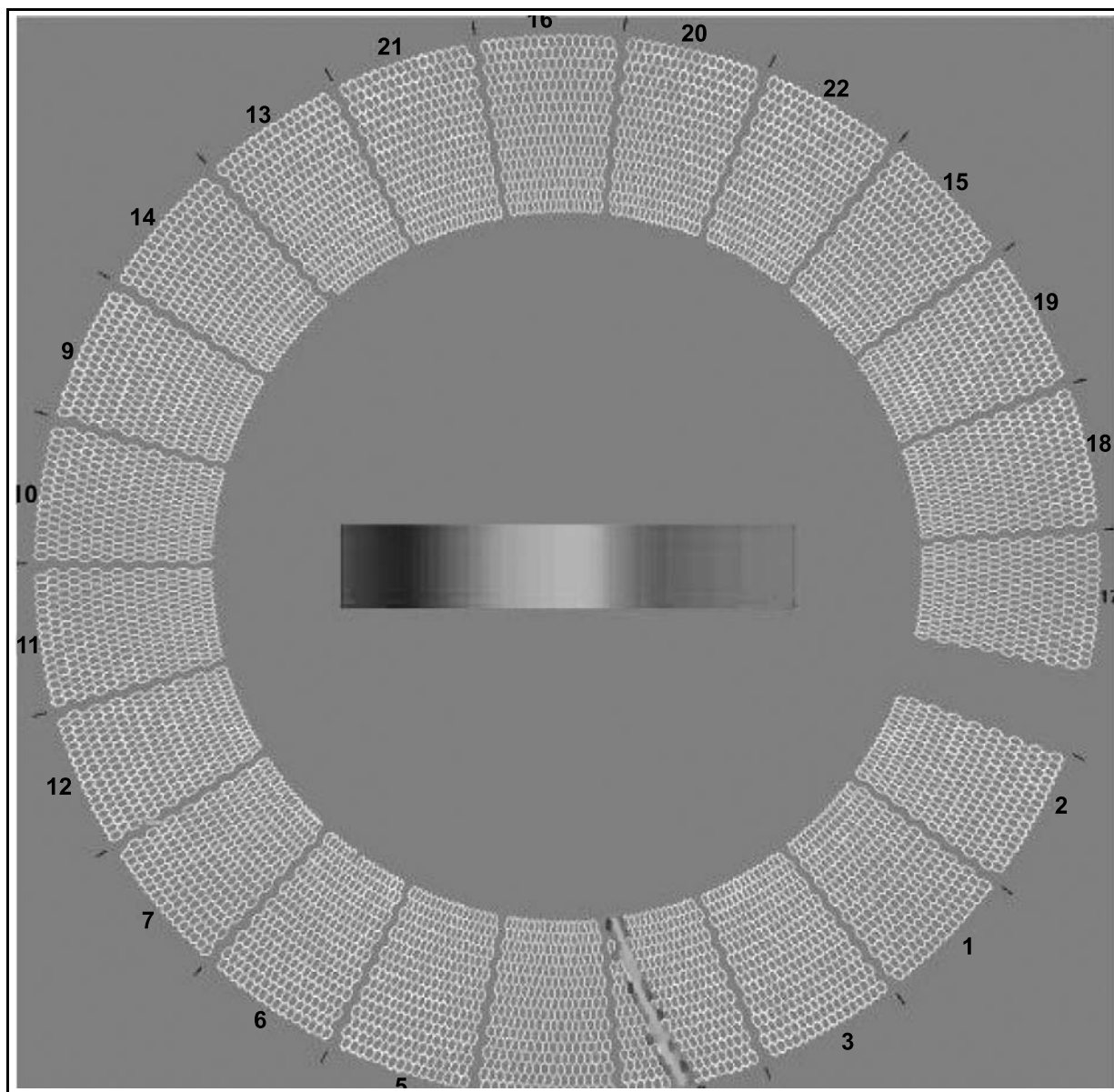


Figure 4.3. HiRes-1 event display. The field of view of each telescope is shown as a trapezoid consisting of 265 pixels. In the event display, up is the north and right is the east. The center of the plot is zenith. The outer parameter is 3° above horizon and the inner ring is 17° above horizon. The event, shown here in mirror 3, shows up as a track. Color is used to indicate the amount of light observed by the pixel.

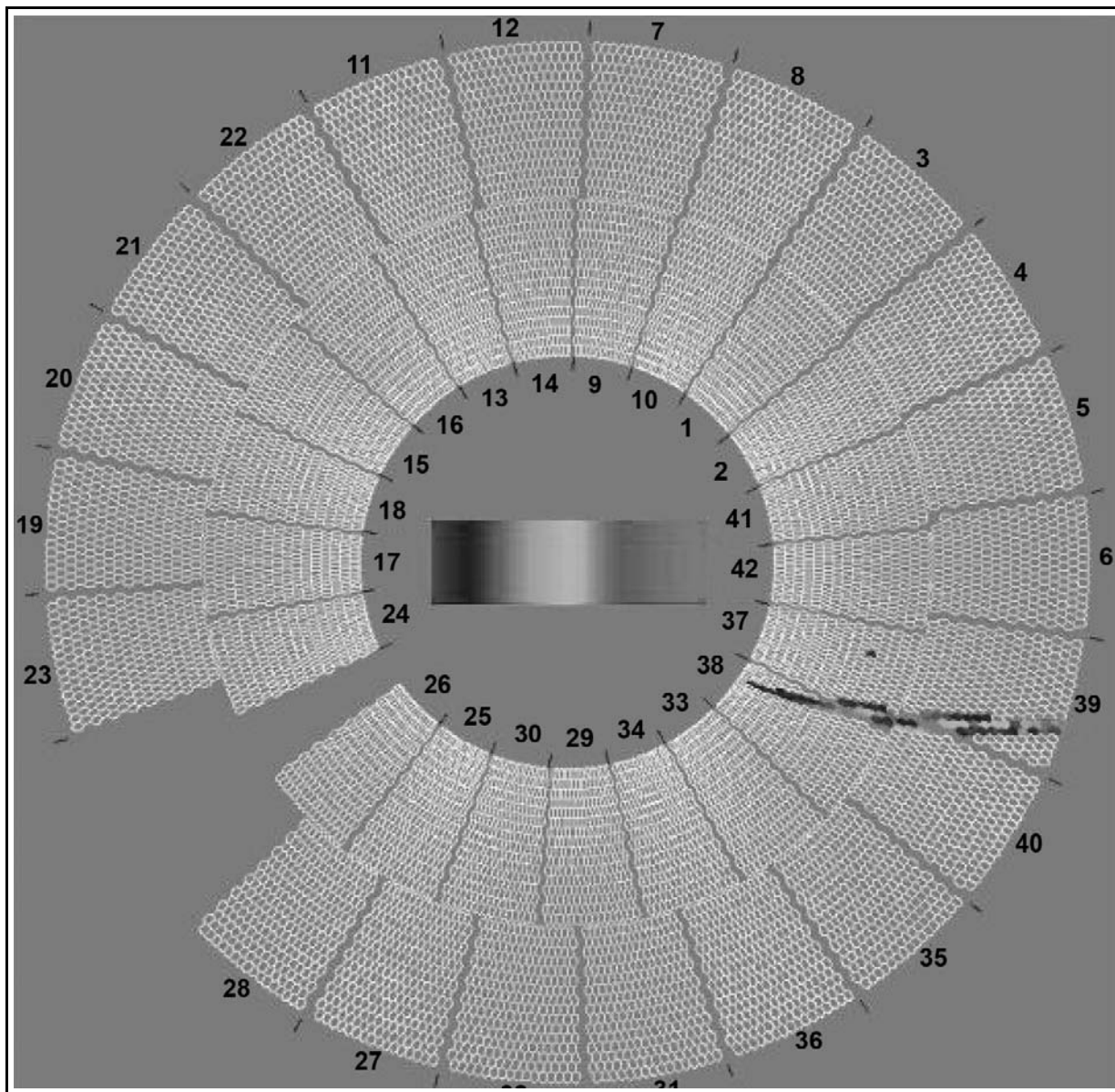


Figure 4.4. HiRes-2 event display. The HiRes-2 display is similar to the HiRes-1 display in that up is north, right is east, and the center is zenith. In this display, we note the “two ring” geometry of the HiRes-2 detector so that the inner ring is at 31° above horizon. This obviously allows one to view more track length especially for lower energy events. This provides more timing information and gives greater accuracy in geometrical reconstruction.

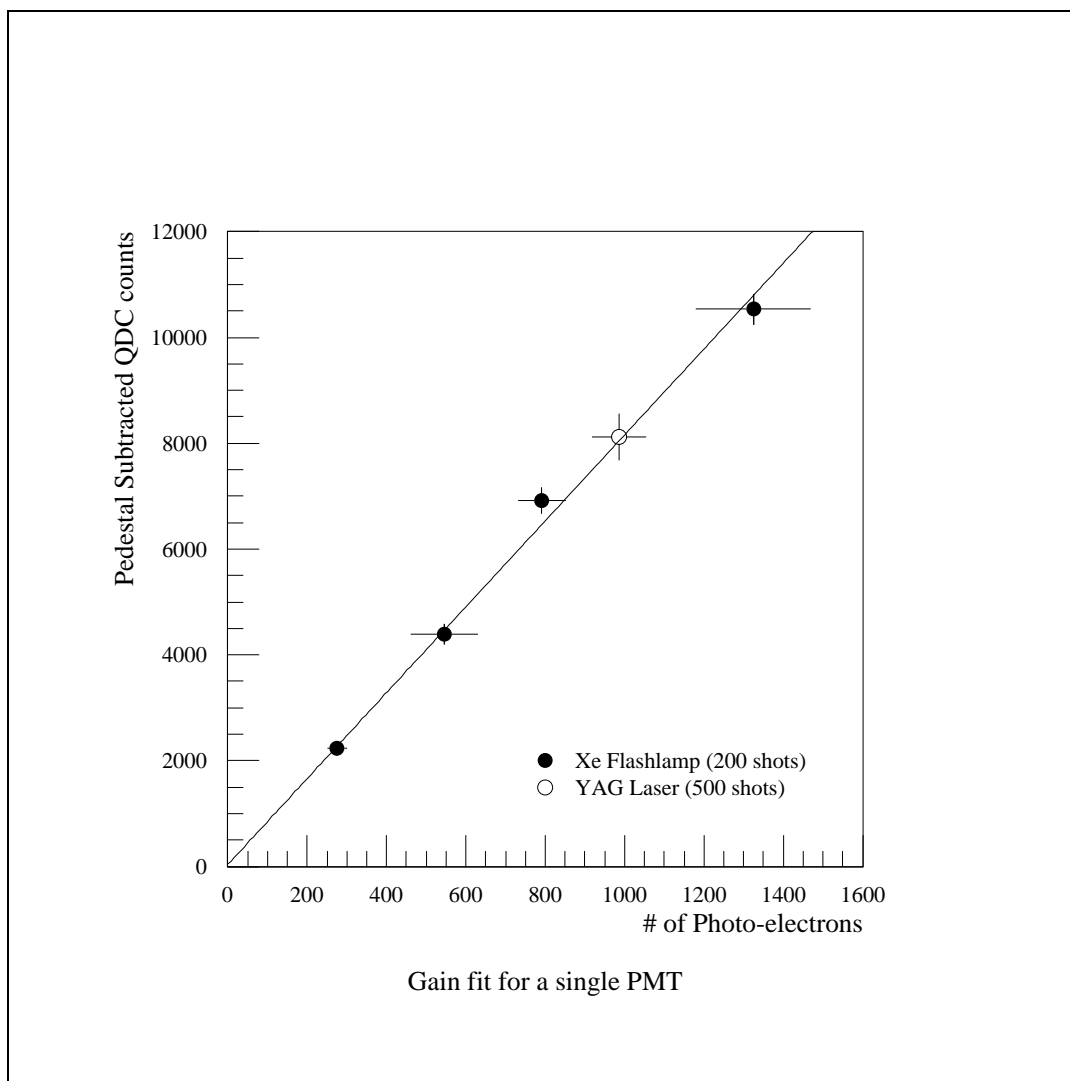


Figure 4.5. The pedestal subtracted QDE count vs. the mean number of photo-electrons for a single PMT. A linear fit is applied, and the tube DSC photoelectrons conversion is the inverse of the slope of the line. Note that the YAG laser value is consistent with the RXF calibration fit [53].

the line. Note the calibration point using the Yttrium Argon Gallium YAG laser (discussed below) is consistent with the RXF calibration fit.

One disadvantage in using the RXF as means of calibration is that it is time consuming and labor intensive. Therefore such monitoring cannot be achieved on a nightly basis. Hence, a YAG laser system is used simultaneously for all cameras before and after collecting data. The YAG laser delivers light at 355

nm to each camera via optical fibers. For every camera there are three sets of fibers, one set connected to the mirror and one set to each side of the PMT cluster. The one that is connected to the mirror illuminates the PMTs directly and allows measurement of their response, while the ones connected to each side of the cluster will illuminate PMTs indirectly via the mirror, and thus allows determination of mirror reflectivity [56].

4.4 Atmospheric

As mentioned in the previous chapter, within the atmosphere there are two types of scattering: Rayleigh scattering and Mie scattering. The Rayleigh scattering is light scattered by the air molecules. Such scattering varies with the angle of emission and atmospheric pressure. Rayleigh scattering is well understood and the pressure used is the one described by the “1976 US standard atmosphere” model. On the other hand, Mie scattering is due to the aerosols such as dust, haze, and everything else that is not molecular. Mie scattering is more challenging to account for since it changes by elevation on a short time scale. A constant monitoring of the atmosphere is necessary in order to account correctly for the contribution of the scattering to the detected light signal. The methods used for atmospheric monitoring are a cloud monitor, xenon flashers and steerable YAG laser.

4.4.1 Cloud Monitor

The runners are supposed to check and report the weather and the cloud coverage on an hourly basis. This should provide a subjective knowledge of the weather status. In addition, there exist at HiRes-1 stationary $30^\circ \times 30^\circ$ infra-red cloud monitors that are installed on half of the buildings. The monitors indicate if clouds are in the FOV by measuring their temperature (the clouds are warmer than the rest of the sky). Furthermore a finer resolution full sky coverage cloud monitor is also mounted. This monitor is mainly used for the remote runner of HiRes-1 to get a feeling on the sky status. As for HiRes-2, the clouds are visible through FADC snapshot, so no other cloud monitors are implemented.

4.4.2 Xenon Flashers

Ten vertical xenon flashers are mounted between HiRes-1 and HiRes-2 in two rows. Another inclined xenon flasher is mounted NNE of HiRes-1. A map of the flashers is shown in Figure 4.6. The flashers are radio signal controlled from HiRes-2. A more detailed description of the xenon flasher system is found in [58]. Xenon flashers are used as a rough estimation to determine the acceptability of the observed data.

When Xenon flashers are fired it is vital that both detectors see the flash at the same time. If not, it might imply that the detectors are not synchronized correctly. It might also imply that the aperture is too hazy. The detected flashes also provide qualitative information about the atmosphere. For example, if a vertical flash hits a cloud it will create a mushroom shaped signal display. Moreover, if a flash signal is too broad, that would imply a thick aerosol content in the atmosphere.

4.4.3 Steerable Lasers

Although the intersite flashers are easy to use and implement we cannot rely on them in understanding the atmospheric scattering. Because that the intersite flasher covers a small portion of the atmosphere. Hence, the steerable laser is used.

There are three steerable (YAG) laser systems. The first is mounted at HiRes-1 and is viewed by HiRes-2. The second is identical and is mounted at HiRes-2 and is seen by HiRes-1 detector. The third is a roving steerable laser that is a portable system and is the only laser that can be seen by both detectors.

The steerable laser fires every hour in a predetermined direction as shown in Figure 4.7. The laser covers 25 kilometers into the FOV sweeping most of the aperture. The steerable laser fired from one detector is seen by the other as shown in Figure 4.8. From the attenuated light we are able to account for the amount of light lost between the laser and the detector “missing light” due to the aerosol scattering. Such calculation is simply made by determining the light missing in excess of the amount expected from molecular scattering. Technique description can be seen at [59].

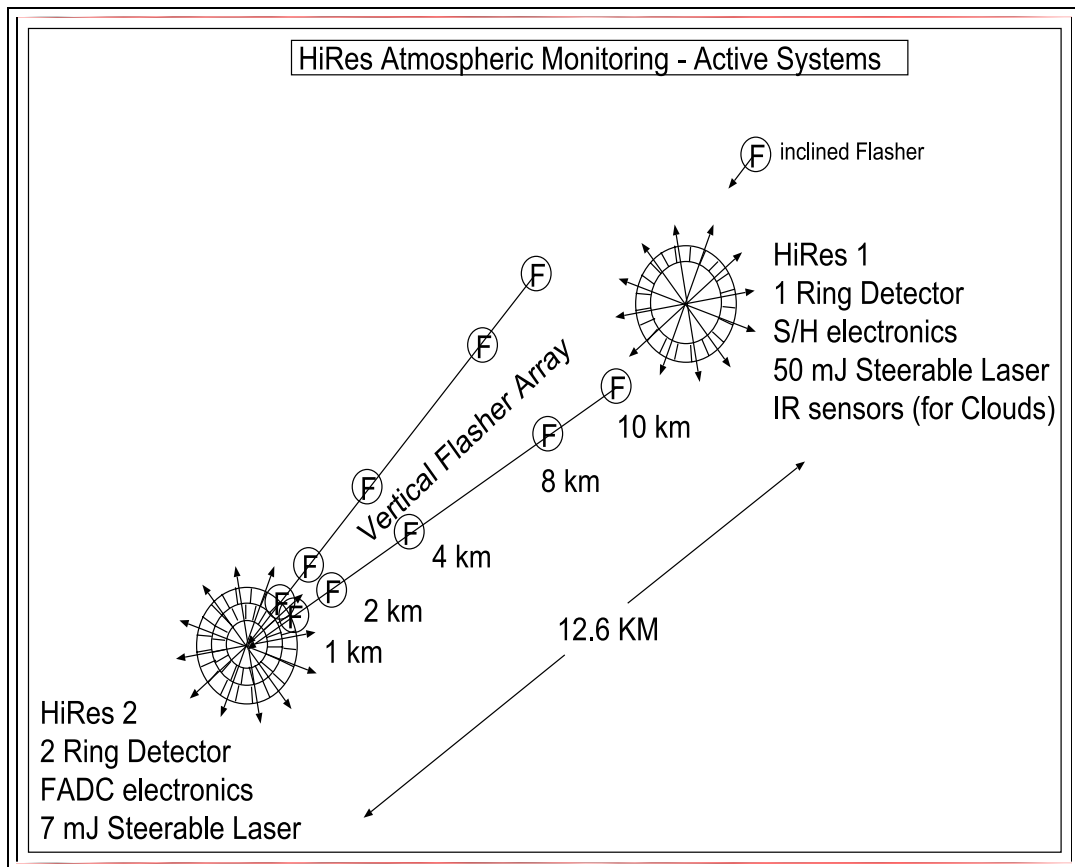


Figure 4.6. A vertical flashers map [57]

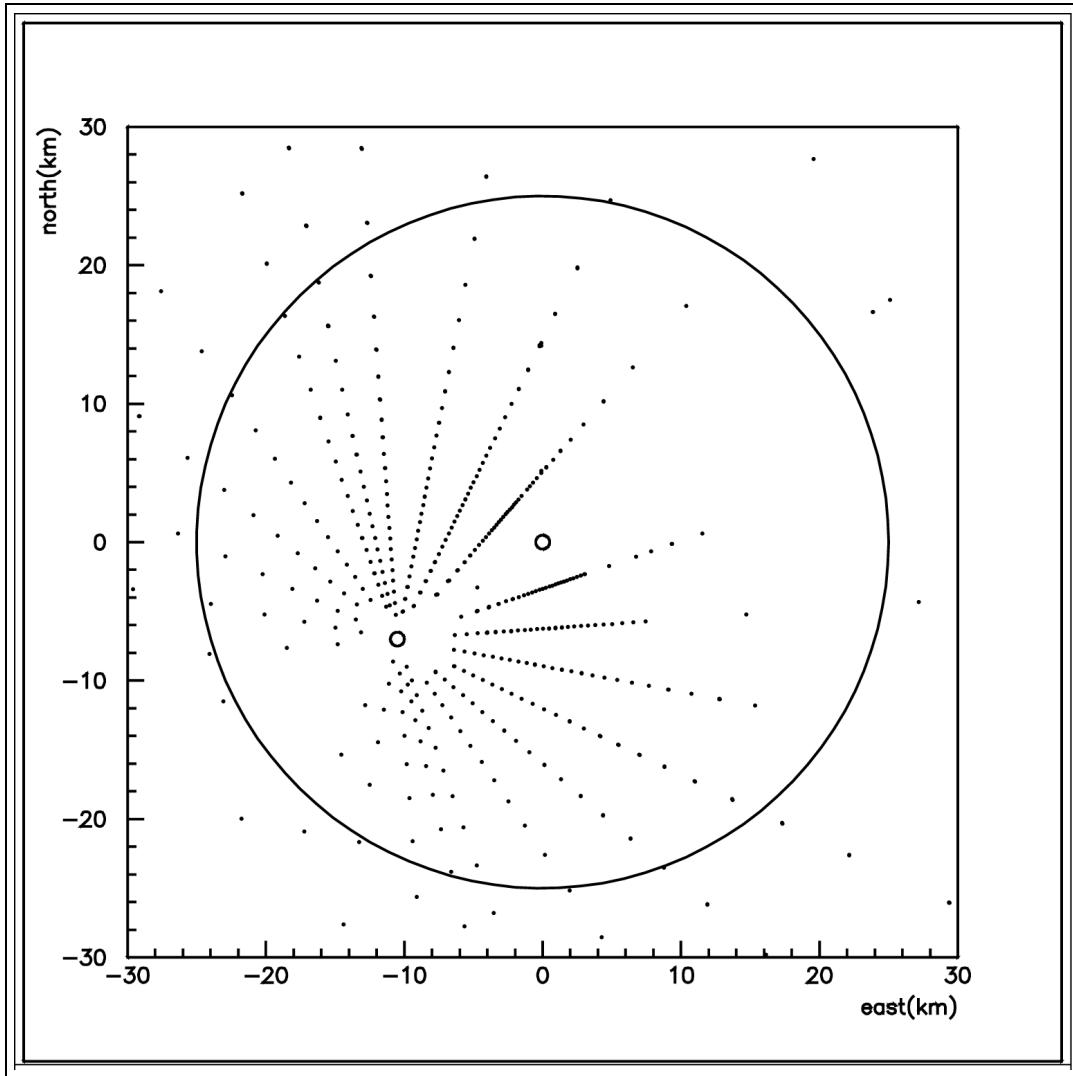


Figure 4.7. Steerable laser shots from HiRes-2 as seen from HiRes-1 [57].

In addition, when a high energy particle is observed by the detector a laser is pointed at the shower, this measurement is described by shoot-the-shower measurement. Such measurement uses many laser shots toward the shower detector plane. The light attenuated from these shots is detected by the other detector and a detailed timely atmospheric information is collected about the important events [60].

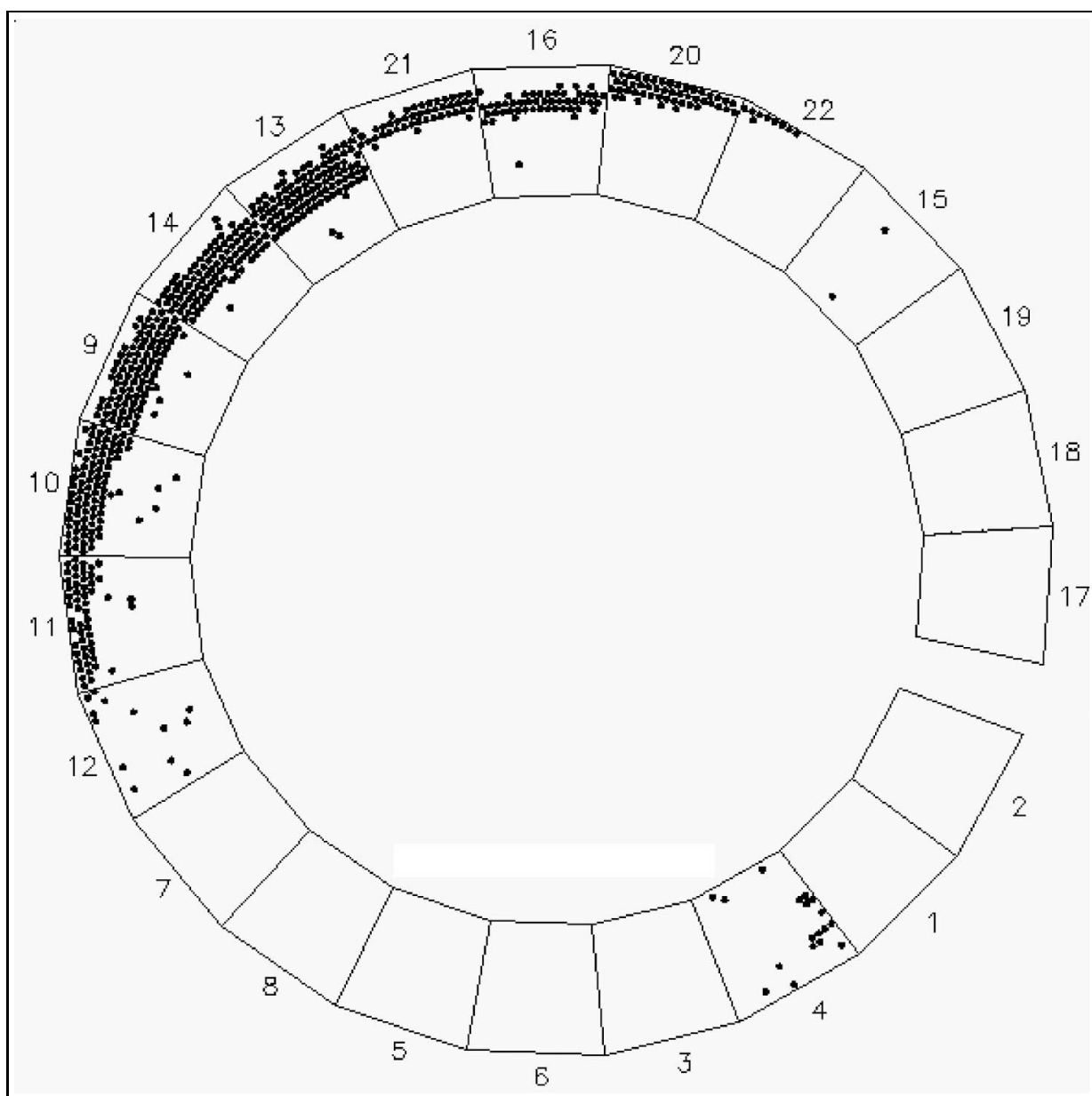


Figure 4.8. A nearly horizontal laser shot as seen by HiRes-1.

CHAPTER 5

EVENT RECONSTRUCTION AND SELECTION

The Anisotropy studies presented in this distribution are based on HiRes stereo data collected between December 1999 and January 2004. The total observation time of 2052 hours. This total observation time is the total number of coincident trigger between the two detectors. This is the same stereo data set that was used in the recent HiRes publication on BL-Lac correlations.

5.1 Reconstruction

In order to determine the energy, and arrived direction of the observed stereo events, the calibrated EAS data must next be presented through reconstruction. This process is divided into two steps: (a) the track geometry reconstruction and (b) the profile reconstruction. Next, cuts are applied to those events which are successfully reconstructed with the goal of optimizing the energy and angular resolutions while retaining the largest possible detector acceptance. These steps are described in more detail in the subsequent sections of this chapter.

5.1.1 Noise Event Filtering

More than 90% of the data collected by the HiRes detectors consist of noise events from random fluctuations in the background light, and from calibration light sources (bi-static lidars and xenon flashers) used to monitor the atmosphere and to extract the aerosol density.

First, the steerable laser events are removed using GPS time samples and the well-defined geometries. Likewise, the xenon flasher events are also cut using geometrical information.

The remaining noise events are subjected to a Rayleigh Filter, which looks for correlated spatial and temporal structure expected in actual cosmic ray showers. The algorithm consists of time-ordering adjacent pairs of triggered photo tubes. A unit vector is constructed from the tube with the earlier trigger time to the later one. The resultant sum, \vec{R} of these unit vectors is then compared to the expectations of a random walk process (assume to be representative of noise events), where

$$P(r > R) = e^{-R^2/n} \quad (5.1)$$

where n is the number of pairs, $R = |\vec{R}|$ is the magnitude of the resultant vector \vec{R} from the observed pairs, and $P(r > R)$ is the probability that a random collection of n pairs would yield a displacement r greater than that observed in the event (R).

The events in question that have a random-walk probability of less than 1% are kept. Also, the direction of the vector \vec{R} also gives a preliminary determination of the direction of the event (downward, sideways or upward). Events that are not downward going are also removed. Figure 5.1 gives an illustration of the Rayleigh filter fit part of a cosmic-ray shower. The eight triggered tubes are labeled in time-order. The individual unit vectors contributing to the sum \vec{R} are shown.

5.1.2 Shower Trajectory Reconstruction

The first step in the trajectory reconstruction procedure is the determination of the Shower Detector (SD) plane (see Figure 5.2). The SD plane can be formed from the direction of the triggered pixels, where the plane is taken to contain the detector, treated as a point, and the shower track treated as a line. The plane normal vector is determined by a χ^2 fit weighted, least-square fit:

$$\chi^2 = \sum_{i=1}^N \frac{(\hat{n} \cdot \hat{n}_i)^2 S_i}{\sigma_i^2} \quad (5.2)$$

Where \hat{n} is the unit vector normal to the plane, \hat{n}_i is the unit vector on the direction of the i^{th} triggered photo tube, S_i is the number of photoelectrons triggering the i^{th} photo tube, and σ_i is the angular uncertainty for the pixel which is taken to be 1° , which is the angular extent of each pixel.

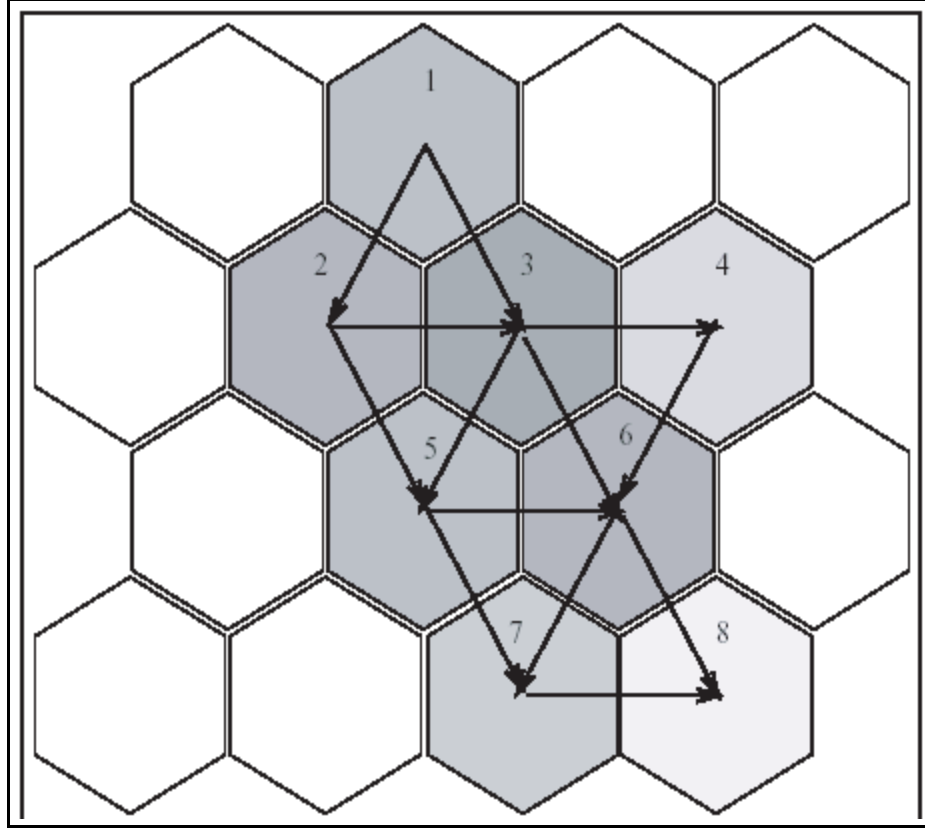


Figure 5.1. Schematic of the Rayleigh scattering [57].

One shower-detector plane is obtained from the hit patterns of each of the two detectors. For stereo events, the trajectory of the shower core is then obtained from the intersection of the two SD planes, as in Figure 5.3.

This procedure gives both the direction of the original cosmic ray and its location in space. This is needed for the subsequent steps in the shower reconstruction.

5.1.3 Shower Profile Reconstruction

Using the known location of the shower, we convert the number of detected photons to the number of photons emitted per unit length by the shower. These numbers are calculated as a function of the slant penetration depth, X .

This profile calculation uses the fact that the fluorescent light is proportional to the number of charged particles in the shower. However, the signal photons observed are a mixture of fluorescent light, Rayleigh scattered, aerosols scattered

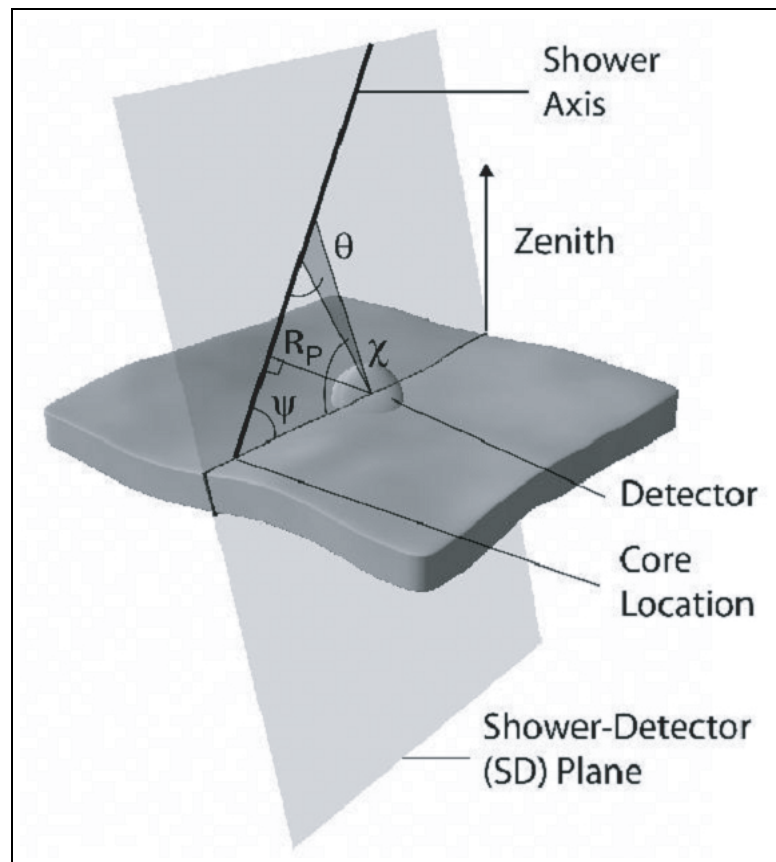


Figure 5.2. The SD plane is formed from the direction of the triggered pixels, where we take the plane to contain the detector, treated as a point, and the shower's track treated as a line.

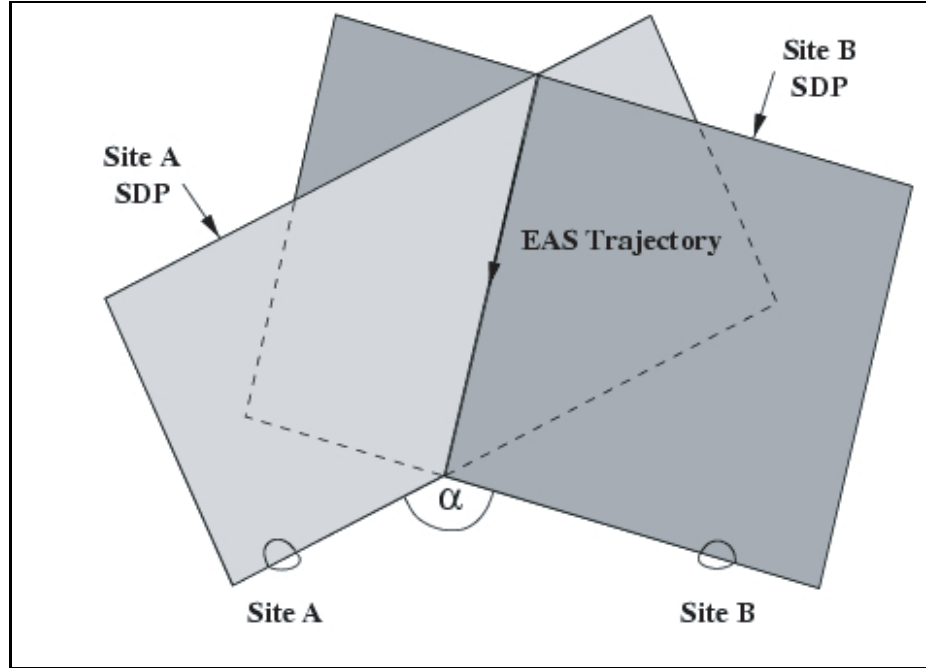


Figure 5.3. Stereo trajectory reconstruction where the trajectory of the shower core is obtained from the intersection of the two SD planes.

and direct čerenkov light (as mentioned in Chapter 3). Therefore, in order calculate the shower profile we need to account for all these components.

The procedure used to extract the shower profile employs an “inverse Monte Carlo” technique where the reconstruction program iteratively produces a shower using the Gaisser Gillas (G-H) parameterization:

$$N(X) = N_{max} \left(\frac{X - X_o}{X_{max} - X_o} \right)^{(X_{max} - X)/\lambda} \exp\left(\frac{X_{max} - X}{\lambda} \right) \quad (5.3)$$

Note that the G-H function has four parameters (X_o , X_{max} , λ and N_{max}). The parameters X_o and λ are fixed. 40 gm and 70 gm/cm^2 , respectively. Subsequently N_{max} and X_{max} are iterated. For each iteration we calculate a prediction for the light produced by the shower including all the contribution listed above. This conversion also takes into account atmospheric attenuation, both by molecular(Rayleigh) scattering and aerosol scattering. The light profile is the converted to the number of charged particles in the shower at varying depths and taking into contribution the atmospheric conditions. The predicted amount of light is then

propagated back to the detectors, correction for the attenuation due to aerosols and Rayleigh scattering to give a predicted signal.

Through the iteration we search for the best fit N_{max} and X_{max} values by minimizing the χ^2 function. The iteration continues until chi squared function is minimized where the χ^2 is:

$$\chi_{pfl}^2 = \sum_i \frac{1}{\sigma_i^2} (\phi_i - \phi_i^{(mc)})^2. \quad (5.4)$$

Here ϕ_i is the flux measured at the detector for each 1° bin in units of the number of photoelectrons per degree per m^2 , $\phi_i^{(mc)}$ is the flux predicted by the fit, and σ_i^2 is the uncertainty calculated after adding the poisson fluctuation and the noise background light.

χ_{pfl}^2 is minimized individually for HiRes-1 and HiRes-2. It is also minimized for both detectors by adding the minimized χ_{pfl}^2 from each site. Subsequently the values of N_{max} and X_{max} found are the values that would define the shower profile. The energy of the shower is then calculated by integrating the number of charged particles along the shower track [45]. Figure 5.4 shows an observed shower profile for an event as seen by HiRes-1 and HiRes-2.

5.1.4 Analyzed Data Set

After successful reconstruction, the remaining events are subjected to additional selection cuts in order to optimize energy and angular resolution. Even though this data set is being used for the pointing direction of the events, energy resolution is still a relevant consideration because a lower-bound cut of 10^{19} eV is made on the energy. Below this energy the direction of the events are likely to be scrambled by magnetic deflection to give any meaningful coincidence signals. The selection cuts are summarized in the list below:

- $\chi^2/ndof$: events with a $\chi^2/ndof$ in the geometrical fit greater than 5 are rejected.
- $\chi^2/ndof$: events with a $\chi^2/ndof$ in the profile fit greater than 5 are rejected.

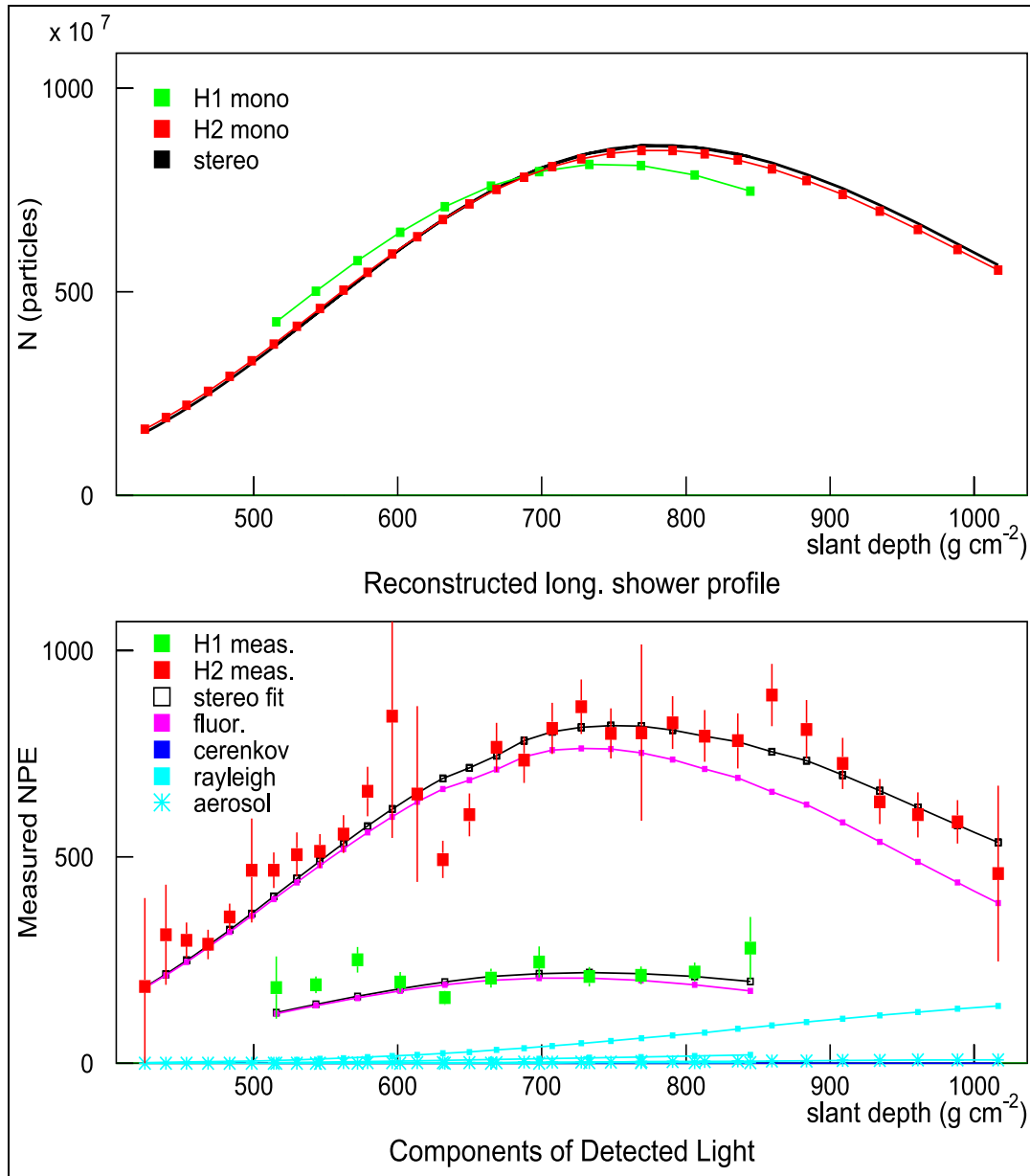


Figure 5.4. The upper figure shows the shower profile, the number of particles in the shower vs. the atmospheric depth as reconstructed by HiRes-1, HiRes-2 separately and together in stereo mode. The lower figure shows the number of photoelectrons per degree per m^2 vs. atmospheric depth for the shower as seen by HiRes-1 and HiRes-2. It also shows the best stereo fit measured. Additionally, this figure shows the individual contribution of different light components (fluorescent, čerenkov, Raleigh and aerosol scattering) towards the total detected signal. Note that this event has a reconstructed energy of 13 EeV. It was detected 25 km from HiRes-1 and 15 km from HiRes-2.

- zenith angle(θ_z): events with zenith angle greater than 70° are rejected.
- zenith angle uncertainty (σ_z): events with a σ_z that is larger than 2° are rejected.
- azimuthal angle uncertainty (σ_a): events with $\sigma_a \cdot \sin\theta_z$ greater than 2° are rejected.
- energy uncertainty: events with energy uncertainty σ_E/E greater than 20% are rejected.

After these cuts there are 4495 events from the stereo data set; 271 of them have energy 10^{19}eV . Figure 5.5 shows these 271 events in equatorial coordinates projected in Hammer-Aitoff projection.

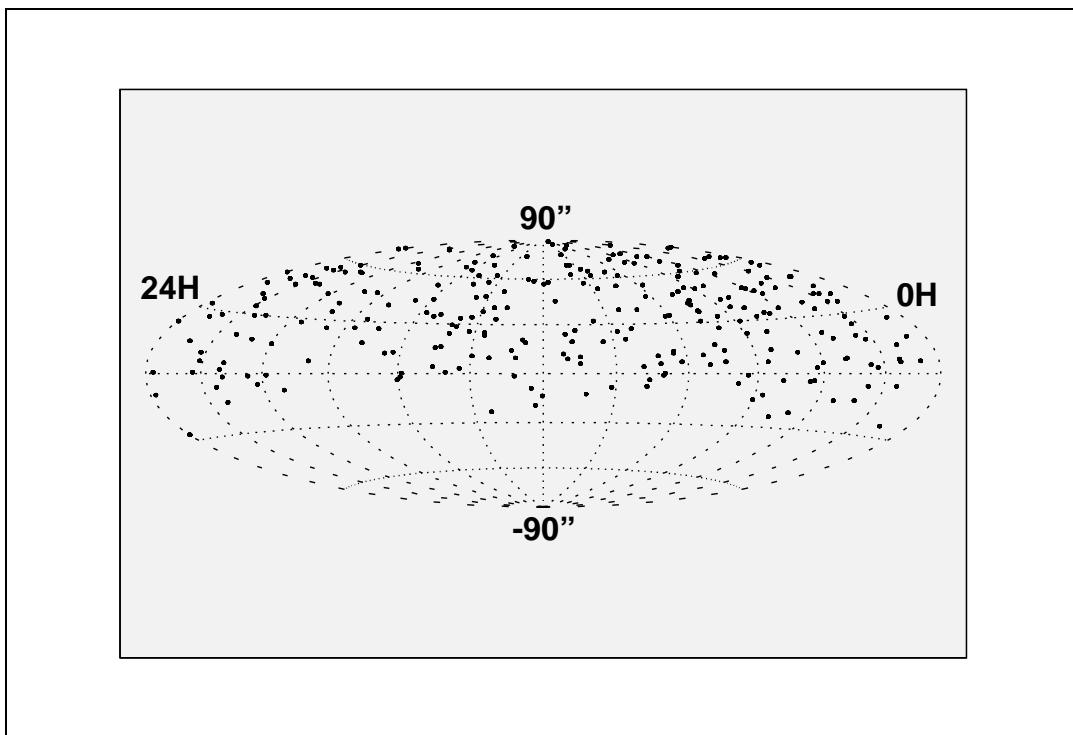


Figure 5.5. The 271 event stereo data set in Hammer-Aitoff projection.

CHAPTER 6

SEARCH FOR EXTENDED CORRELATIONS

While the search for small-scale anisotropy in UHECR datasets have concentrated on point-like sources, the existence of the galactic and extra-galactic magnetic fields (GMF and EGMF) suggests the same deflections are expected for charged particles. The actual deflections depend on the strength and coherence of the field, where widely divergent oriental predictions have been made. In some scenarios, it is possible for cosmic rays arriving from point source to align in arcs (see for example the plot from Gustavo-Medina Tanco, Figure 6.1).

In addition to the magnetic deflection of point sources, there exists the possibility of extended source such as the galactic and super-galactic planes. In this section we describe a search for arc-like enhancements of events along a great circle in the sky. For this study, we adapt a spherical version of the Hough Transformation, and then apply the technique to the HiRes stereo data.

6.1 Introduction to Hough Transformation

The Hough transform is a class of duality transformations commonly used to identify 1-d structures in graphical images [64] (e.g., edges and lines). In this study, we are applying a version of the Hough Transformation to look for arcs in the arrival direction of HiRes events. Here we use the term “arc” to describe segments of great circles in the dome of the sky.

The Hough Transform is a duality transformation. In our case, where it is applied on a sphere, the transformation is actually self-dual. The pointing direction of each event is mapped to a great circle that is perpendicular to it. For events

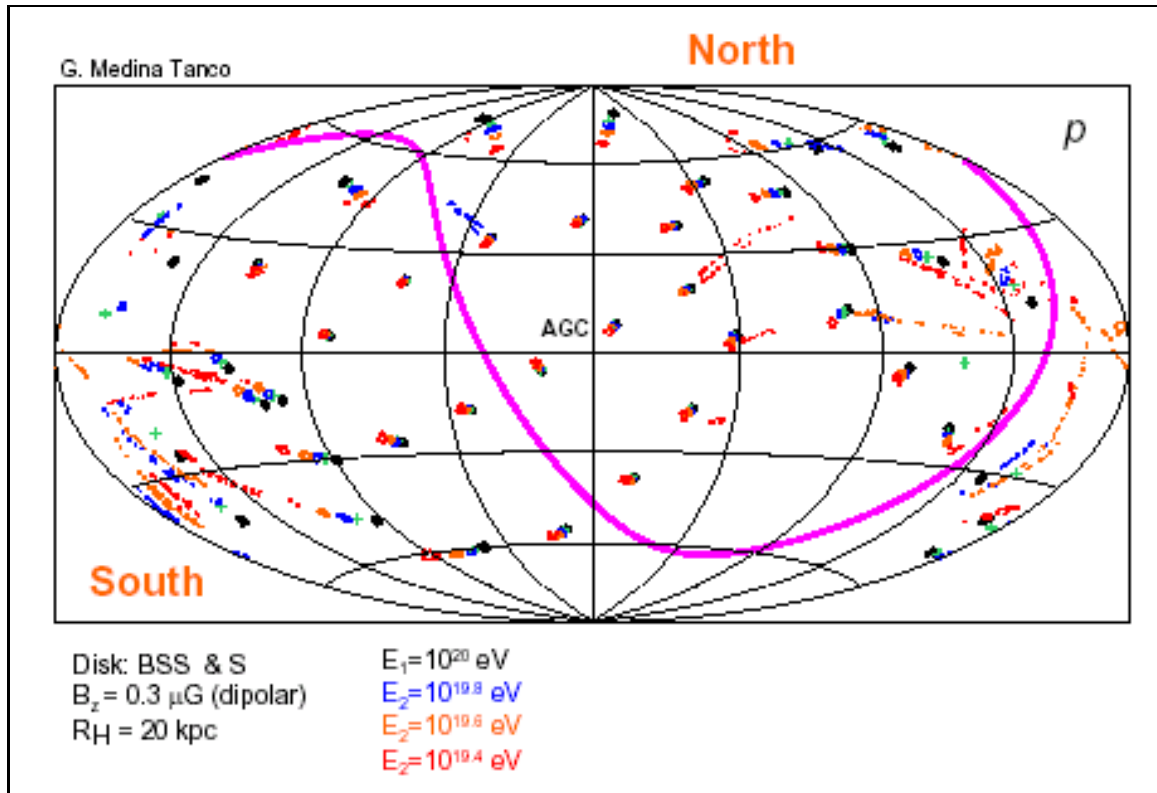


Figure 6.1. Simulated polarization plot by Gustavo Medina-Tanco [65] showing cosmic rays with energies between $10^{19.4}$ and 10^{20} eV. The events are deflected while passing through the galactic magnetic field forming arcs shapes. While the events originate at point sources, the magnetic field deflects the events to form the arc shapes which one sees in the plot.

that lie on an arc, their associated great circles would intersect at two points, as illustrated in Figure 6.2.

To find such multiple intersective in the dual space, we then divide the sky into equal sized and shaped bins. A coarsely binned example (for illustration purposes only) is shown in Figure 6.3. The analysis procedure consists of looping over all events. For each event, we increment those bins through which the corresponding dual great circles passes. The bin values therefore represent the total number of dual great circles that lie within its boundaries. The arcs are then identified by significant excess in a particular bin. in dual space.

For our analysis, the sky is then binned into 6° , equal area bins (a total of 4584 bins). This bin size was chosen to given reasonable bin statistics for the HiRes dataset, without iterative optimization. Each bin is then arbitrarily numbered in latitude from north pole to south and around the axis. Finally, the bins values are plotted and an excess is found in the two bins were the great circles meet.

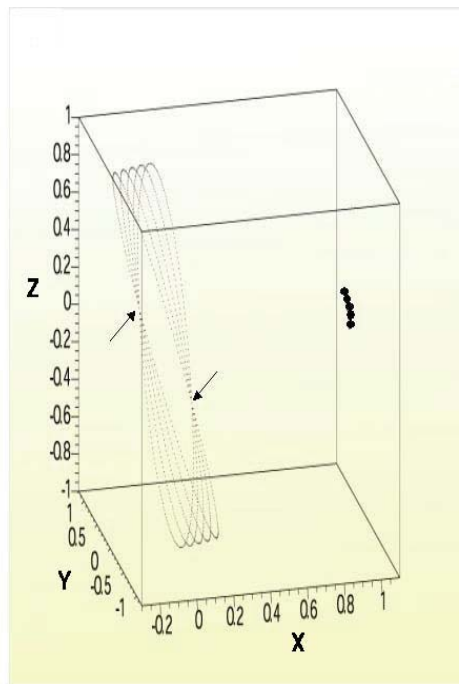


Figure 6.2. Illustration of the Hough transform applied to fire events that lie on an arc. Their dual great-circles intersect at two locations indicated by the arrows in the figure.

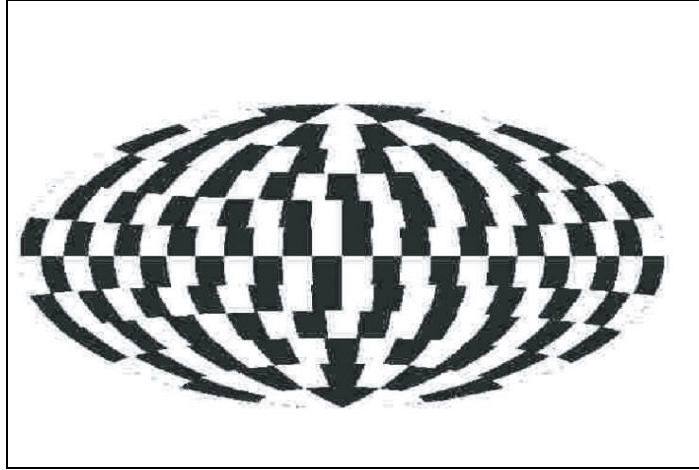


Figure 6.3. An illustration of the latitudinal binning scheme where the sky divided into equal-sized and equal-shaped bins. This example uses a coarse, 1° bins. In the actual analysis, 6° bins are used [66].

6.2 Applying The Hough Transform

We apply the Hough transform method to the stereo HiRes data to search for arcs of events in the data. The HiRes stereo data have excellent angular resolution of $\sim 6^\circ$. The data selected are those events with energies $> 10^{19}$ eV (particles with energies $< 10^{19}$ eV are deflected by larger angles). This data set contains 271 events collected between December 1999 and 31 January 2004. More details about this data set are given in [67].

Figure 6.4 shows the particle's arrival direction (in equatorial coordinates) for the 271 events used in this analysis. The same data are also shown in Hammer-Aitoff projection in Figure 6.5. After applying the Hough Transform to the data set, the bin occupancy for the great circles is calculated. The resulting histogram is shown in Figure 6.6.

6.3 Background Estimation

The signal for arc-like coincidence in this study is an observed excess in the dual-space bin content relative to what is expected from an isotropic background distribution. An essential part of this analysis is therefore the simulation of such

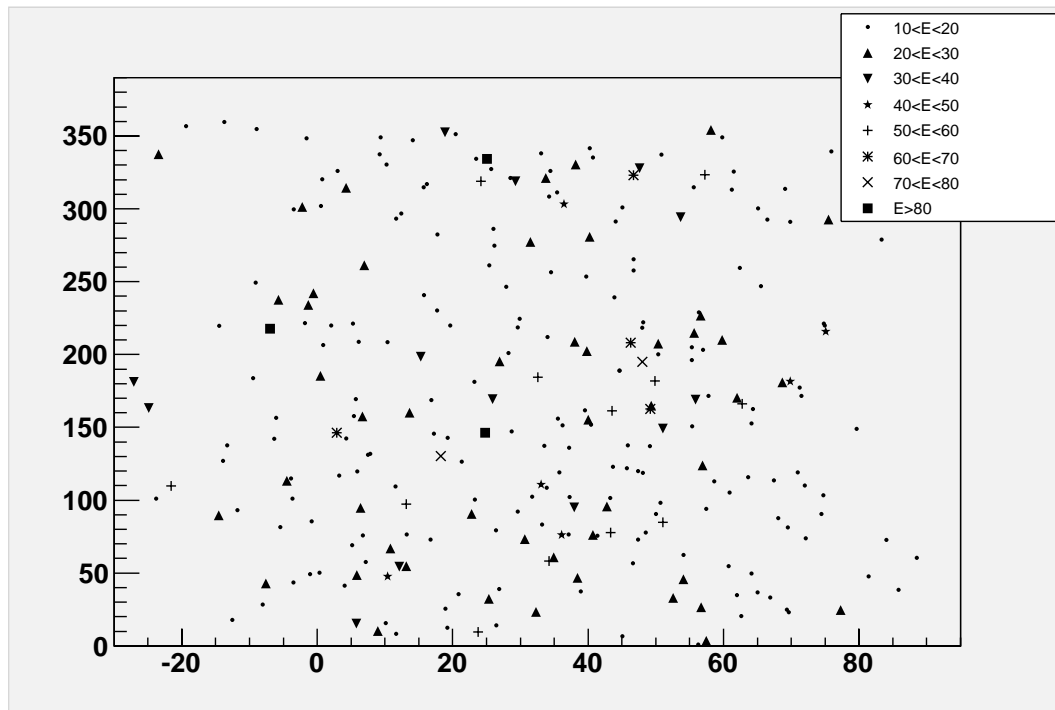


Figure 6.4. The pointing direction, right ascension vs. declination in degrees, of the 271 events used in this analysis. The box on the top right of the figure shows the color key for the energies (in EeV) of the events.

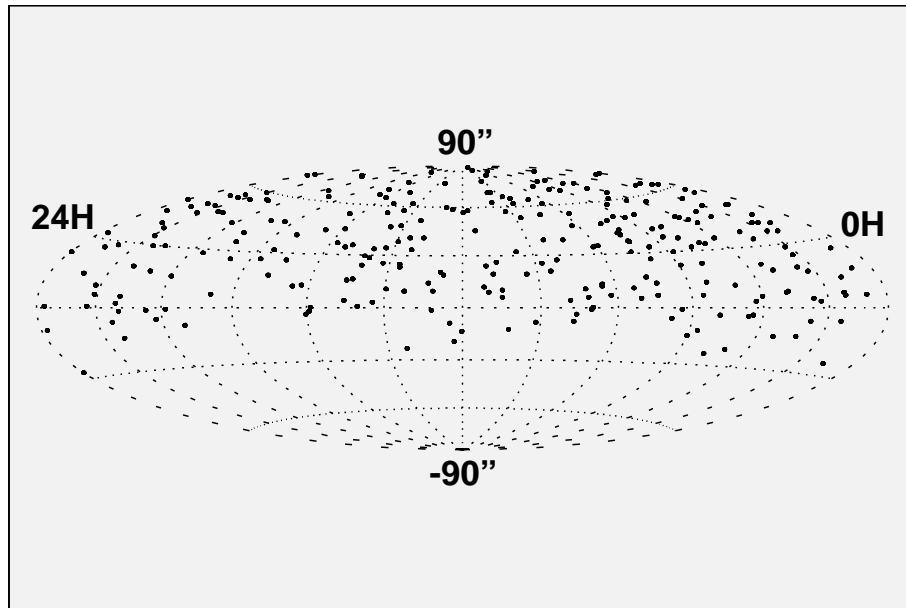


Figure 6.5. The 271 event stereo data shown in (equatorial coordinates) Hammer-Aitoff projection.

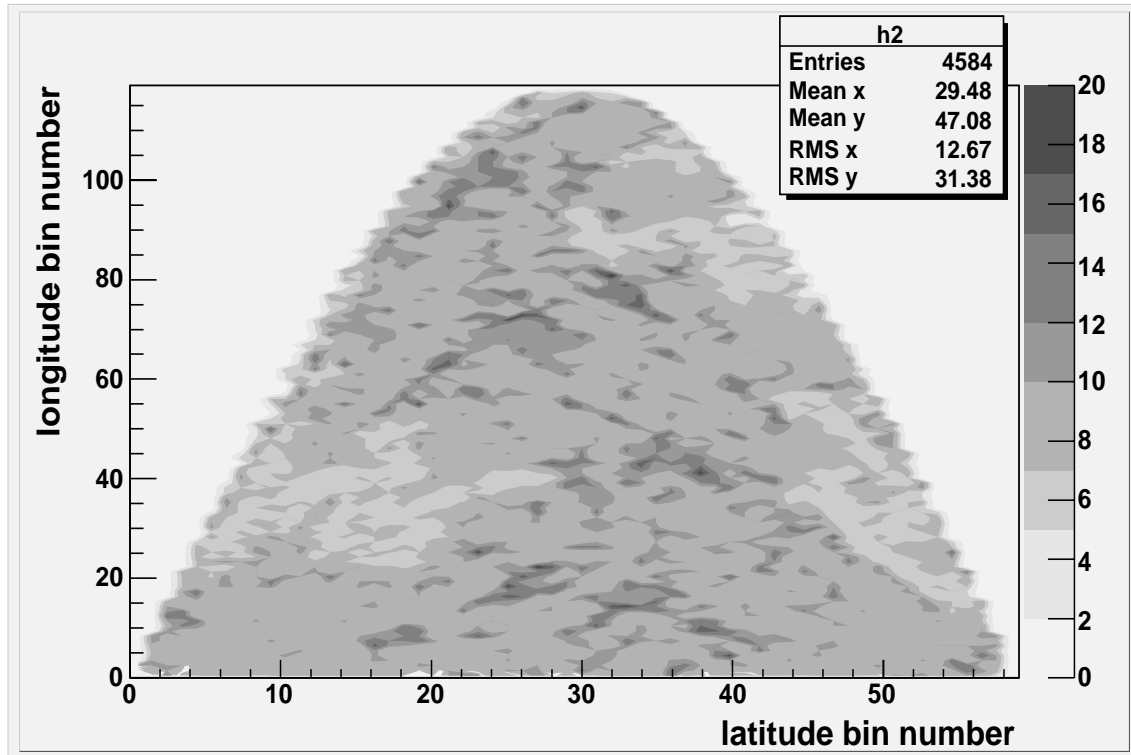


Figure 6.6. The bin occupancy values of normal great circles to the stereo data set. The sky was divided into 4584 number of bins of equal size (6°) with the north pole at the zenith. The bins are arbitrarily numbered in latitude from north pole to south and around the axis.

background sets, including the random fluctuation associated with limited sampling.

To calculate the chance probability for the arcs found, a comparison to simulated isotropic background data sets is determined. The background is first simulated with an energy flux of the order of $\alpha = -3.0$. Afterwards, the Monte Carlo data are retraced with the detector reconstruction described in Chapter 5. By this step we are able to calculate the detector acceptance of the zenith and azimuthal angle. Subsequently, the timing information is added to get the detector exposure. The result is a sky map that gives the exposure of the detector in different directions of the sky.

Note that to simulate a smooth sky map events with all energies are used. In addition, it is assumed that the right ascension acceptance of the detector is isotropic. In addition, note that using the sky map to simulate the events arrival direction from the calculated exposure helps us gain speed as opposed to using the detector simulation. Figure 6.7 compares the distribution of the observed data in points with error bars as oppose to the simulated data in solid lines in the right ascension and declination. For right ascension, $\chi^2/ndof = 0.77$; as for declination $\chi^2/ndof = 0.73$ [45].

6.4 Search for Significant Excess

In order to identify the statistically significant arcs, we look for apparent excess over what is expected from the simulated isotropic background. To estimate the significance of such excess in each bin, we compared the data distribution to that of 2×10^4 isotropic simulated data sets. Each simulated data set contained 271 events generated randomly according to the actual HiRes stereo exposure, and assuming an isotropic *a priori* distribution.

From the Monte Carlo data sets, we calculate the probability for each dual-space bin to have a simulated occupancy greater than or equal to that found in the data. We define the significance, S , for a bin to be given by

$$S = \log\left(\frac{1}{P}\right) \quad (6.1)$$

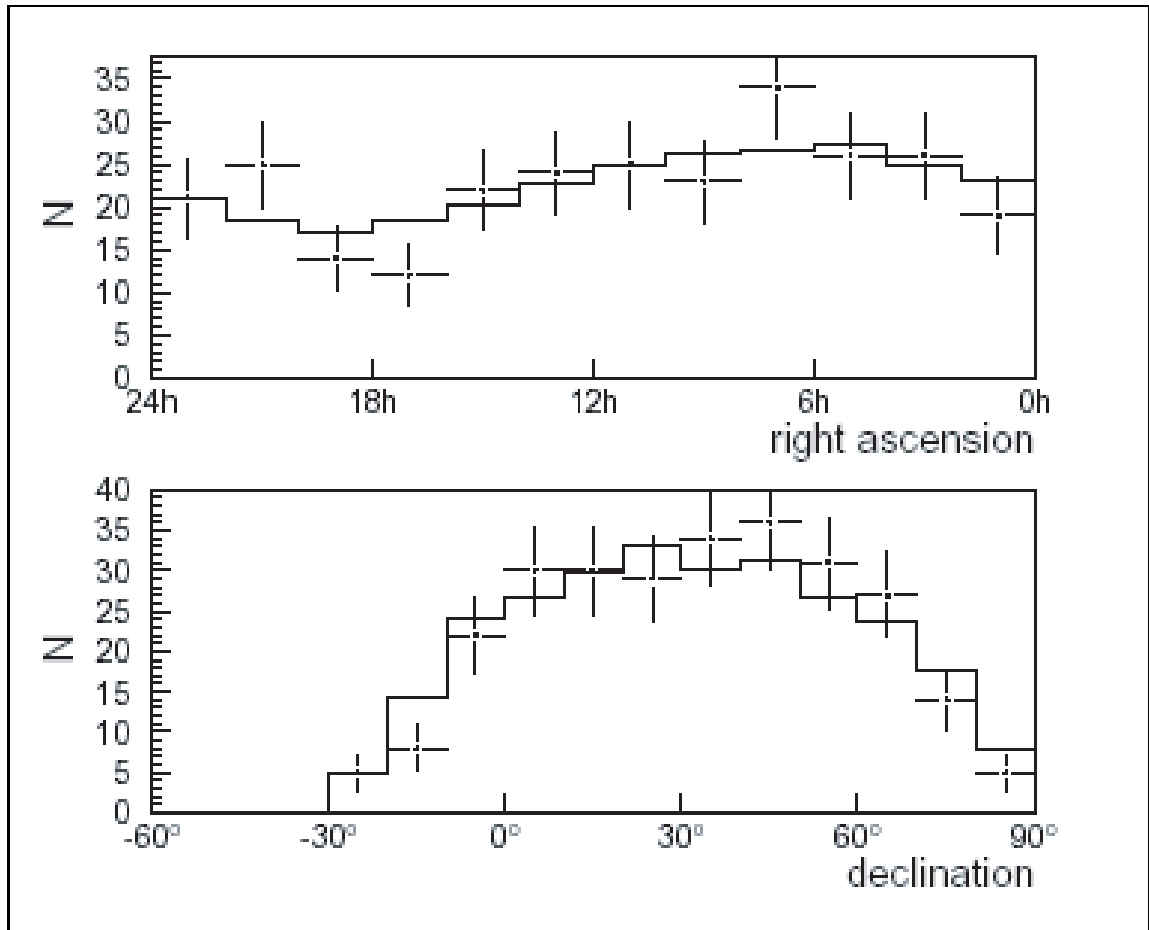


Figure 6.7. Right ascension and declination histograms. The observed data are the points with the errors bars. The simulated data are in the solid lines [45].

and

$$P = \frac{M}{N} \quad (6.2)$$

where N is the total number of simulated data sets, and M is the number of MC sets which recorded an occupancy greater or equal to that seen in the data bin.

The resulting significance values are shown in Figure 6.8, where each bin is indexed by both a longitudinal (RA) and a latitudinal (DEC) bin number. We designed bins with $S > 2.5$ designated as “high significance.” This cut was chosen *a priori*. In addition to the significance and energy ($E \geq 10^{19}$ eV) selection, we also required the opening angle between any pair of events in an arc to be less than 5° . This requirement was added to reduce the background from long-range random overlaps.

The HiRes stereo data showed seven “high significance” bins. The arcs corresponding to these bins are shown in Figure 6.9. The arc with the greatest significance had a value of $S=3.5$.

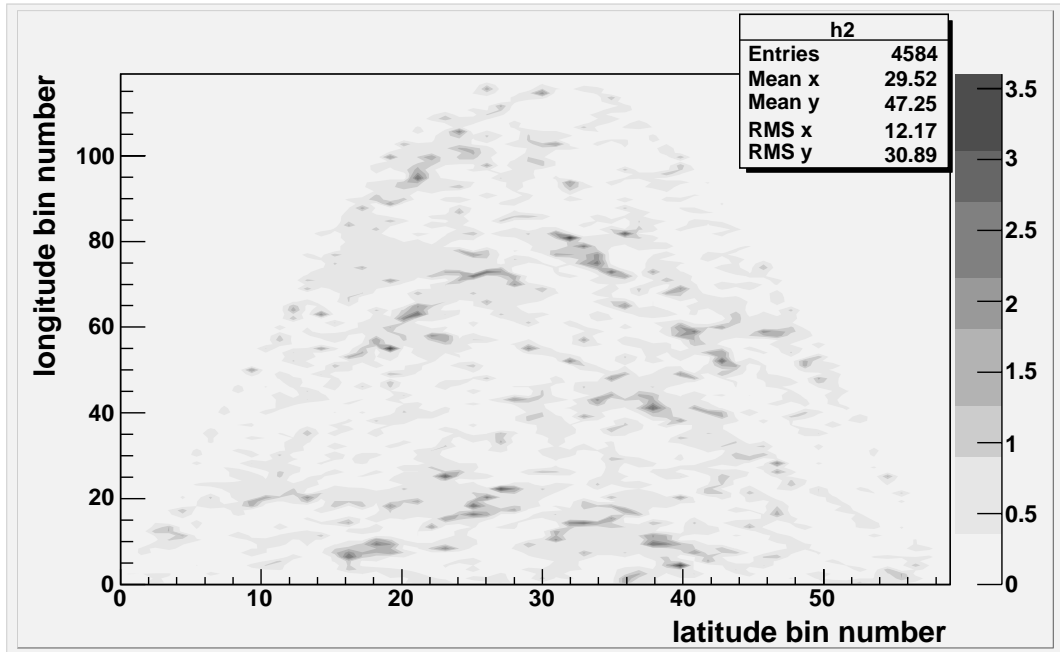


Figure 6.8. Significance values for each bin.

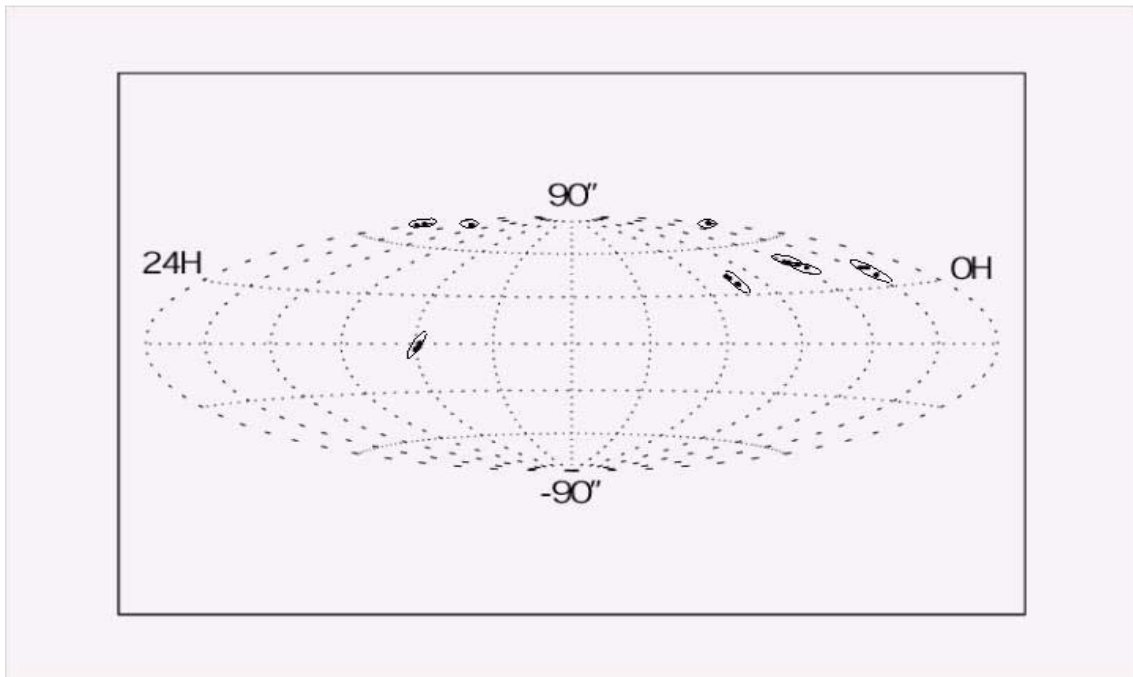


Figure 6.9. The arcs found in the stereo data set (the actual arrival direction) in Hammer-Aitoff projection (for clarity each arc has been enclosed with an ellipse).

For the seven high-significance bins we display in Figure 6.10 the occupancy histogram of that bin for the 2×10^4 isotropic MC set. A vertical line is drawn on each plot at the bin occupancy level found in the data. The probability of randomly finding at least this occupancy level in an isotropic data set is then the ratio of the area under curve to the right of the line to the whole area (2×10^4). The significance value S , as defined earlier, then calculated and recorded in the boxed number for each bin.

6.5 Global Significance of Data Excess

While we did find seven arcs with claim probabilities of $< 3 \times 10^{-3}$ in their respective bins, a full interpolation of the data requires a global significance study to determine whether this number of arcs is consistent with fluctuation over the full sky, not just in the location in which they occurred. To this end, we compare our 2×10^4 isotropic simulated sets to a new set of 1000 isotropically simulated data sets, each with 271 events. These new MC sets were analyzed in exactly the same manner as the actual data set, following the procedure described earlier in this chapter. We also applied the significance cut of 2.5. From these 1000 sets, we found that 99.6% of the time, the maximum significance of the isotropically generated data sets is greater than 2.5. Also, in 41.2% of the samples, the simulated data sets recorded a significance ≥ 3.5 , which is the highest significance found in the real data set.

Finally, the greatest number of events found on an arc in the real data is 19, as shown in Figure 6.10. This was also seen to be quite common in the simulation, where arcs with $S > 2.5$ and at least 19 events were found in 90.4% of the simulated isotropic sets.

6.6 Conclusion

The Hough transform has been applied to the HiRes stereo data and seven arcs were found. However, when a global significance analysis was performed, similar results were commonly reproduced within isotropic data sets of equivalent size. Hence, the observation of seven arcs in the data is not significant.

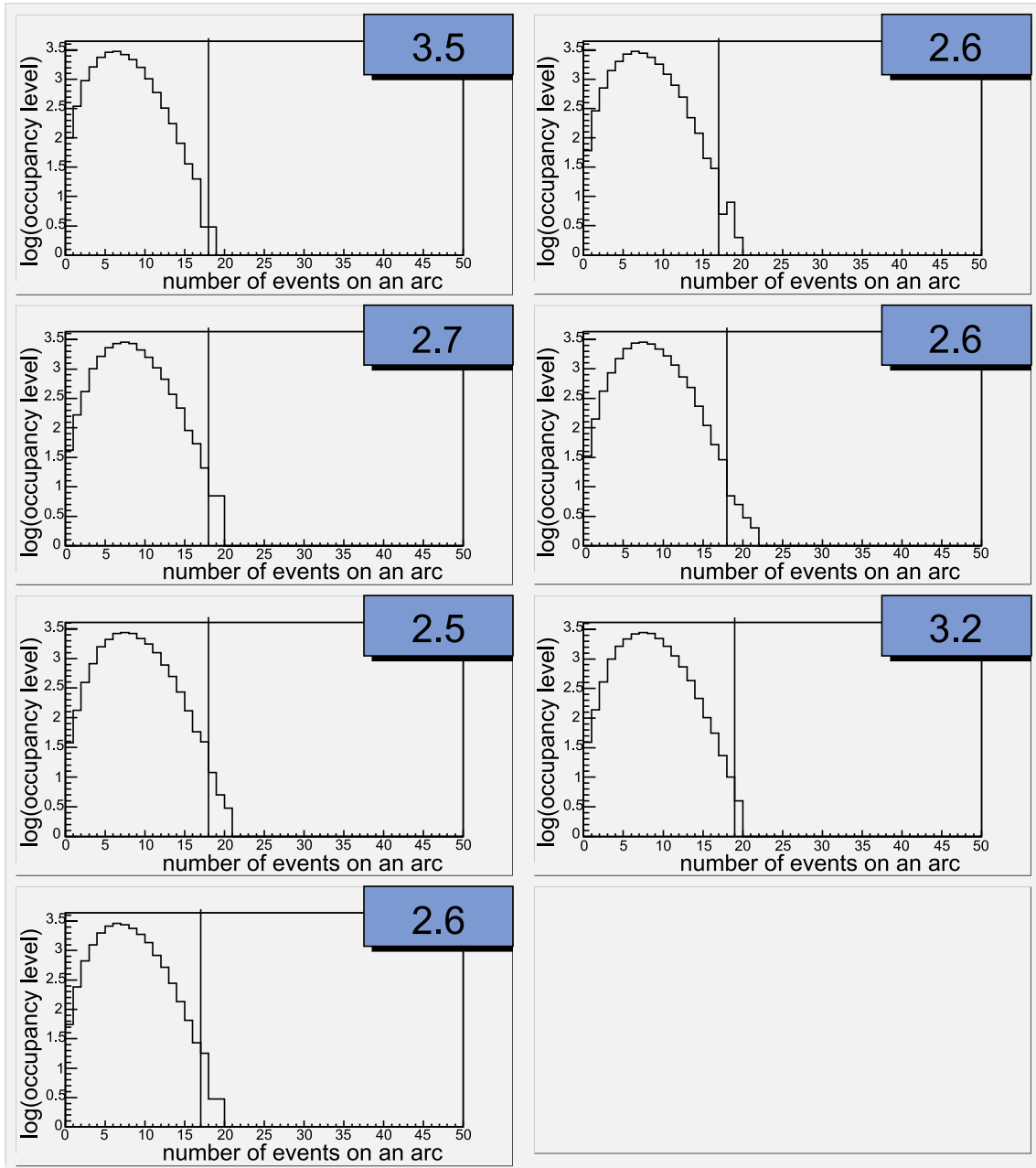


Figure 6.10. For the 2×10^4 isotropic MC sets, we histogrammed the occupancy level for the bins which showed “high significance” in the data. The histograms above show the logarithm of the occupancy level vs. the number of events in the arc. A vertical line is drawn on each plot at the number of events in the arcs found in the data. The probability of randomly finding at least this many events in an isotropic data set is then the ratio of the area of the curve to the right of the line to the whole area (2×10^4). The significance value is then calculated and recorded in the boxed number for each bin.

CHAPTER 7

CROSS CORRELATION WITH BL LACERTAE OBJECTS

After many decades of cosmic ray research the origin of UHECRs is still unknown. A leading candidate for the source of UHECRs is the BL-Lacertae class of objects. This suggestion is supported by recent studies that show significant correlations between AGASA and Yakutsk cosmic rays data set and a subset of BL-Lacertae objects([69], [70], [71]). In this chapter a cross correlation study between the arcs found in HiRes stereo data and the BL Lacertae objects is presented.

7.1 BL Lacertae Objects

BL Lacertae objects or BL Lacs are a type of Active Galactic Nucleus (AGN). An AGN is suspected to contain a super-massive black hole in its center and an accretion disk around it. The material in the accretion disk contains gas and dust; it tumbles around the black hole and in the case of AGNs produces twin luminous jets along the spin axis of the AGN. BL Lacs, also known as blazars, are characterized by their featureless spectrum (in radio, infrared and optical wavelengths). They are suspected to be a subclass of AGNs with their luminous jets aligned to our line of sight.

Blazars are an established source of TeV Gamma rays [68]. They are also a suspected source of Ultra High Energy Cosmic Rays (UHECRs). Many studies have been made to search for correlations between these objects and cosmic rays events detected by various UHE cosmic ray experiment(([69], [70], [71])). The results of these studies have been mixed, with a number of papers reporting correlation ([69], [71]), although none of these claims has been verified by independent data sets. These results have also been criticized for the *a posteriori* nature of their

analysis cuts([72], [73]). In addition, the apparent correlations which have been reported are consistent with the angular resolution of the respective experiments. This would require the primary cosmic rays to be (exotic) neutral particles. In a more conventional picture, one would expect cosmic rays to be bent by magnetic fields. If the fields are sufficiently coherent then the events should fall into arcs near their sources. Because of these controversial results, we include here a cross correlation study between the arcs found in our data and the BL-Lac objects.

7.1.1 Cross Correlation Study With BL-Lacertae

In an attempt to answer the question of whether BL-Lacs are the source of the UHECRs a correlation analysis between the arcs (obtained when applying Hough Transform to the stereo data set) and the BL Lacs positions has been applied to two sets of BL Lac data. The comparison was first performed for BL Lacs with magnitude < 18 and with classification type BL. This set was defined by (Ref. [70]). We call this the BL set. A second comparison was made after including the (so-called) Highly Polarized (HP) BL Lacs, again requiring a magnitude < 18 . We call this the BL+HP set.

Figure 7.1 shows a histogram for the cosine of the angle between the BL set and the closest event in the arc to the BL set. One might notice what appears to usually be an excess in the last two bins. To study the significance of this excess, a comparison was made with 10^4 Monte Carlo data sets. Each simulated set contained 271 events (same size as real data) isotropically simulated according to HiRes stereo detector exposure. For each MC set, we find the arcs in the set and we calculate and histogram the cosine of the angle between these arcs and each BL object.

The values of the cosine histogram of each of the 10^4 simulated sets shown in Figure 7.2 are then normalized to the area of the real data distribution shown in Figure 7.1. Figure 7.3 shows the distribution of the occupancy level of the simulated sets for the right most bin of the cosine histogram. A vertical line is drawn at the number of pairs found in the real data at that bin. The distribution fitted well to a Gaussian. The probability of finding at least this many pairs in an isotropic data

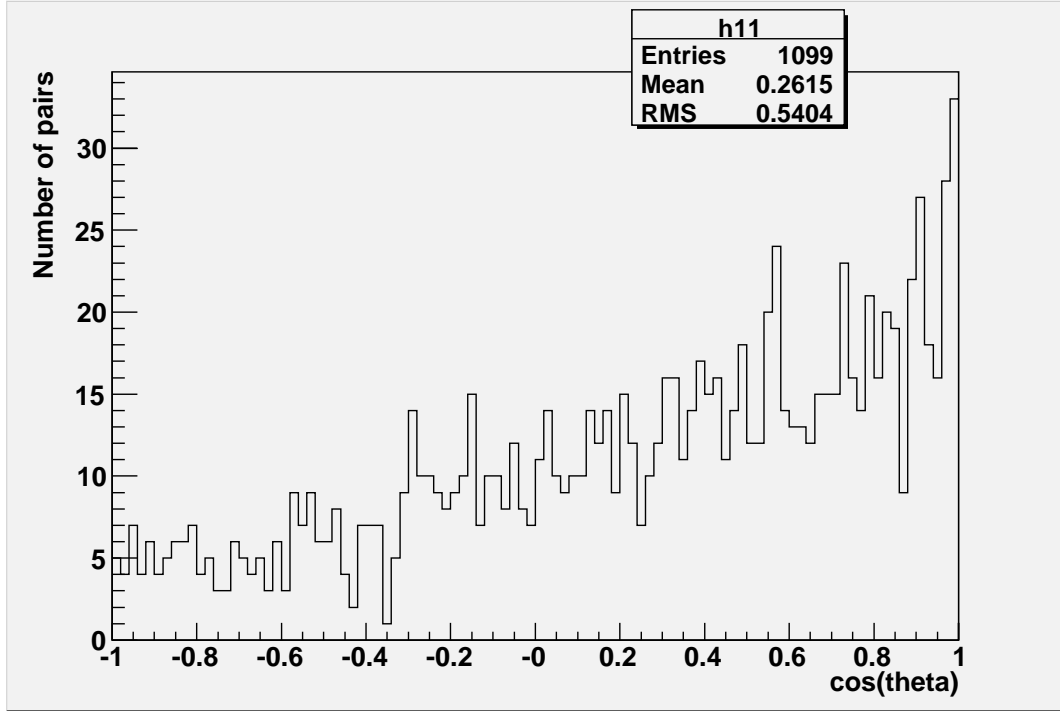


Figure 7.1. Histogram of the cosine of the angle between the BL Lac and the closest event in the arc in the real data set to the objects in the BL set.

set is then calculated by dividing the area of the curve to the right of the vertical line to the whole area of the distribution (a more detailed explanation about the probability calculation is given later in this chapter). In other words,

$$P_{last\ bin} = \frac{\#simulated\ data\ sets \geq\ real\ data\ value}{\#total\ simulated\ data\ sets} \quad (7.1)$$

For the cross correlation seen between the HiRes data and the BL set, we obtain a value of $P=0.174$.

Figure 7.4 shows the histogram for the cosine of the angle between the BL Lacs and the closest event in the arc to the BL Lac for the BL+HP set. The same process applied to the BL set is used here. The probability of the value of the last bin being \geq that of the last bin in Figure 7.4 is then calculated using Equation 7.1 to be 0.318.

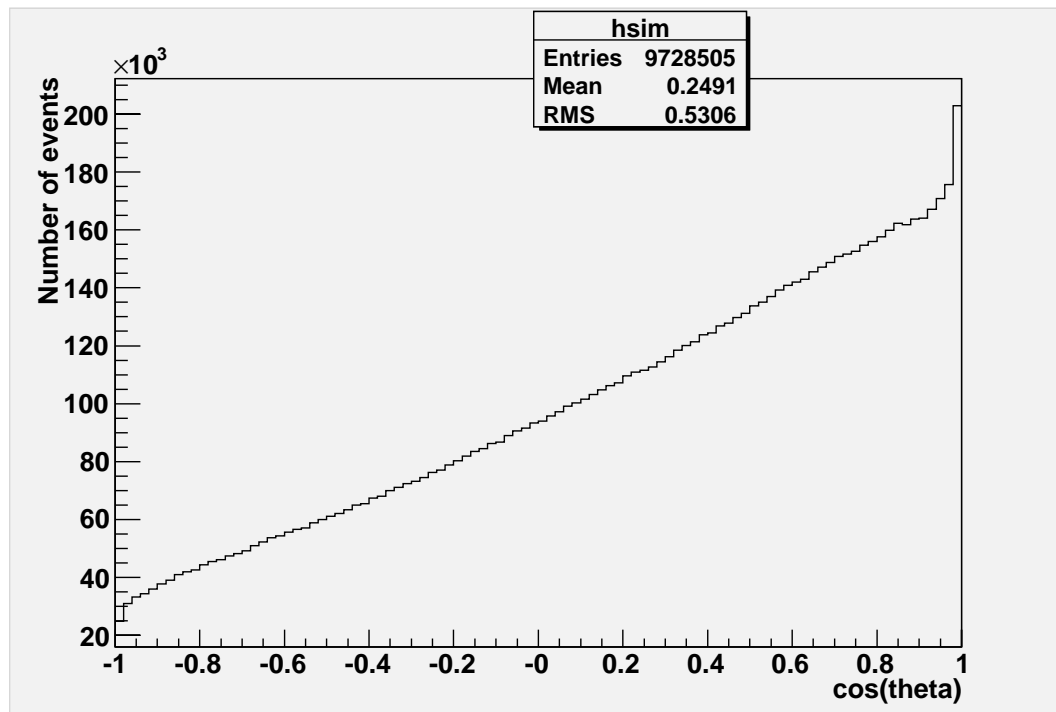


Figure 7.2. Histogram of the cosine of the angle between the BL Lac and the closest event in the arc. The arcs used in this figure are the ones found in the 10^4 simulated sets to the objects in the BL set.

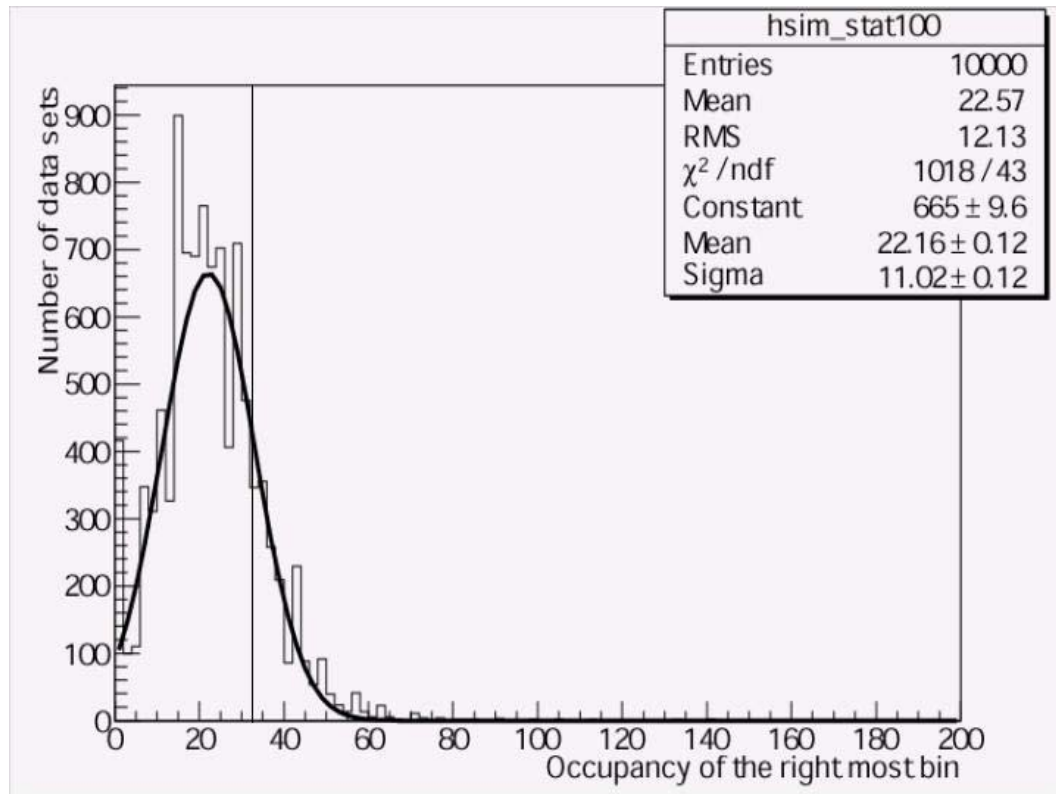


Figure 7.3. This figure shows the distribution of the occupancy level of the 10^4 simulated sets for the right most bin from the cosine theta histogram in Figure 7.1. A vertical line is drawn at the number of pairs found in the real data set at that bin. The probability of finding at least this many pairs in an isotropic data set is then calculated by dividing the area of the curve to the right of the vertical line to the whole area of the distribution.

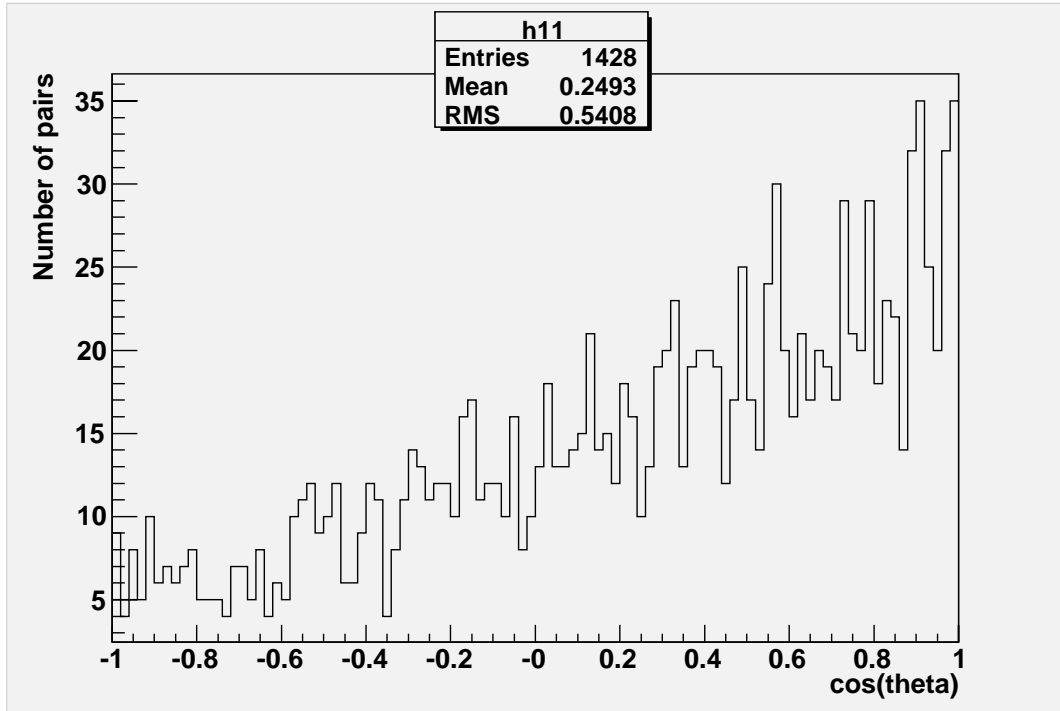


Figure 7.4. Histogram of the cosine of the angle between the closest point in the arc to the BL+HP set.

7.1.2 The Arc Average Point Correlation With BL-Lacertae

In Figure 7.2 we noticed a peak in the last bin near $\cos \theta = 1$. This suggests that the use of the closest event to the BL Lac to calculate the event-BL Lacs pairing produces a bias at small angles.

To circumvent this effect, we repeated the same study except that instead of studying the correlation between the closest point in the arc and the BL Lac source we examined the correlation between the centroid (the average vector of the events on the arc) in the arc and the BL object.

Figure 7.5 shows the histogram of the cosine of the angle between the central point on the arc and the objects in the BL set. We applied same procedure used previously to find the chance probability of the value of the last bin in Figure 7.1, except that we rebinned the cosine histogram into 50 bins. This change was made because the excess in Figure 7.1 was in the last two bins, and because the bin fluctuations are found non-poissonian as the result of the bin-to-bin correlation.

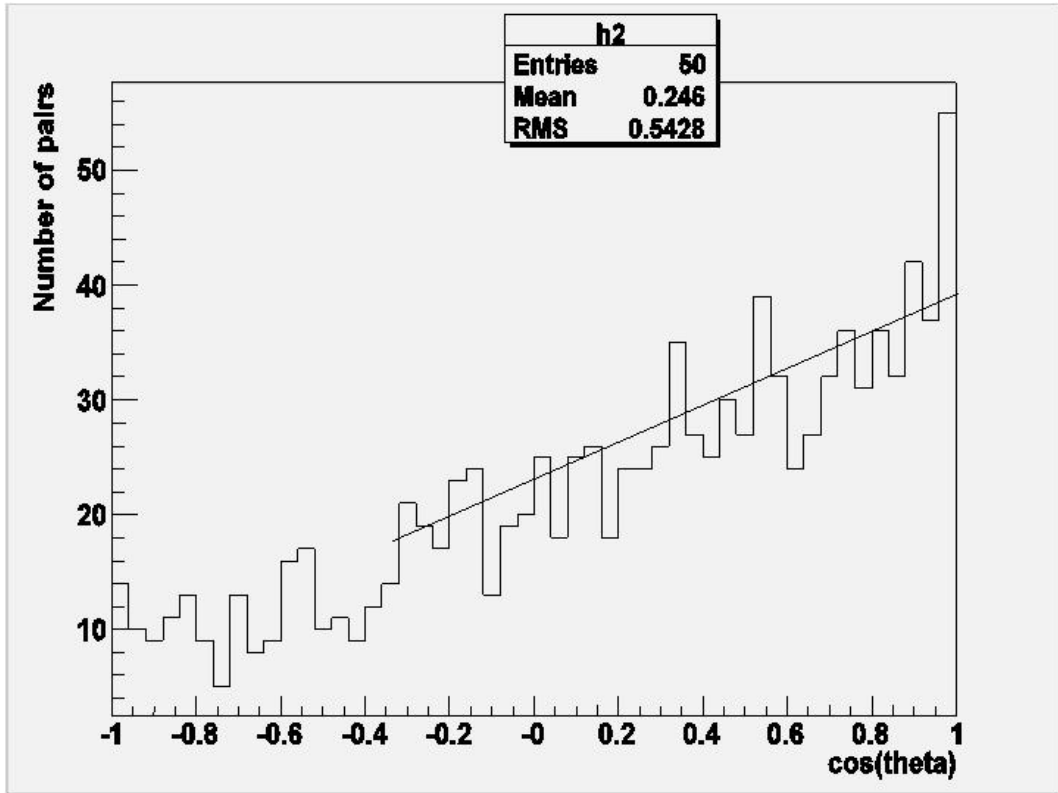


Figure 7.5. Histogram of the cosine of the angle between the average point in the arc and the BL set. Note that an extrapolation into the last bin with a simple poisson interpolation would have yielded to an incorrectly 3σ significance as shown in the figure.

Also because of the correlation, one cannot multiply the probabilities of the last few bins. Therefore, we decided to bin the histogram to 50 bins instead of 100 bins (as binned in the previous study). The bin-to-bin correlation is better understood by replotting Figure 7.5 as simple points in Figure 7.6 (Note that bars simply mark the points and are not error bars). Next, from the MC data sets (10^4 isotropic data sets each equivalent in size to the real data set) we plot the lines representing the normalized to real data median and $\pm 34\%$ intervals (confidence interval) for each angular bin. The median here represents the middle of the distribution of the simulated data sets at each bin, where half of the distribution is above the median and half is below the median. Note that the number points (the histogram points of Figure 7.1) that lie outside the confidence intervals are not $\sim 32\%$ of the total

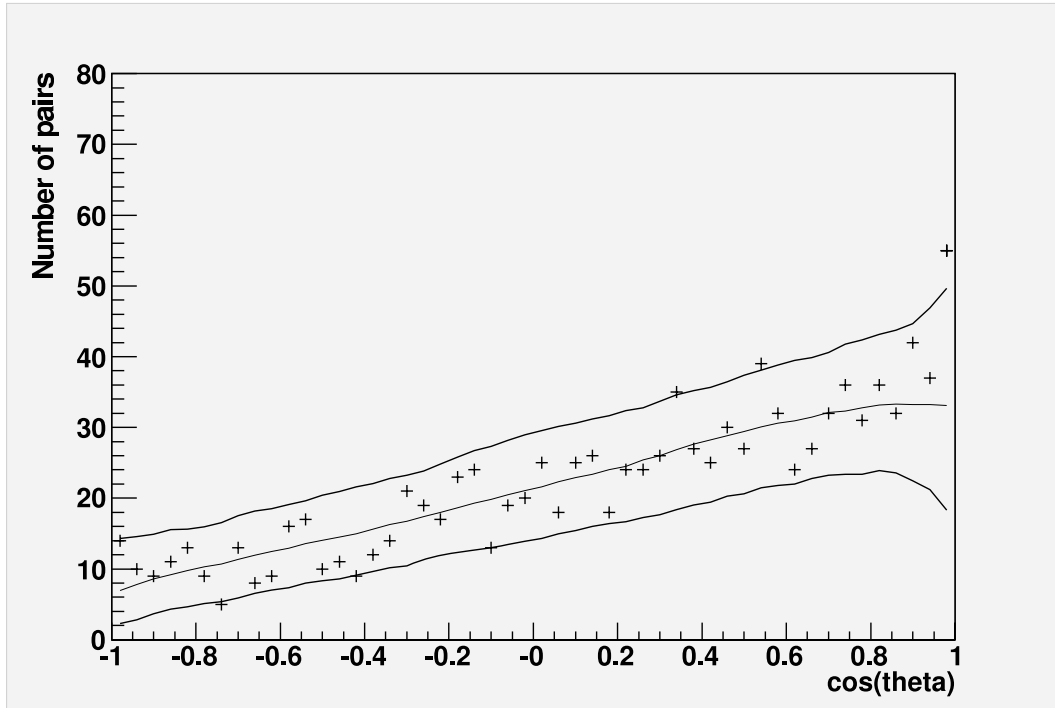


Figure 7.6. This figure shows the histogram in Figure 7.5 as simple points (note that the bars around the points are not error bars). The lines plotted are the normalized to real data median and $\pm 34\%$ intervals of the 10^4 simulated data sets.

number of points, because of the correlation between the bins.

The chance probability of the last bin in Figure 7.5 is of low significance and is equal to 0.095. In addition, the same method of study has also been applied to the BL+HP data set. The cosine histogram between the stereo data set and the BL+HP set is shown in Figure 7.7 and the chance probability of the last bin histogram having a value \geq that found in the real date (Figure 7.7) is of high probability and found to be 0.168.

We made one additional study to examine the excess in the last bin of the cosine histogram in the real data. We compared the cosine histogram in the real data to that of the simulated data using only those sets which had seven arcs (the same number of arcs that were found in the real data set). For this study we simulated additional MC sets and yielded 2500 data sets. Using these sets with seven arcs, the chance probability of the excess in the last bin in Figure 7.5 (correlation with BL set) is found to be of high probability and is equal to 0.084. In addition,

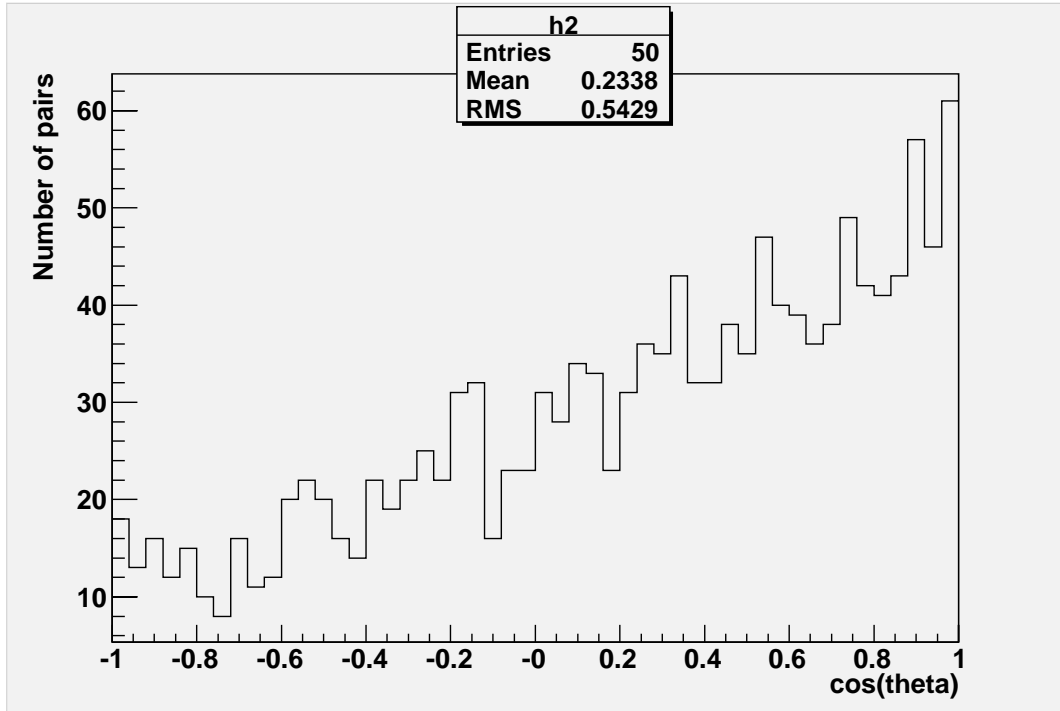


Figure 7.7. Histogram of the cosine of the angle between the average point in the arc and the BL+HP set.

we calculated the chance probability of the excess in the last bin in Figure 7.7 (correlation with BL+HP set) and is also found of high probability and is equal to 0.16.

7.1.3 Conclusion

After applying Hough Transformation to the HiRes stereo data set, we looked for a correlation between the arcs found by Hough Transform, and BL Lacs locations as defined in Veron 10th Catalog were applied. We found small excess in the histogram of the cosine of the opening angle between the arcs and the BL Lac sources. When this excess was investigated by comparison to isotropically simulated data sets, we then found that it is not statistically significant. When we repeated this study for simulated data sets that contained only seven arcs, the statistical significance did not change in any substantial way.

7.2 Bin-to-bin Correlation

In our BL-Lac vs. arcs cross correlation analysis, we found what appears to be a bin-to-bin correlation in Figure 7.5. The correlation is due to the fact that the positions of the BL Lacs are fixed. Therefore, when calculating the opening angle between one event and one BL Lac, the distribution of the angles between that same event and the rest of the BL Lacs is constrained to a smaller subset of possible values.

To demonstrate the existence of the correlation between the bins in Figure 7.5 we calculate the correlation strength between them, also called the Correlation Factor CF. The CF between any two bins is calculated by assigning a vector for each bin. Consider, for example, the vectors for two particular bins, \vec{a} and \vec{b} , given by

$$\vec{a} = (x_1 - \bar{x}, x_2 - \bar{x}, \dots, x_n - \bar{x}) \quad (7.2)$$

and,

$$\vec{b} = (y_1 - \bar{y}, y_2 - \bar{y}, \dots, y_n - \bar{y}) \quad (7.3)$$

where the values of x_1, x_2, \dots, x_n and y_1, y_2, \dots, y_n are the number of entries pairs from the simulated sets for each bin, respectively, n is the total number of entries from the simulated sets and \bar{x} and \bar{y} are the average values of these entries where

$$\bar{x} = \frac{1}{n} \sum_{i=1}^n x_i \quad (7.4)$$

and

$$\bar{y} = \frac{1}{n} \sum_{i=1}^n y_i. \quad (7.5)$$

The CF between the two bins is then given by the cosine of the angle between the two vectors \vec{a} and \vec{b}

$$CF = \cos\theta = \frac{\vec{a} \cdot \vec{b}}{|\vec{a}||\vec{b}|} \quad (7.6)$$

If the two vectors were completely uncorrelated, they would be orthogonal and the CF would equal to zero. In addition, if the two vectors were completely correlated, they would be parallel and the CF would equal one.

The CF between the bins in Figure 7.5, as defined above are plotted in Figure 7.8. The bins are plotted on each axis and are numbered from 1 to 50. The first bin represents the left most bin in Figure 7.5 where the $\cos\theta$ value borders on -1. Accordingly, the last bin represents the right most bin where the $\cos\theta$ value borders on 1. The shading index shows the values of the CF ranging from zero to one.

Figure 7.8 demonstrates that a significant correlation does exist between the bins in the distribution Figure 7.5. To further ensure that our understanding of the source of the correlation between the bins is correct, we repeated the correlation study between 10^4 generated data sets and the BL set. Each MC set contained 271 isotropically generated events (same size as real data) according to HiRes stereo

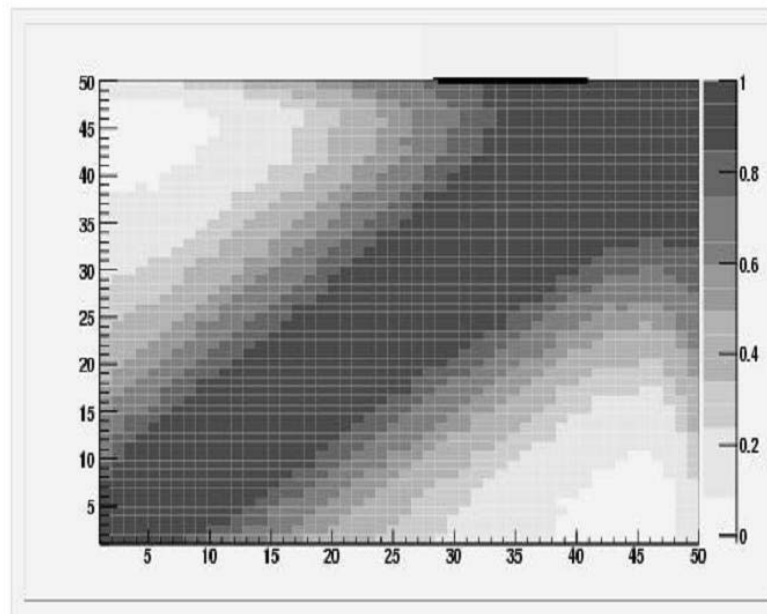


Figure 7.8. The correlation factor between the bin in Figure 7.5. The bin numbers are plotted on each axis. The bins are arbitrary numbered from 1 to 50. The first bin represents the left most bin in Figure 7.5 where the $\cos\theta$ value borders to -1. Accordingly, the last bin represents the right most bin where the $\cos\theta$ value borders to 1. The shading index shows the values of the CF ranging from zero to one.

exposure. We then calculated the CF between the $\cos\theta$ histogram bins. Here θ is the angle between each of the 271 events and the BL set. Figure 7.9 shows the CF between the 50 bins of the histogram. We see that Figure 7.9 contains a much narrower bin-to-bin correlation ridge.

In order to determine whether the decreased correlation in Figure 7.9 is due to the size of the data sample, we repeated exactly the same study between 10^4 generated data sets and the BL set, except that each generated data set contained seven isotropically generated events (equal to the number of arcs found in HiRes stereo data set). The result is shown in Figure 7.10, which displays bin-to-bin correlation ridge comparable to that of Figure 7.8.

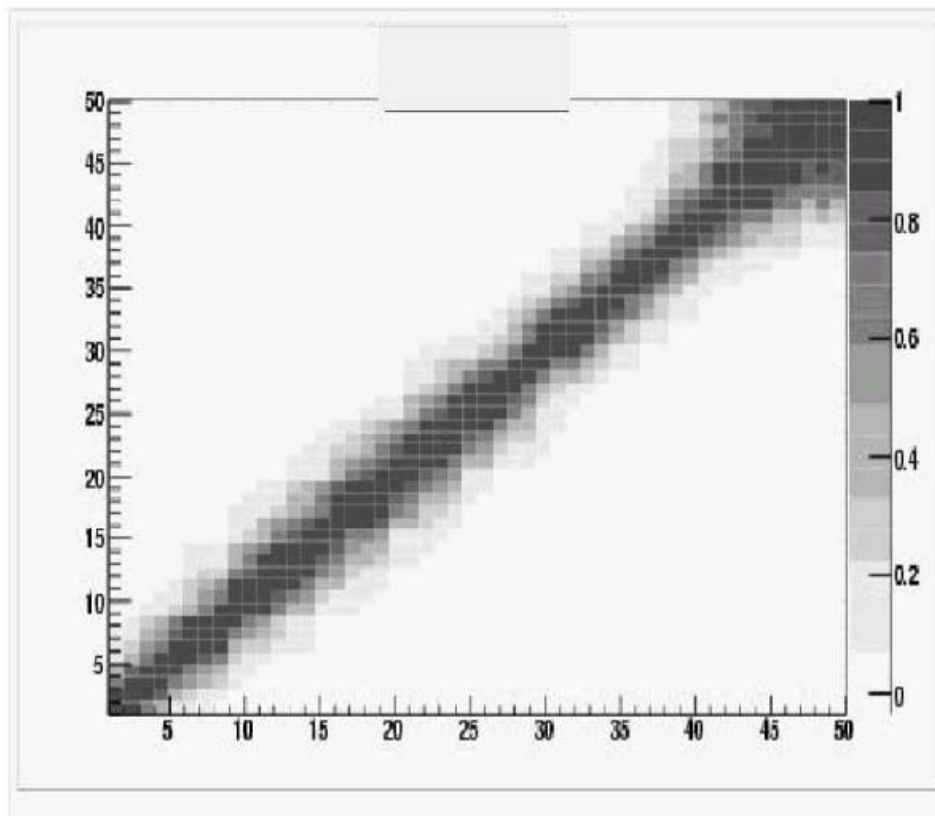


Figure 7.9. The CF between the bins of the $\cos\theta$ histogram, where θ is the angle between the 271 events in each of the 10^4 simulated data sets and BL set. The bin numbers are plotted on each axis. The bins are arbitrary numbered as mentioned in Figure 7.8. The colored index shows the values of the CF ranging from zero to one.

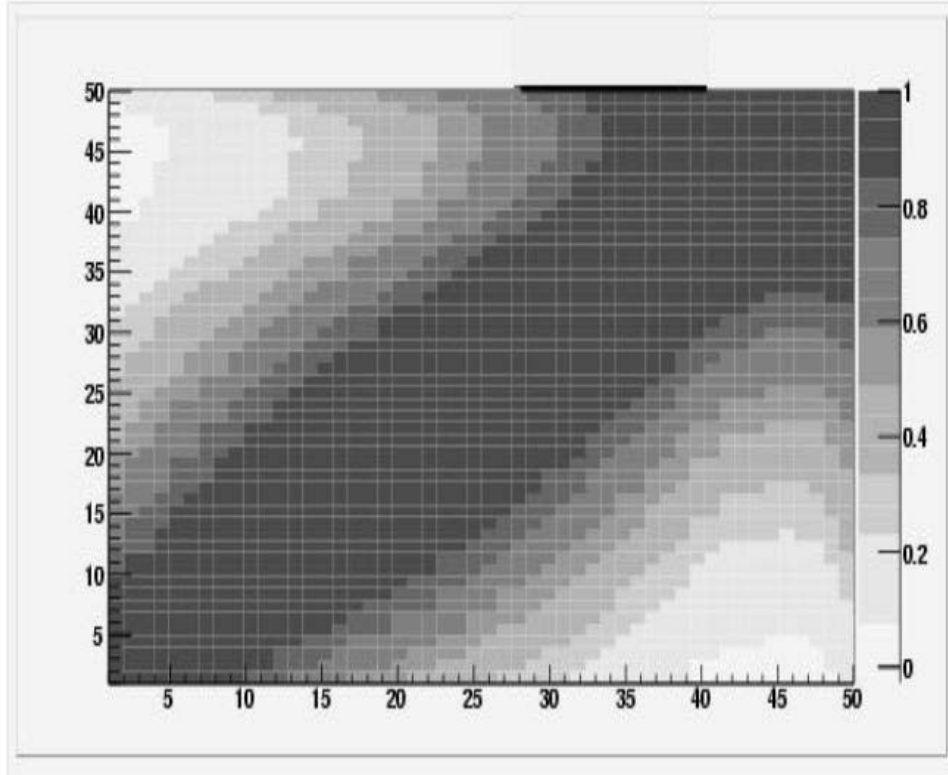


Figure 7.10. The CF between the bins of the $\cos\theta$ histogram, where θ is the angle between the seven events in each of the 10^4 simulated data sets and BL set. The bin numbers are plotted on each axis. The bins are arbitrarily numbered as mentioned in Figure 7.8. The colored index shows the values of the CF ranging from zero to one.

In conclusion, a correlation between the bins in the $\cos\theta$ histogram in Figure 7.5 does exist. However, the breadth or range of such correlation depends on the size of the data sample. As shown in Figure 7.10, the bins in the $\cos\theta$ histogram of a data sample that is statistically similar to the data sample in Figure 7.5 are correlated over much longer range than that for a larger set, shown in Figure 7.9.

Note that because of the correlation between the bins, the distribution of pairs of the 10^4 simulated sets of the $\cos\theta$ histogram (i.e., Figure 7.5) are subject to a larger fluctuation than would be expected for a simple poisson distribution. This is shown in Figure 7.11, where we fit the distribution of values of the right most bin in Figure 7.5 to a Gaussian function. While the Gaussian gives a good description of the distribution, the RMS fluctuation is significantly larger than the poisson

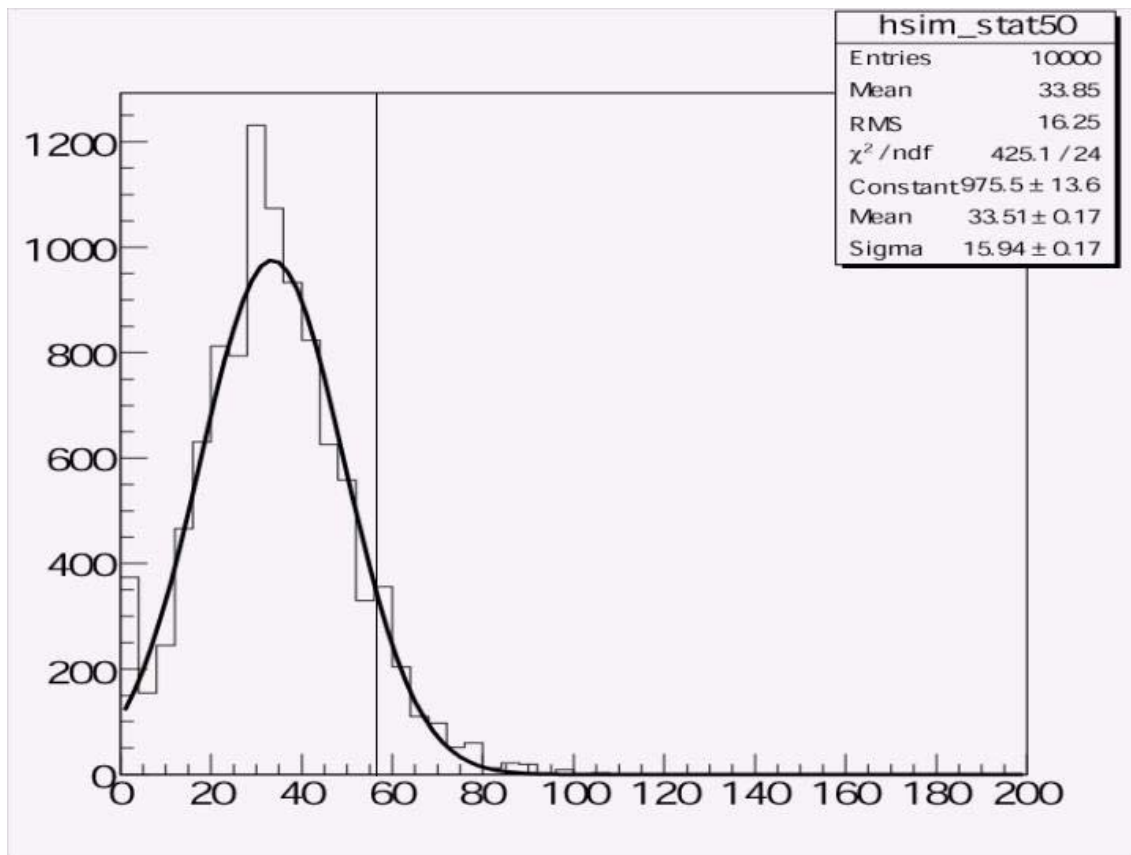


Figure 7.11. This figure shows the distribution of the occupancy level of the 10^4 simulated sets for the right most bin from the cosine theta histogram in Figure 7.5. A vertical line is drawn at the number of pairs found in the real data set at that bin. The probability of finding at least this many pairs in an isotropic data set is then calculated by dividing the area of the curve to the right of the vertical line to the whole area of the distribution.

expectation. This observation tells us that a proper statistical interpolation of the apparent excess in the last bin must be made using equation 1. A naive extrapolation of Figure 7.5 into the last bin with a simple poisson interpretation would have incorrectly yielded a 3σ significance.

CHAPTER 8

THREE POINT CORRELATION

In an attempt to further investigate the existence of clustering in the arrival direction of the UHECR events detected by the HiRes detector, a search for three-event clustering is implemented. We do this by finding the solid angle subtended by the spherical triangle formed using every triplet of events in the HiRes data set used. The resulting histogram of the solid angles distributions is again compared to the cumulative distributions from multiple simulated data set to estimate the significance of any excess form. To correctly assess the significance of any signal the simulated data sets used contain the same size and detector acceptance as that of the real data set. This chapter explains the method used to calculating the signal, the result found from the study and the significance of the outcome.

8.1 Girard's Theorem

To calculate the solid angle of a spherical triangle, we used Girard's theorem. In this section we explain Girard's derivation. We begin by considering a sphere with a radius R , divided into two hemispheres each of which is in turn divided into four spherical triangles. Figure 8.1 illustrates this division. To distinguish the four spherical triangles, a color is assigned to each. In the upper hemisphere, the triangles are colored black (T), blue, green, and red. The lower triangles are colored are grey (T'), blue, green, and red, respectively. In this configuration we are trying to find the area of the spherical triangle T , which is colored in black.

Figure 8.2 shows the triangle T with interior angles denoted by r , g , and b . The angle letters stand for red, green, and blue. The angles are denoted by r , g , and b because they are the opposite and equal to the angles of the red, green and blue spherical triangles. Note that the spherical triangles are divided in such a

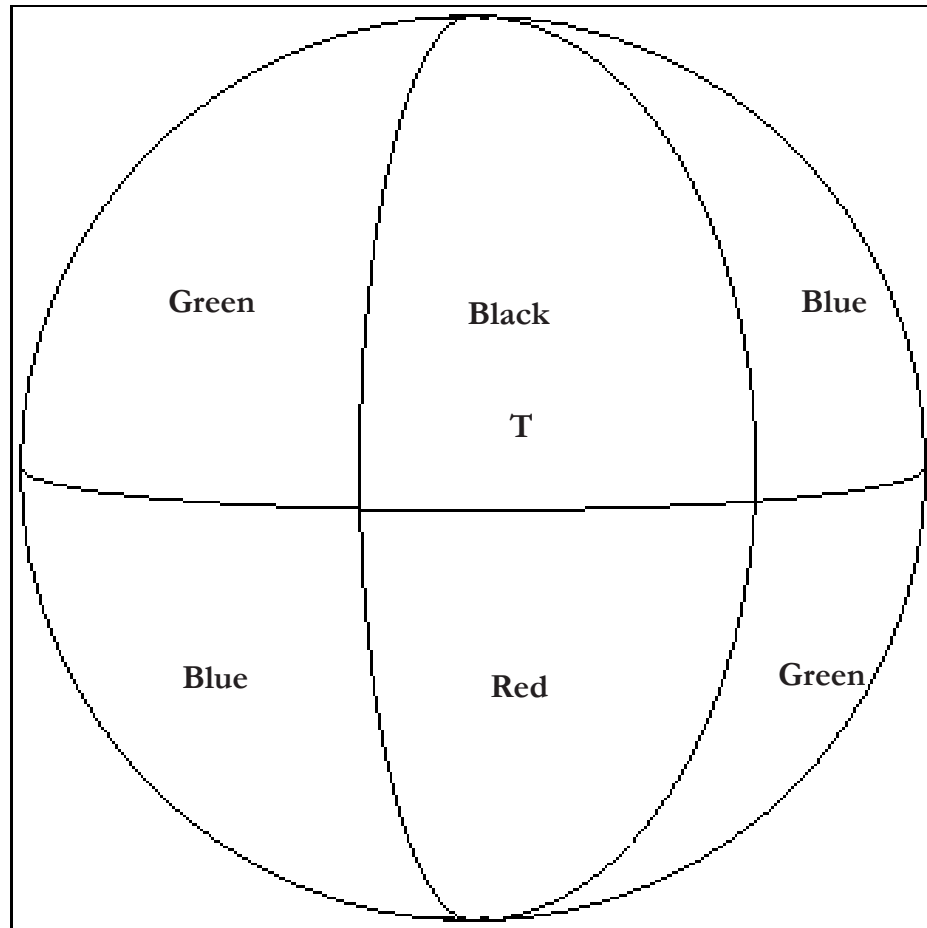


Figure 8.1. A sphere divided into two hemispheres; each hemisphere is divided into four spherical triangles. The upper hemisphere spherical triangles are labeled with the colors red, blue, green and black (T). The lower hemisphere is also divided into four spherical triangles and they are labeled with the colors red, blue, green, and grey (T').

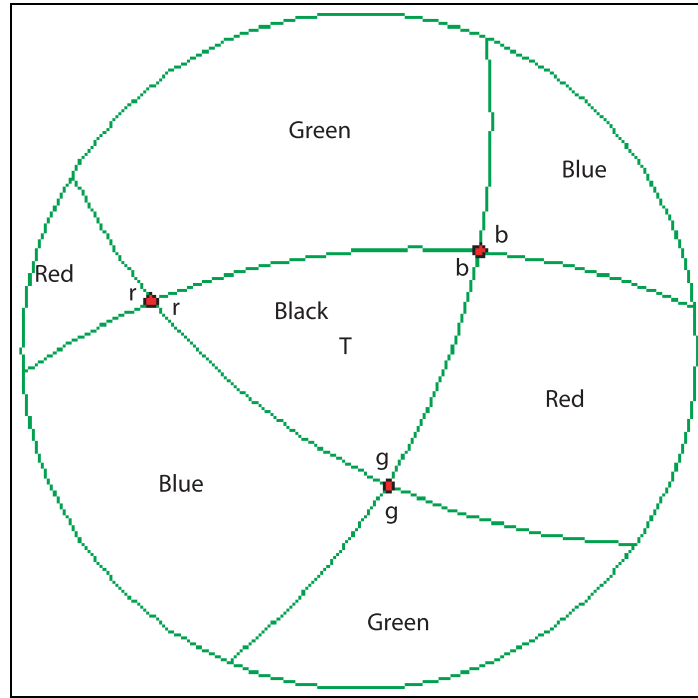


Figure 8.2. This figure shows the angles of the spherical triangle T denoted as r , g , and b . The angles letters stand for red, green, and blue. They are the opposite angles of the red, green and blue spherical triangles and therefore they are equal. Note that it is difficult to draw the green, blue, and red as triangles; they look like they have four sides when in fact they have three sides. The third point of the triangle is located on the back side of the sphere.

way that there are six lunes assigned in this configuration, where a lune is the area bounded by two half great circles as shown in Figure 8.3. The first two lunes are L_R and L'_R . L_R is the lune containing the spherical triangles red (from the lower hemisphere) and T (in the upper hemisphere). L'_R is the lune containing the red (from the upper hemisphere) and T' (in the lower hemisphere). These lunes are referred to as the red lunes. Similarly the second two lunes are the green lunes L_G and L'_G . L_G contains the green (from the lower hemisphere) and T spherical triangles, and L'_G contains the green (from the upper hemisphere) and T' spherical triangles. The same grouping applies to the blue lunes L_B and L'_B . Note that the triangle T is in each of the lunes L_R, L_B, L_G while the triangle T' is in each of the three lunes L'_R, L'_B, L'_G . In addition, note that any point on the sphere that is not

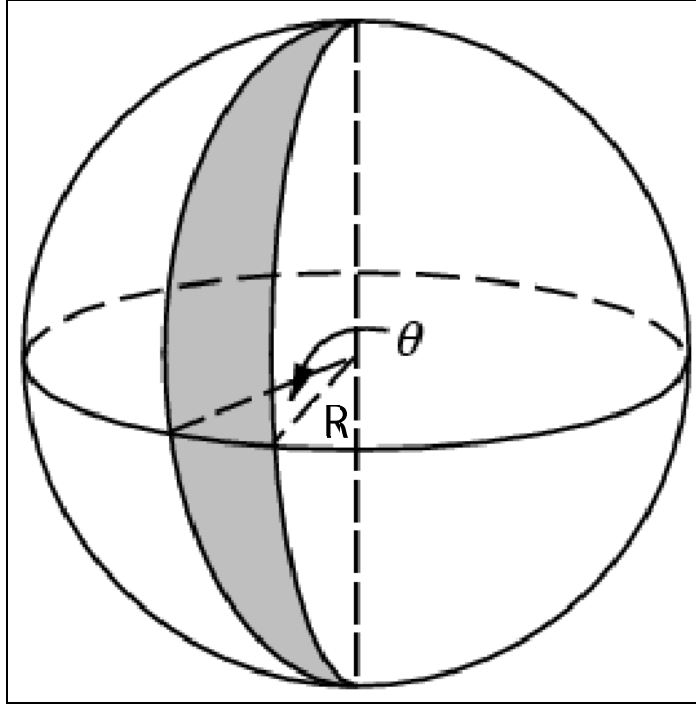


Figure 8.3. This figure shows the lune bounded by two half great circles. The area of the lune described equals $2R^2\theta$ where R is the radius of the sphere and θ is the opening angle between the two half great circles defining the lune.

in T or T' precisely contained in one of the lunes.

We note the areas of the six lunes would sum to the total area of the sphere, but with those of the T and T' spherical triangles double-counted. To calculate the areas of the spherical triangle T , the areas of the lunes are added as follows:

$$\begin{aligned} \text{area}(L_R) + \text{area}(L_B) + \text{area}(L_G) + \text{area}(L'_R) + \text{area}(L'_B) + \text{area}(L'_G) &= \\ \text{area}(\text{sphere}) + 2 \text{area}(T) + 2 \text{area}(T') & \end{aligned} \quad (8.1)$$

Note that the area of a lune is $2 R^2 \theta$, where R is the radius of the sphere and θ is the opening angle between the two half great circles that define the lune. Hence, the previous equation can be rewritten as follows:

$$2R^2r + 2R^2g + 2R^2b + 2R^2r + 2R^2g + 2R^2b = 4\pi R^2 + 2 \text{area}(T) + 2 \text{area}(T') \quad (8.2)$$

Observe that with this configuration the areas of the spherical triangles T and T' are equal by symmetry. Hence, solving for T , we have:

$$area(T) = \frac{1}{4}(2R^2(2r + 2g + 2b) - 4\pi R^2) \quad (8.3)$$

by which we arrive at Girard's formula, which is used in this study to calculate the area of each spherical triangle connecting every three points in HiRes stereo data set:

$$area(T) = R^2(r + g + b - \pi) \quad (8.4)$$

8.2 Spherical Trigonometry

In this section we derive the equations used to calculate the spherical triangle angles. Note that the spherical trigonometry is not usually taught in physics curriculum and it is therefore useful to review in this dissertation.

In order to calculate the spherical triangle area shown in Figure 8.4 the angles A, B, and C (corresponding to r , g , and b in the previous section) need to be determined. For simplicity we also denote the corresponding vertices by A, B, and C. We assume without loss of generality, that the sphere is centered at the origin: $O=(0,0,0)$. With this configuration the position vectors of the vertices can be written as $\vec{a} = OA$, $\vec{b}=OA$ and $\vec{c} = OC$. Each pair of the vectors \vec{a} , \vec{b} and \vec{c} in turns forms a triangle as shown in Figure 8.4. We label the angles adjacent to the origin in these triangles as a' , b' , and c' as shown in the figure where $a' = \angle BOC$, $b' = \angle COA$, $c' = \angle AOB$. Consequently the arc lengths of the side of the spherical triangles are a , b , and c , where $a = R a'$, $b = R b'$, $c = R c'$. And because \vec{a} , \vec{b} , and \vec{c} all have length R , we have:

$$\vec{a} \cdot \vec{b} = R^2 \cos c' = R^2 \cos\left(\frac{c}{R}\right) \quad (8.5)$$

$$\vec{a} \cdot \vec{c} = R^2 \cos b' = R^2 \cos\left(\frac{b}{R}\right) \quad (8.6)$$

$$\vec{b} \cdot \vec{c} = R^2 \cos a' = R^2 \cos\left(\frac{a}{R}\right) \quad (8.7)$$

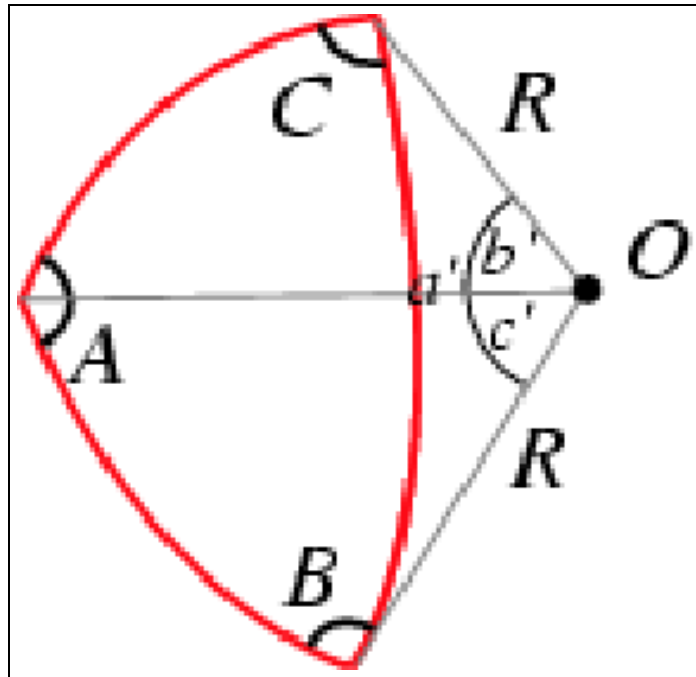


Figure 8.4. This figure shows a generic spherical triangle. The angles of this spherical triangle are denoted by A , B , and C . The spherical triangle is on a sphere of radius R with the center at the origin $O(0,0,0)$. The angles of the side of the triangle are a' , b' , c' [74].

In the subsequent derivation, we will take $R=1$, where then the vectors \vec{a} , \vec{b} , and \vec{c} become unit vectors \hat{a} , \hat{b} , and \hat{c} . The angle A is clearly the same as the angle between the planes defined by the triangles $\triangle AOB$ and $\triangle AOC$, so that

$$\begin{aligned} (\hat{a} \times \hat{b}) \cdot (\hat{a} \times \hat{c}) &= (|\hat{a}||\hat{b}| \sin c)(|\hat{a}||\hat{c}| \sin b) \cos A \\ &= \sin c \sin b \cos A. \end{aligned} \quad (8.8)$$

The cross product of the plane normal can also be expressed using the properties of the triple scale product, and applying the usual vector identity for the resulting triple vector product we therefore have:

$$\begin{aligned} (\hat{a} \times \hat{b}) \cdot (\hat{a} \times \hat{c}) &= \hat{a} \cdot [\hat{b} \times (\hat{a} \times \hat{c})] \\ &= \hat{a} \cdot [\hat{a}(\hat{b} \cdot \hat{c}) - \hat{c}(\hat{a} \cdot \hat{b})] \\ &= (\hat{b} \cdot \hat{c}) - (\hat{a} \cdot \hat{c})(\hat{a} \cdot \hat{b}) \\ &= \cos a - \cos b \cos c \end{aligned} \quad (8.9)$$

Since these two expressions are equal:

$$\cos a = \cos b \cos c + \sin b \sin c \cos A \quad (8.10)$$

Analogously, we find the angles B , and C given by.

$$\cos b = \cos c \cos a + \sin c \sin a \cos B \quad (8.11)$$

$$\cos c = \cos a \cos b + \sin a \sin b \cos C \quad (8.12)$$

Equations 8.10, 8.11, and 8.12 are known as the *cosine rules* (for spherical triangles) ([75], [76], [77]). In addition, using the cross product between the plane normals, $\sin A$ can also be expressed as:

$$\left| (\hat{a} \times \hat{b}) \times (\hat{a} \times \hat{c}) \right| = (|\hat{a}||\hat{b}| \sin c)(|\hat{a}||\hat{c}| \sin b) \sin A \quad (8.13)$$

and hence,

$$\sin A = \frac{|(\hat{a} \times \hat{b}) \times (\hat{a} \times \hat{c})|}{\sin b \sin c} \quad (8.14)$$

$$= -\frac{|\hat{a}[\hat{b}, \hat{a}, \hat{c}] + \hat{b}[\hat{a}, \hat{a}, \hat{c}]|}{\sin b \sin c} \quad (8.15)$$

$$= \frac{[\hat{a}, \hat{b}, \hat{c}]}{\sin b \sin c} \quad (8.16)$$

Where $[\vec{a}, \vec{b}, \vec{c}]$ denotes a scalar triple product. Similarly,

$$\frac{\sin A}{\sin a} = \frac{\sin B}{\sin b} = \frac{\sin C}{\sin c} = \frac{[\hat{a}, \hat{b}, \hat{c}]}{\sin a \sin b \sin c} \quad (8.17)$$

equation 8.17, is known as the *law of the sines* (for spherical triangles) ([75], [76], [77]).

In addition, we also used the analogs of the law of cosines for the angles of spherical triangles,

$$\cos A = -\cos B \cos C + \sin B \sin C \cos a \quad (8.18)$$

$$\cos B = -\cos C \cos A + \sin C \sin B \cos b \quad (8.19)$$

$$\cos C = -\cos A \cos B + \sin A \sin B \cos c \quad (8.20)$$

$$\cos A = \csc b \csc c (\cos a - \cos b \cos c) \quad (8.21)$$

$$\sin a \cos B = \cos b \sin c - \sin b \cos c \cos A \quad (8.22)$$

$$\cos a \cos C = \sin a \cot b - \sin C \cot B \quad (8.23)$$

using equations 8.17, 8.21, 8.22, and 8.23 ([75], [76], [77]) the values of the angles A, B, and C are determined. In this way, given the direction cosines of these events in the form of unit vectors a' , b' , and c' , we can calculate the solid angle of the spherical triangle formed by these events.

8.3 Search for Significant Excess

In order to identify the statistically significant clustering we look for excess in the real data over what is expected from the simulated isotropic background. The significance of the clustering of three points in the data is found by calculating

the solid angle that is contained between every three points using the equations (8.17, 8.21, 8.22, 8.23, and 8.4). The result is shown in Figure 8.5 where the plot shows the histogram of the solid angle of every triplet of events in the HiRes stereo data set (same data set described in Chapter 6). The histogram shows the number of triplets vs. the spherical triangle area. The distribution from the real data set is shown in points. In addition, Figure 8.5 shows the mean and $\pm 1\sigma$ limits from the distribution for 10^3 simulated data sets. We note a clear discrepancy between the data points and the MC average in that the simulation predicts on average more triplets at large solid angles, which then results in an apparent excess in the data because of the equal normalization. A possible and likely explanation for this discrepancy is the observation that the MC detector simulation appears to accept more events at larger zenith angle than are actually observed. This flaw in the simulation has the effect of over-populating the sky below the equator, and these events contribute to an over-abundance of large-solid angle triplets in the simulation.

However, because we are looking for clustering at small solid angles, we can circumvent this problem by concentrating on solid angles of relatively nearby triplets. To this end, we make a cut on the angular separation between any pair of events within a triplet to be less than 10 degrees. Figure 8.6 shows the histogram of the occupancy level vs. the spherical triangle area with the angular separation cut. The real data are shown in points. In particular, the solid lines again show the mean and the $\pm 1\sigma$ limits. The plot shows the data points to lie well within the MC expectations, with no excess seen at small solid angles. The chance probability for the value of the real data in the first bin is calculated by counting the number of times the simulated data sets yield to a stronger signal. The probability of the signal to be greater than 14 (the value of the first bin) is found to be equal to 0.75. Hence, no significant signal is found of small scale clustering for the HiRes stereo data set using the three point correlation method.

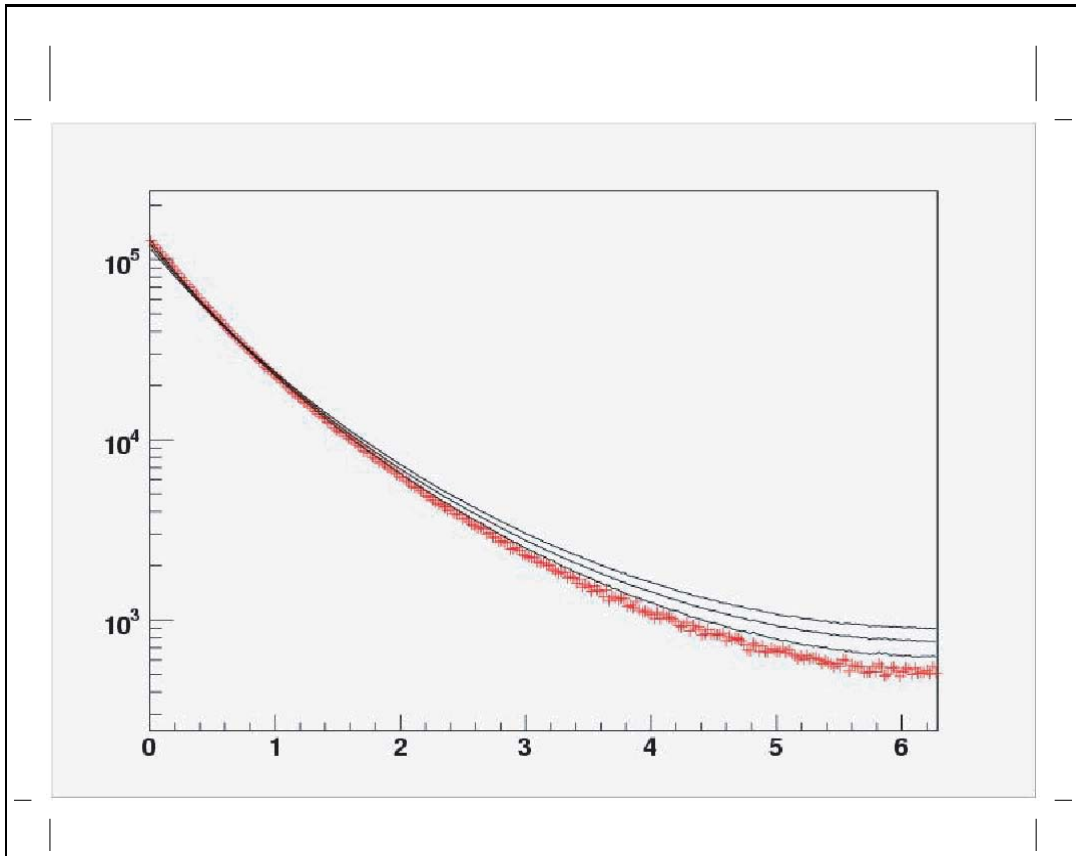


Figure 8.5. A histogram of the area of the spherical triangles. The dotted points represent the spherical triangles found in HiRes stereo data set. The lines represent the mean and the $\pm 1\sigma$ for the simulated data sets.

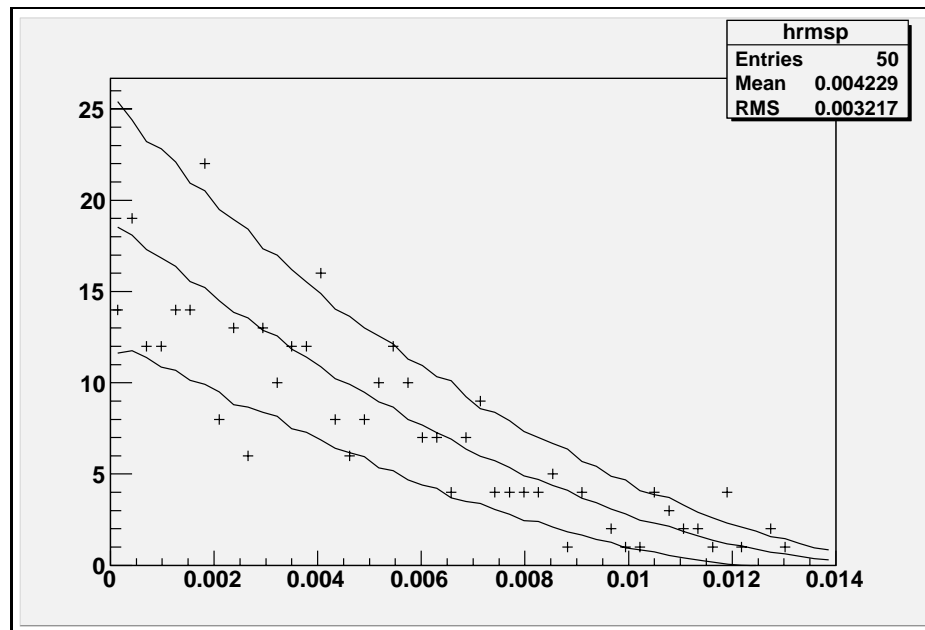


Figure 8.6. A histogram of the area of the spherical triangles. The dotted points represent the spherical triangles found in HiRes stereo data set. The lines represent the mean and the $\pm 1\sigma$ limits for the simulated data sets. The opening angles between each two points of the the three points are 10 degrees.

8.3.1 Cross Correlation Between the Centroid of the Triplets With Small Solid Angles and BL-Lacertae

BL-Lacertae objects are a well-motivated source for the UHECR events as explained in the previous chapter. In this section we search for the cross correlation between triplets with small spherical triangles with the BL-Lac objects. The cross correlation is tested with the triplets of area of $\Omega < 0.004$ and BL-Lacs in the BL+HP set also defined in the previous chapter. The spherical triangle area $\Omega < 0.004$ was calculated as the area of the three points in the diagram shown in Figure 8.7. To explain this diagram assume three points on an arc where the separation angle between the two end points is 10 degrees, if the middle point is displaced by a degree above the arc and the two end points are displaced by a degree below the arc than the resultant spherical triangle will have an area of $\Omega = 0.004$. This is the area chosen for the cut on the spherical triangles areas in the real data set of 271 events.

To investigate the cross correlations between the 207 triplets in the real data set with the BL-Lacs in the BL+HP set we plot the histogram of the $\cos(\theta)$ where θ is the angle between the center of each of the 207 triplets and the BL+HP set. Figure 8.8 shows this histogram, where the cross correlation in the real data set is shown in points and the lines represent a 1000 simulated data sets mean and $\pm 1\sigma$. Note that the mean of the simulated sets does not represent the mean of the real data sets. The reason is that each simulated data set contains a different number of triplets from that found in the real data set. Figure 8.9 shows the distribution of the triplets for the 1000 simulated data sets with a spherical triangle area $\Omega < 0.004$. The line in this figure represents the 207 triplets found in the real data set.

To circumvent the discrepancy between the mean of the simulated sets and that of the real data set we need to normalize the simulated data sets to that of the real data set. Figure 8.10 shows the histogram of $\cos(\theta)$, where θ is the opening angle between the middle point of the spherical triangles with the spherical triangle area $\Omega < 0.004$ and the BL+HP set. Note that the points represent the real data set. The lines represent the normalized to real data simulated sets mean and $\pm 1\sigma$. The

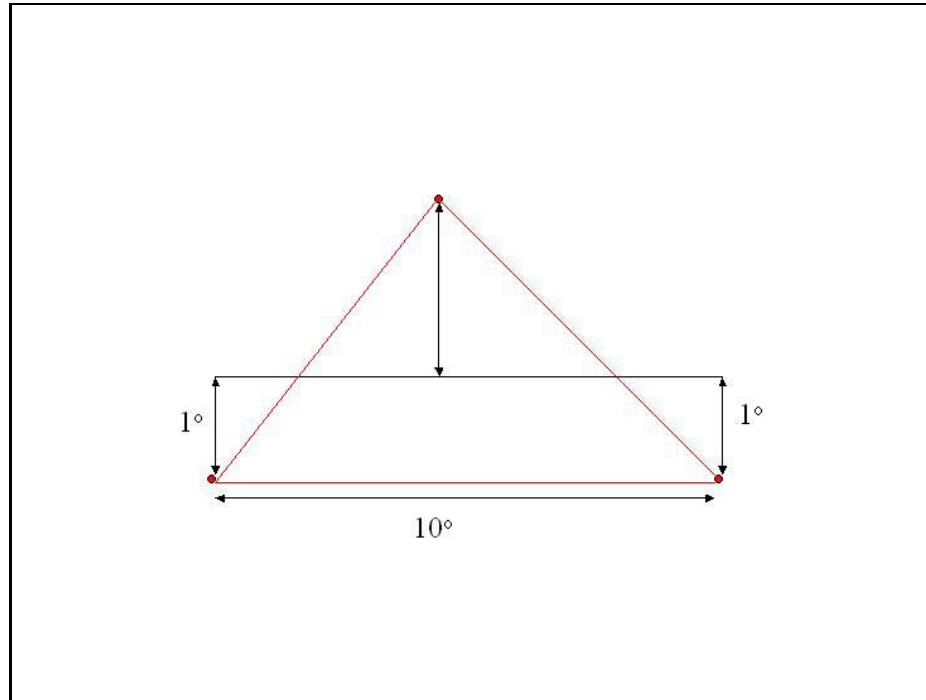


Figure 8.7. A diagram of three points with a separation angle between the furthest two points of 10° . The middle point of the triangle is displaced one degree up and the furthest two points are displaced one degree down from where the three points would be placed on the same arc.

probability of the last bin where $\cos(\theta)$ is close to 1 is equal to 0.3. Such probability is high and implies no cross correlation between the triplets found in the real data set and that of the BL+HP data set.

8.3.2 Three Point Correlation With the BL-Lacertae

For an additional search for a possible correlation between the HiRes stereo data with the BL-Lacertae objects we used the three point correlation method. The correlation is identified by calculating the area of spherical triangles that is contained between two points of the real data and one point from the BL-Lacertae object. Figure 8.11 shows the histogram of the spherical triangle areas of the real data in points compared to that of the 10^3 simulated data sets mean and $\pm 1\sigma$ from the mean in solid lines. The chance probability for the value of the real data to be greater than 55 (the value of the first bin) is found to be equal to 0.054. Hence,

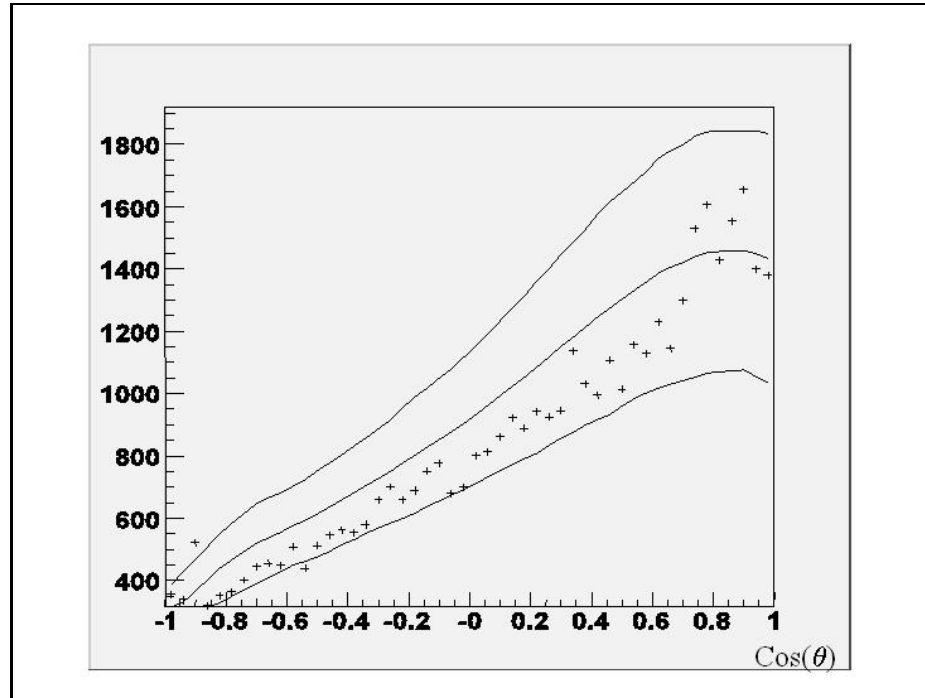


Figure 8.8. A histogram of $\cos(\theta)$, where θ is the opening angle between the middle point of the spherical triangles with the spherical triangle area $\Omega < 0.004$ and the BL+HP set. The points represent the real data set. The lines represent the 1000 simulated sets mean and $\pm 1\sigma$.

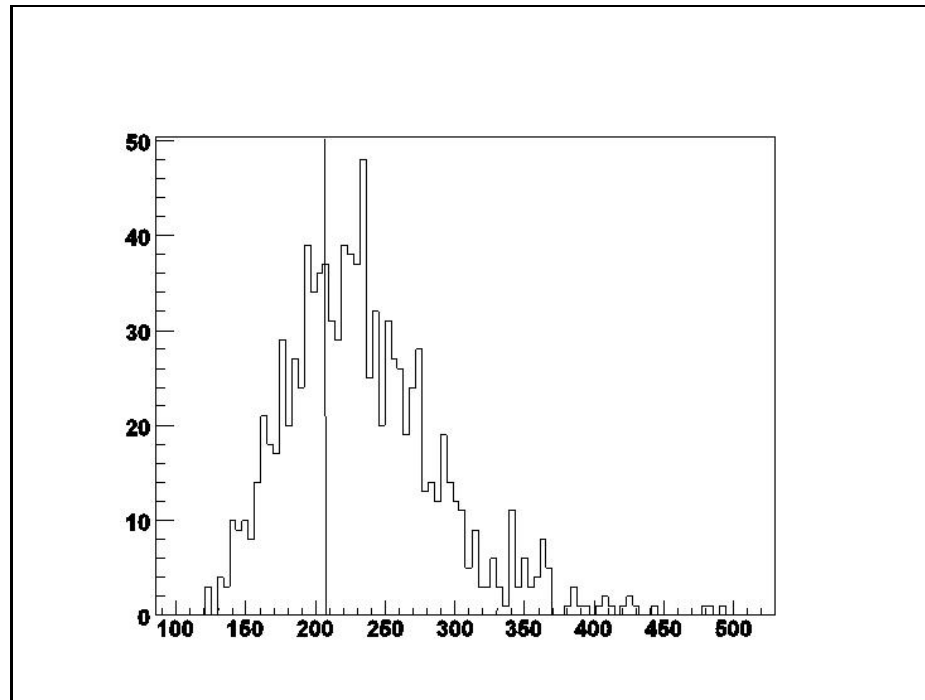


Figure 8.9. The distribution of the number of spherical triangles with a spherical triangle area $\Omega < 0.004$ in a 1000 simulated data sets. The line in this distribution represents the number of spherical triangles in the real data set.

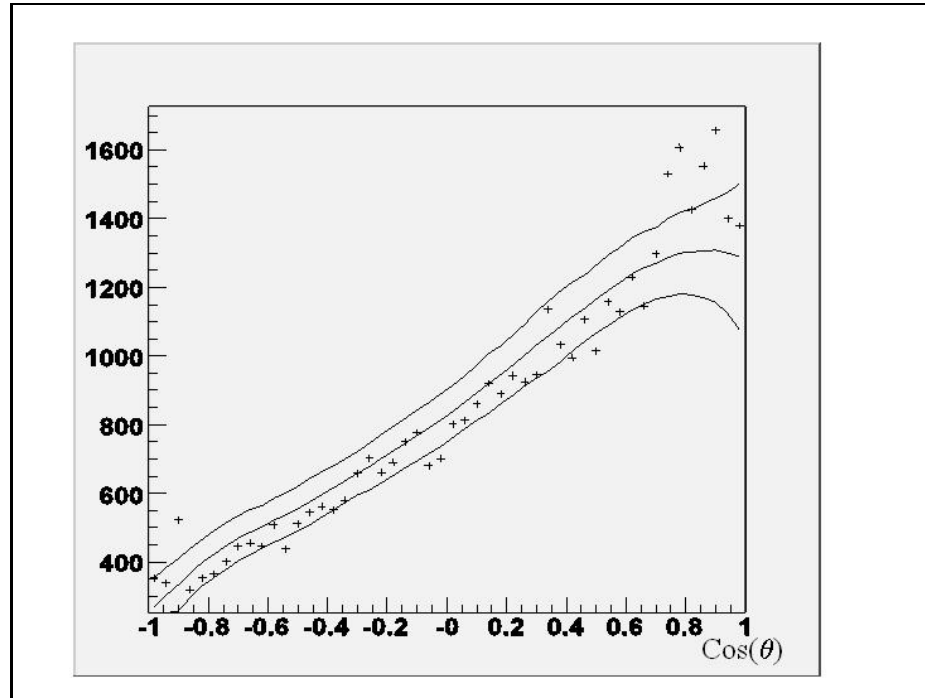


Figure 8.10. The histogram distribution of the $\cos(\theta)$, where θ is the opening angle between the middle point of the spherical triangles with the spherical triangle area $\Omega < 0.004$ and the BL+HP set. The points represent the real data set. The lines represent the normalized to real data simulated sets mean and $\pm 1\sigma$.

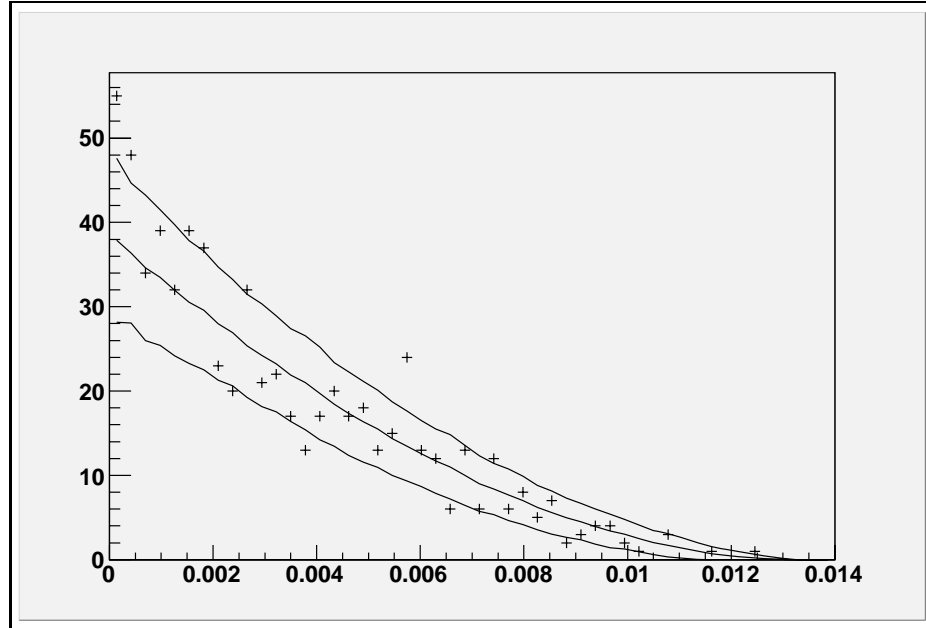


Figure 8.11. A histogram of the area of the spherical triangles. The dotted points represent the spherical triangles found in HiRes stereo data set and the BL-Lacertae, where two points are from the data set and the third point is from the BL-Lacertae location. The lines represent the mean and the $\pm 1\sigma$ for the simulated data sets with the same study. The opening angles between each two points of the the three points is 10 degrees.

No significant signal is found for the HiRes stereo data set with the BL-Lacertae objects using the three point correlation.

8.4 Conclusion

In this chapter we described a search for small scale clustering in the HiRes stereo data set using three point correlation. The search is applied by histogramming the spherical triangle area subtended by triplets in the HiRes stereo data set. To circumvent the tendency for the simulation to generate more events at large zenith angles, we required that every pair in a triplet lie within 10 degrees of angular separation. The result from the histogram is then compared to that found in the simulated data sets. The simulated data sets were generated to have the same exposure as that of the real observed data. No excess of small scale clustering in the HiRes stereo data set is found.

In addition, we looked for cross correlation between the HiRes stereo data triplets with $\Omega < 0.004$ and that of the BL-Lacs in the BL+HP set. No significant correlation was found between the triplets with such an area cut and that with the BL-Lacertae objects.

Also, we looked for correlation between the HiRes stereo data set and the BL-Lacertae objects using the three point correlation. The strategy used in this study is looking for three points where two of the three points are from the data set and the third one is a BL-Lacertae location, each of which has a maximum angular separation of 10 degrees. No significant correlation was found between the data set and the BL-Lacertae objects.

CHAPTER 9

FOUR POINT CORRELATION

In the previous chapter we looked for three point correlation in the HiRes stereo data set using their spherical triangle area. In this chapter we will extend the technique to four point correlation in an attempt to further investigate clustering in the HiRes stereo data set. We do this by calculating the solid-angle/area bounded by each quadruple of events in the data set. The resulting histogram of the solid angle areas is then compared to simulated data sets to assess correctly for the significance of any excess.

9.1 Four Point Configurations

There are two distinct angular configurations for any set of four events. These are shown in Figure 9.1. The figure on the right hand side shows four points where one point is completely contained inside the spherical triangle defined by the outer three points. In contrast, The figure on the left hand side shows four points that make a spherical quadrilateral. The area of each of these configurations is calculated differently. In this section we will give a description of the computational algorithm for distinguishing between the two configurations, and how the solid-angle is calculated in each case.

9.1.1 Configuration 1: Spherical Triangle With Interior Point

For those quadruplets that have one point that lies inside of the spherical triangle defined by the other three (see, for example, the left side of Figure 9.1). We take the solid-angle/area of the quadruplet as the area of the exterior spherical triangle, as shown in Figure 9.2. As before, the exterior area of the spherical triangle is calculated by $\Omega = A + B + C - \pi$, where A , B , and C are the angles of the exterior

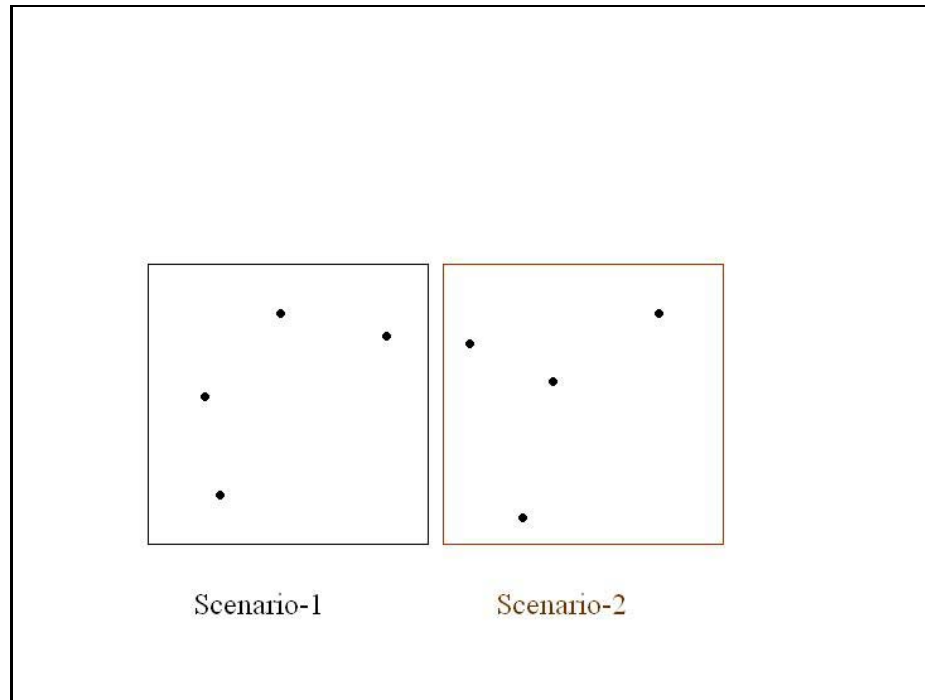


Figure 9.1. The configuration of four points on a sphere. The left hand side figure shows a spherical quadrilateral. The right hand side figure shows four points where one point is inside a spherical triangle contained by the outer three other points.

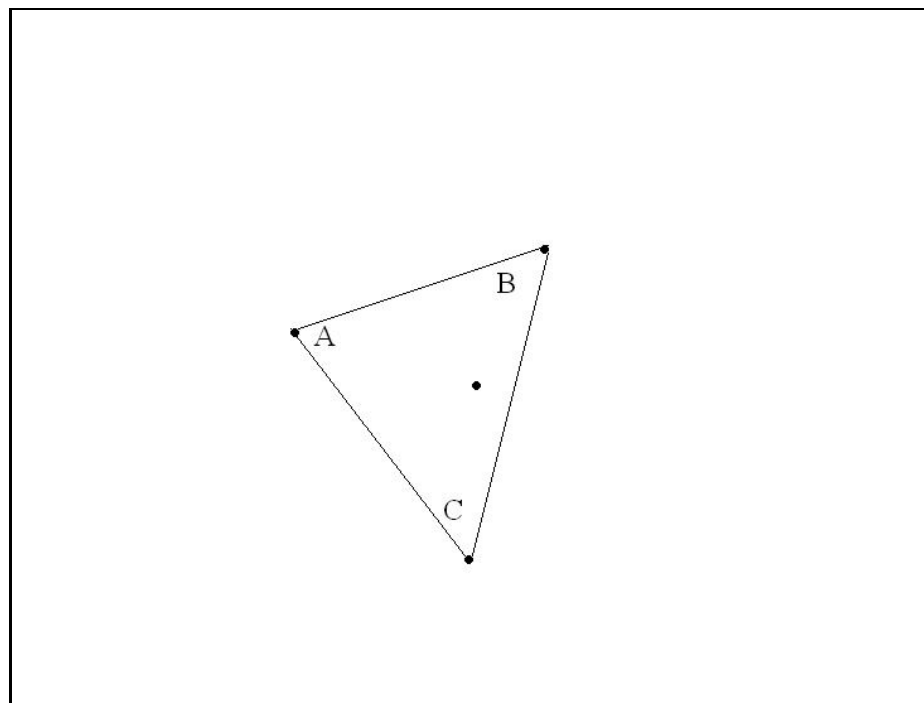


Figure 9.2. The area of the second configuration is calculated as the area of the spherical triangle made by the outer three points.

spherical triangle.

It should be noted that this assignment of the solid-angle/area to the exterior-triangle is not unique, and actually represents the maximum polygonal area that subtends to quadruplet. We have chosen this definition because it is the simplest choice and most consistent with the intended use in an auto correlation study.

9.1.2 Configuration 2: Spherical Quadrilateral

The second configuration is shown on the left hand side of Figure 9.1. It describes four points on a sphere making a spherical quadrilateral. The enclosed solid angle/area for quadrylets of this type is calculated is by dividing the quadrilateral into two spherical triangles. The actual division can be done in two different ways, as illustrated in Figure 9.3. The total solid angle/area is simply the sum of these two triangles, and the value is the same for the two divisions.

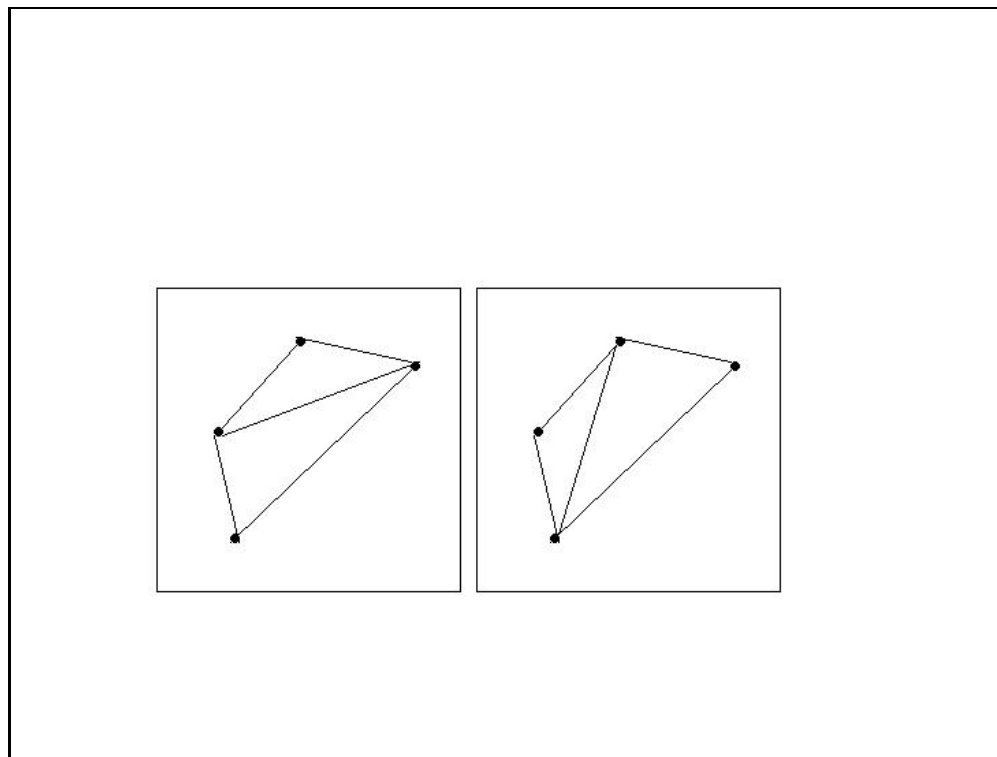


Figure 9.3. Two different divisions of a spherical quadrilateral into two spherical triangles. The same overall solid-angle/area is obtained from these same two triangles, regardless of which division is used.

9.2 Classification of Quadruples

For each quadruple of events, we first determine its classifications according to Figure 9.1. This is accomplished by a sequence of three tests, described in the following paragraph. First, we arbitrarily assign the numbers 1-4 to the four events. We then calculate the angles θ_{213} and θ_{214} , where $\theta_{213} = \angle 213$ and $\theta_{214} = \angle 214$. The angle θ_{213} and θ_{214} are compared. If $\theta_{214} > \theta_{213}$ then the vertices numbering stays the same. If $\theta_{214} < \theta_{213}$ then labels 3 and 4 are reversed to enforce condition $\theta_{214} > \theta_{213}$. Figure 9.4 shows how the four vertices and the angles are labeled after this assignment.

After the four points are numbered and arranged as described above, we proceed to determine if point number 3 lies inside or outside the spherical triangle defined by the vertices $\Delta 124$. To do so, we calculate $\theta_{tot} = \theta_{132} + \theta_{134} + \theta_{431}$, where $\theta_{132} = \angle 132$, $\theta_{134} = \angle 134$ and $\theta_{431} = \angle 431$. If θ_{tot} equals 2π then point number 3 is inside the spherical triangle $\Delta 124$ as shown in Figure 9.5. If θ_{tot} does not equal 2π then point 3 is outside the spherical triangle $\Delta 124$ and the configuration is a spherical quadrilateral. Like the one in Figure 9.4.

Apart from the configurations shown in Figure 9.4 and 9.5, there remains one more possibility, where vertex 1 lies in the middle of the spherical triangle $\Delta 234$ as illustrated in Figure 9.6. Such configuration is tested by calculating $\theta_{tot2} = \theta_{312} + \theta_{214} + \theta_{413}$, where $\theta_{312} = \angle 312$, $\theta_{214} = \angle 214$ and $\theta_{413} = \angle 413$. If $\theta_{tot2} = 2\pi$ then vertex 1 is inside the spherical triangle $\Delta 234$. Otherwise, vertex 1 is outside the spherical triangle $\Delta 234$ and the configuration of the four points is again a spherical quadrilateral.

9.3 Four Point Auto Correlation

As in the case of the three point autocorrelation study, we compare the distribution of the solid angles from the real data to that found in the simulated isotropic MC sets. The only difference is that we are using quadruplets rather than triplets. The solid angle calculated has been described in the preceding section. As in the case of the three point study, we have made a cut on the angular separation

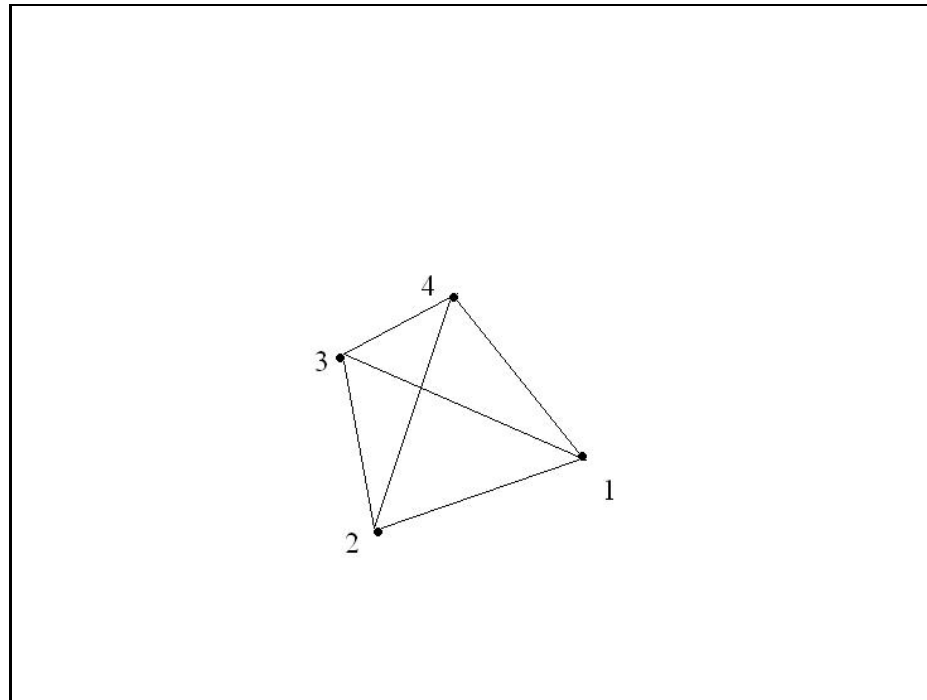


Figure 9.4. First condition where point number three is outside the spherical triangle 124.

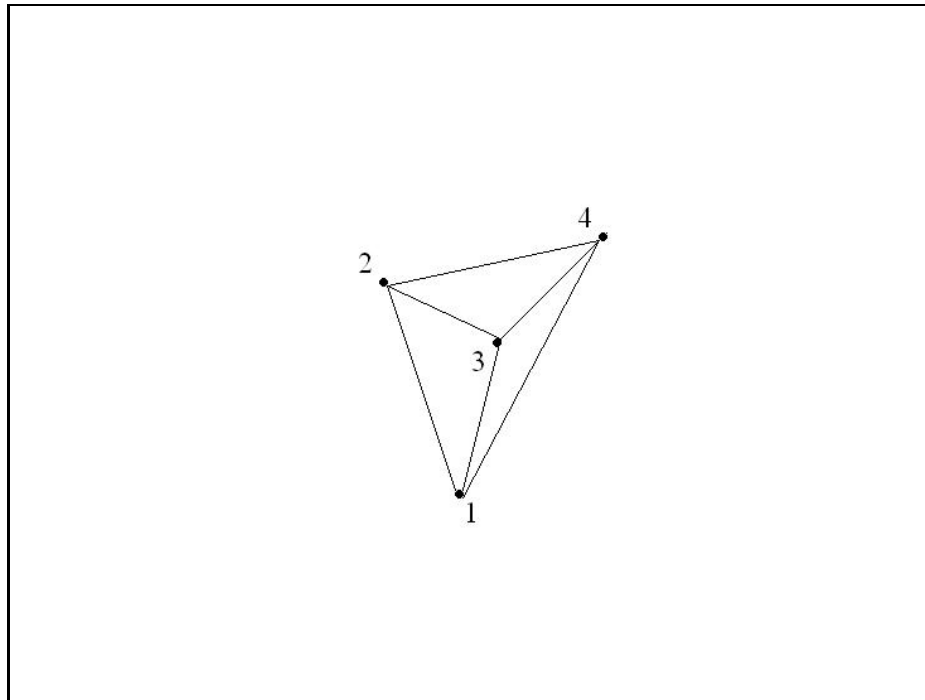


Figure 9.5. Second condition where point number three is inside the spherical triangle 124.

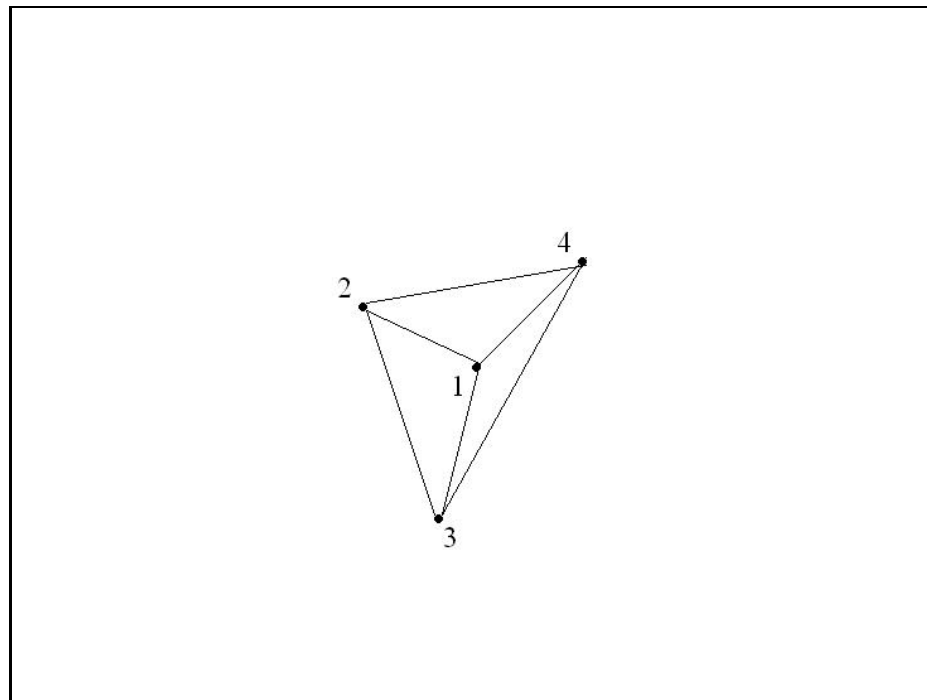


Figure 9.6. Third condition where point number one is in the middle of the spherical triangle 234.

between pairs of points in the quadruplets to be less than 10° . This is because we are primarily, interested in small-scale clustering, and we have already seen that the MC does not describe the large-separation characteristics of the data set well.

Figure 9.7 shows the occupancy level vs. the solid angle area of quadruplets with the 10° angular separation cut. The actual HiRes data set is shown by the data points. The mean and $\pm 1\sigma$ intervals are shown by the solid lines. The figure clearly shows no obvious excess in the lowest bins. The chance probability of the first bin from 1000 MC sets area (corresponding to the smallest solid angle) is calculated by dividing the number of simulated data sets that yielded a stronger signal than that of the real data set and dividing it by the total number of simulated data set. In this case, the value was found to be ~ 0.70 . Hence, no significant four point clustering is found in the data.

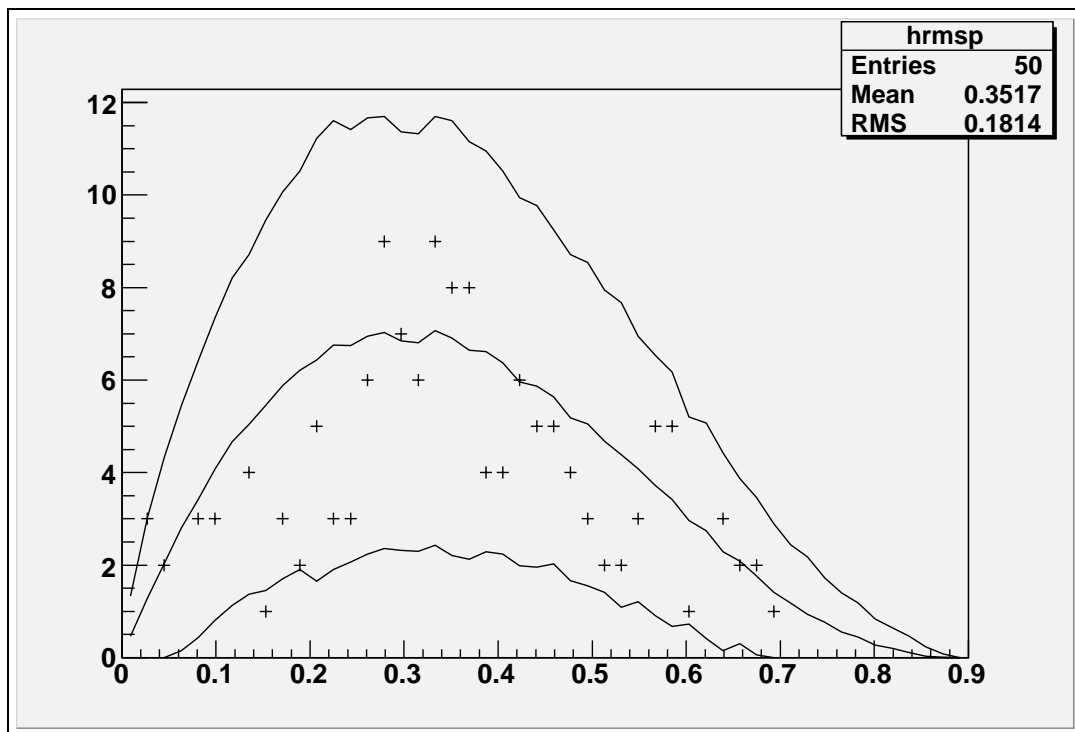


Figure 9.7. The histogram of the solid angle between each of four points with the angular separation cut. The point represents the real data sets while the solid lines represent the mean and the $\pm\sigma$ of a 1000 simulated data set.

9.4 Conclusion

It is interesting to note that over the range of the plot, the fluctuation in the data points lie well within the $\pm 1\sigma$ intervals from the simulation, which suggests that we once again have the significant bin-to-bin correlation that we describe in detail in Chapter 7. We also note that the data points are systematically low compared to the MC mean. From this we conclude that the four point auto correlation study is pushing the limit of the reliability of the simulation. For this reason, we decided not to extend the study to four point BL-Lac correlation or to five point auto correlation.

CHAPTER 10

CONCLUSION

Several studies were applied to HiRes mono and stereo data sets in searching for correlation with point sources in the sky. Most of these searches have concluded that the arrival direction of the ultra high energy cosmic rays is isotropic. In this dissertation we searched for patterns in the HiRes stereo data. The patterns are expected due to the smearing of the ultra high energy cosmic rays from the magnetic field. Such patterns are expected to form when ultra high energy cosmic rays coming from the same source pass through the magnetic field. If the particles are charged they will get deflected, their deflection would depend upon their energies.

The first pattern we investigated is the arc pattern. Such pattern is searched for using Hough Transform. No statistically significant arcs were found. Furthermore, we investigated the correlation of the arcs found with the Bl-Lacertae objects and found the correlation of high probability when compared to isotropically simulated data sets.

In addition, we investigated three and four point correlation where we histogrammed the solid angle area contained between every three and four points in the HiRes stereo data set. Excess in the small solid angle area would correspond to clustering in the arrival direction of the cosmic ray events; it could also imply an arc structure in the data set. We found no statistically significant clustering in the three and four point correlation.

Furthermore, we searched for a possible three point correlation between the cosmic rays' arrival direction and a point from the Bl-Lacertae data set. The correlation was investigated by two methods. First, we looked for excess in the small area of the solid angle contained between every two points in the data set and the Bl-Lacertae data set. Second, we looked for the correlation between the triplets

in the data set with an $\Omega < 0.004$ and the BL-Lacertae set. Using both methods the correlation with the BL-Lacertae was of high probability when compared with that of isotropically simulated data sets.

In conclusion, we did not find any statistically significant patterns in the HiRes stereo data. We also did not find any correlation between the patterns found in the data and that of the BL-Lacertae set. Currently, the sources of the ultra high energy cosmic rays are as mysterious as ever. We hope with future experiments we will be able to understand the acceleration mechanisms and find the sources of the ultra high energy cosmic rays.

REFERENCES

- [1] J.W. Cronin, *The Most Energetic Particles in the Universe*, Rev. Mod. Phys. **71**, 2 (1999).
- [2] R.A. Millikan and G.H. Cameron, *The Origin of the Cosmic Rays*, Phys. Rev. **32**, 533 (1928).
- [3] A.H. Compton, *A Geographic Study of Cosmic Rays*, Phys. Rev. **43**, 387 (1933).
- [4] C. Anderson, *The Positive Electron*, Phys. Rev. **43**, 491 (1933).
- [5] L. Brown, *The Discovery of Antimatter, the Autobiography of Carl David Anderson, the Youngest Man to Win the Nobel Prize*, Phys. Tod. Online, **53**, 10, 81 (1999). [<http://www.aip.org/pt/vol-53/iss-10/p81.html>].
- [6] P. Auger and R. Maze, C.R. Acad. Sci. Ser. **B 207**, 228 (1938).
- [7] P. Auger, P. Ehrenfest, R. Mase, J. Daudin, and A. Freon Robley, *Extensive Cosmic-Ray Showers*, Rev. Mod. Phys. **11**, 288-291 (1939).
- [8] E. Fermi, *On the Origin of Cosmic Radiation*, Phys. Rev. **75**, 1169 (1949).
- [9] K. Greisen, *End to the Cosmic Ray Spectrum?*, Phys. Rev. Lett., **16**, 748-750 (1966).
- [10] G. Zatsepin and V. Kuzmin, *Upper Limit of the Spectrum of Cosmic Rays*, Phys. JETP Lett. **4**, 78 (1966).
- [11] S. Swordy, Private Communication. The data points are collected from the following experiments; LEAP, Proton, Akeno, AGASA, Fly's Eye, Havarah Park, Yakutsk.
- [12] X. Bertou, M. Bortav and A. Latessier-Selvon, *Physics of Extremely High Energy Cosmic Rays*, Int. J. Mod. Phys. **A15** 2181-2224 (2000).
- [13] P. Sokolsky, *Introduction to Ultra High Energy Cosmic Ray Physics*, Addison-Wesley, 1989.
- [14] F. Aharonian, *et al.*, *High-Energy Particle Acceleration in the Shell of a Supernova Remnant*. Nature, **432**, 75-77 (2004).
- [15] A. Hillas, *The Origin of Ultra-High Energy Cosmic Rays*, Ann. Rev. Astron. Astrophysics, **22**, 425-44 (1984).

- [16] R. Giovanelli, G. Chincarini, and M. Haynes, *The H I Content of Galaxies in the Hercules Supercluster Evidence for Sweeping*, Ap. J. **247**, 383-402 (1981).
- [17] P. Bhattacharjee and G. Sigl, *Origin and Propagation of Extremely High Energy Cosmic Rays*, Phys. Rept, **327**, 109-247 (2000).
- [18] B. Connolley, S. BenZvi, C. Finley, A.S. O'Neil, and S. Westerhoff, *Comparison of the Ultra High Energy Cosmic Ray Flux Observed by AGASA, HiRes, and Auger*, Phys. Rev. **D74**, 043001 (2006).
- [19] D. De Marco, P. Blasi, and A.V. Olinto. *Astropart. Phys.* **20**, 53 (2003).
- [20] R.U Abbasi, *et al.*, *Measurments of the Flux of Ultra High Enegy Cosmic Rays from Monoculear Observations by the High Resolution Fly's Eye Experiment*, Phys. Rev. Lett. **92**, 151101 (2004).
- [21] M. Takeda, *et al.*, *Energy Determination in the Akeno Giant Air Shower Array Experiment.*, *Astropart. Phys.* **19**, 447-462 (2003).
- [22] D. Harari, S. Mollerach, E. Roulet and F. Sánchez, *Lensing of Ultra-High Energy Cosmic Rays in Turbulent Magnetic Field*, JHEP **03**, 045, (2002).
- [23] J.L. Han, *The Large-Scale Magnetic Field Structure of Our Galaxy: Efficiently Deduced from Pulsar Rotation Measure*, National Astronomical Observatories, Beijing, China. 3-12, (2004).
- [24] J.L. Han, R.N. Manchester, E.M. Berkhuijsen, and R. Beck, *Astro. Astrophys.* **322**, 98 (1997).
- [25] G. Novak, D.T. Chuss, T. Renbarger, G.S. Griffin, M.G. Newcomb, J.B. Peterson, R.F. Loewenstein, D. Pernic, and J.L. Doston *Astro. J.* **583**, L83 (2003).
- [26] S. Roy, *Bull. Astron. Soc. India* **32**, 205 (2004), [astro-ph/0411687].
- [27] T.N. LaRosa, *et al.*, *Astrophys. J.* **626**, L23 (2005), [astro-ph/0505244].
- [28] Alvarez-Muniz and Stanev, *The Large Scale Structure of the Galactic Magnetic Field and High Energy Cosmic Ray Anisotropy* (2005), [astro-ph/0507273].
- [29] D. Harari, S. Mollerach, and E. Roulet, *JHEP* **9908**, 022 (1999), [astro-ph/9906309]
- [30] M. Prouza and R. Smida, *Astron. Astrophys.* **410**, 1 (2003), [astro-ph/0307038]
- [31] T. Stanev, *Astrophys. J.* **479**, 290 (1997).
- [32] M. Kachelriess, P.D. Serpico, and M. Teshima, *The Galactic Magnetic Field as Spectrograph for Ultra-High Energy Cosmic Rays* (2005), [astro-ph/0510444].
- [33] C.L. Carilli, G.B. Taylor, *Ann. Rev. Astron. Astrophys.* **40**, 319, (2002).
- [34] V. Beresinsky, A.Z. Gazizo, and S.I. Grigoriva [astro-ph/0210095].

- [35] P. Blasi and D. De Marco, [astro-ph/0307067].
- [36] P. Blasi, S. Burles, and A.V. Olinto, *Astrophys. J.* **514**, L79 (1999).
- [37] E. Armengaud, G. Sigl, and F. Miniati, *Ultrahigh Energy Nuclei Propagation in a Structured, Magnetized Universe*, *Phys. Rev.* **D72**:043009 (2005).
- [38] K. Dolag, D. Grasso, V. Springel, and I. Tkachev. *Mapping Deflections of Ultra-High Energy Cosmic Rays in Constrained Simulations of Extragalactic Magnetic Fields*, *JETP Lett.* **79**, 583 (2004).
- [39] J.W. Cronin, *The Highest Energy Cosmic Rays*, [astro-ph:0402487].
- [40] T. Gaisser and A.M. Hillas, in *Proceeding of the 15th International Cosmic Ray Conference (ICRC)*, Plovdiv, 1997 (Plovdiv, Bulgaria, 1997), Vol.8, p.353.
- [41] T. K. Gaisser, *Cosmic Rays and Particle Physics*, Cambridge University Press, 1990.
- [42] T. Abu-Zayyad, Ph.D. Thesis, University of Utah, Salt Lake City, 2000.
- [43] G. Archbold, Ph.D. Thesis, University of Utah, 2002.
- [44] R.U. Abbasi, *et al.* *Techniques for Measuring Atmospheric Aerosols at the High Resolution Fly's Eye Experiment*, *Astropart. Phys.* **25** 74-83, (2006).
- [45] C. Finely, Ph.D. Thesis, Columbia University, 2006.
- [46] Pierre Auger Project Design Report, 2nd ed, <http://www.auger.org/admin/DesignReport/>, revised, March 1997.
- [47] J.W. Elbert, in *Proceeding of the Tokyo Workshop on Techniques for the Study of Extremely High Energy Cosmic Rays*, Tokyo, 1993, (Institute of Cosmic Ray Research, Tokyo, 1993) P.232.
- [48] C.R. Wilkinson, Ph.D. Thesis, University of Adelaide, Adelaide, 1998.
- [49] K.M. Simpsons, Ph.D. Thesis, University of Adeliade, Adelaide, 2001.
- [50] A.V. Apanasenk, *et al.*, in *Proceedings of the 26th (ICRC)*, Salt Lake Cirt, 1999,(University of Utah, Salt Lake City, 1999), Vol.3, p. 167.
- [51] J.H. Boyer, B.C. Knapp, E.J. Mannel, and M. Seman. *FADC-based DAQ for HiRes Fly's Eye*, *Nucl. Instrum. Meth.*, **A482** 457-474 (2002).
- [52] J.N. Matthews and S.B. Thomas. In *Proceeding of the 27th(ICRC)*, Hamburg, 2001 (Copernicus Gesellschaft, Hamburg, 2001), pages 350-353.
- [53] T. Abu-Zayyad, *et al.*, in *Proceedings of the 26th (ICRC)*, Salt Lake Cirt, 1999,(University of Utah, Salt Lake City, 1999), Vol.3, p. 349-354.
- [54] J.N. Matthews, *et al.*, HiRes Internal Memo (1997).

- [55] B.F. Jones, *et al.*, in Proceedings of the 27th (ICRC), Hamburg, 2001 (Copernicus Gesellschaft, Hamburg, 2001), Vol. **1**, p.641.
- [56] G.C. Archbold, Ph.D. thesis, University of Utah, Salt Lake City, 2002.
- [57] K. Reil, Ph.D. thesis, University of Utah, Salt Lake City, 2002.
- [58] L.R. Wiencke, *et al.*, Nucl. Inst. Meth., Sect. **A 428**, 593 (1999).
- [59] R. Abbasi, *et al.*, *Techniques for Measuring Atmospheric Aerosols at the High Resolution Fly's Eye Experiment*. Astropart. Phys., **25** 74-s3, (2006).
- [60] J. Boyer, E. Mannel, and L. Wiencke. '*Shoot the Shower*': *Probing Atmospheric Clarity of the Shower/ Detector Plane at HiRes*. Proceeding of the 28th ICRC (2003).
- [61] C. Song, PhD Thesis, Columbia University, 2001.
- [62] C.R. Wilkinson, *et al.*, *Geometrical Reconstruction with the High Resolution Fly's Eye Prototype Cosmic Ray Detector*, Astroparticle Physics, **12**, 3:121-134 (1999).
- [63] P.A. Sadowski, *et al.*, *Geometry and Optics Calibration for Air Fluorescence Detectors Using Starlight*, Astropart. Phys.(to be published)
- [64] V.F. Leavers, *Shape Detection in Computer Vision Using the Hough Transform*, London, New York:Springer-Verlag (1992).
- [65] G.M. Tanco, M. Teshima & M. Takeda, in Proceedings of the 28th (ICRC), Tsukuba, 2003,(Tsukuba, Japan, 2003), p. 747-750.
- [66] B. Stokes, Ph.D. thesis, University of Utah, Salt Lake City, 2006.
- [67] R.U. Abbasi *et al.*, Astrophys. **L 73**, J.610 (2004).
- [68] R.C. Hartman *et al.*, Astrophys. J.Suppl. 123, **79** (1999).
- [69] P.G. Tinyakov and I.I. Tkachev, JTEP Lett., **74**, 445 (2001).
- [70] P.G. Tinyakov and I.I. Tkachev, Astropart. Phys. **18**, 165 (2002).
- [71] D.S. Gorbunov , P.G. Tinyakov , I.I. Tkachev, and S.V. Troitsky, Astrophys. J, 577, **L93** (2002).
- [72] N. Evans, F. Ferrer, and S. Sarkar, Phys. Rev.,103005, **D93** (2003).
- [73] D. Torres, S. Reucroft, O. Reimer, and Anchordoqui, L. A. Astrophys. J., 595, **L13** (2003).
- [74] <http://math.rice.edu/pcmi/sphere/gos4.html>
- [75] W.M. Smart, *Spherical Astronomy*, Cambridge University Press, 1960.

- [76] W.Gellert, *et al. Spherical Trigonometry*, Van Nostrand Reinhold, 1989.
- [77] D. Zwillinger, *Spherical Geometry and Trigonometry*, CRC Press, 1995.